Engineering 3-D Neural Organoid Morphology

By

Carlos R. Marti Figueroa

A dissertation submitted in partial fulfillment

of the requirements for the degree of

Doctor of Philosophy

(Biomedical Engineering)

at the

UNIVERSITY OF WISCONSIN-MADISON

2020

Date of oral examination: 05/15/2020

The dissertation is approved by the following members of the Final Oral Committee:

Randolph S. Ashton, Professor, Biomedical Engineering
William Murphy, Professor, Biomedical Engineering
Justin Williams, Professor, Biomedical Engineering
Lih-Sheng Turng, Professor, Mechanical Engineering
Qiang Chang, Professor, Medical Genetics and Neuroscience

Abstract

Three-dimensional organoids derived from human pluripotent stem cell (hPSC) derivatives have become widely used in vitro models for studying development and disease. Their ability to recapitulate facets of normal human development during in vitro morphogenesis produces tissue structures with unprecedented biomimicry. Current organoid derivation protocols primarily rely on spontaneous morphogenesis processes to occur within 3-D spherical cell aggregates with minimal to no exogenous control. These yields organoids containing microscale regions of biomimetic tissues, but at the macroscale (i.e. 100's of microns to millimeters), the organoids' morphology, cytoarchitecture, and cellular composition are non-biomimetic and variable. The current lack of control over in vitro organoid morphogenesis at the microscale induces aberrations at the macroscale, which impedes realization of the technology's potential to reproducibly form anatomically correct human tissue units that could serve as optimal human in vitro models and even transplants.

Here, we have developed a methodology for engineering three-dimensional neural tube organoid morphology using alginate hydrogels with internal architecture and human embryonic stem cells. First, we describe the use of poly(vinyl alcohol)-calcium salt templates (PVOH-Ca) fabricated by micro-injection molding, a parallel mass-production process, to conveniently cast internal geometries within both bulk curing hydrogels and ionically cross-linked alginate hydrogels. Calcium salt solubility was discovered to be a critical factor in optimizing the polymer composite's manufacturability, mechanical properties, and the quantity of calcium released upon template dissolution. Metrological and computed tomography (CT) analysis showed that the template's calcium release enables precise casting of microscale channel geometries within alginate hydrogels (6.4 ± 7.2% average error). Assembly of modular PVOH-Ca templates to mold 3D channel networks within alginate hydrogels is presented to demonstrate engineering scalability.

Secondly, we describe a methodology for the injection hPSCs into alginate hydrogel monoliths with a PVOH-Ca-molded central microscale channel to produce cylindrical aggregates of the channel's shape and diameter, to generated neural organoids that mimicked the developing neural tube. Variables such as the initial cell injection concentration, the method of injection, and physical restriction of the hydrogel channel outlet were found to be critical for the reproducible hPSC cylindrical aggregates.

Finally, this platform was used to generate neural tube mimetic organoids using chemically defined media conditions. We found that microscale dimensions of the cylindrical aggregate play an important role in the formation of a single polarized neuroepithelial tube. We found that at 250µm we could generate 3D neuroepithelial tube organoids that resembled the in vivo neural tube as evidenced by the single polarized expression of N-Cadherin, ECM basement membrane protein Laminin, and early neural progenitor marker Pax6. To our knowledge, this is the closest demonstration of a neural tube mimetic in vitro, and we believe it is the first step into standardizing the formation of cerebral organoids. Ultimately, the long-term goal is to use a standardized version of this platform to replicate developmentally relevant corticogenesis in cerebral organoids. Integrating this platform with different cutting-edge techniques such as CRISPR-CAS9 mediated gene editing and patient-specific induced pluripotent stem cell reprogramming will provide a power model to study neurodevelopmental and psychiatric diseases that affect the later structures that develop from NEOs, which are the brain, retina, and spinal cord.

Acknowledgements

While my journey at Madison has had many challenges along the way, I cannot be any more proud and grateful for being a part of the department of Biomedical Engineering, the University of Wisconsin-Madison, and the city of Madison as a whole. These have truly been the best and most life-changing years of my life and I cannot be happier with all the connections I have made in my time here.

I want to first and foremost thank the Ashton lab for welcoming me from Puerto Rico for the first time as a summer intern and then as a Graduate student. I have grown a lot from being in this lab and all of the people in it made this experience, that at times can be stressful and difficult, so much more enjoyable. I am grateful for all the training, collaborations, and enjoyable times I have had with every single one of the members in the lab.

I also want to thank all the people I have had the opportunity to collaborate with from other labs. Starting with Dr. Turng for providing valuable feedback and access to his lab equipment, such as the Extruder and Injection molding machine, and his students such as Tom Ellingham and George Schmidt for providing feedback and content to my first publication. I would like to thank Dr. Thompson for access to the lab's cryosection equipment, Dr. Saha for access to the cell injection microscope and epifluorescence microscope, Dr. Murphy and Dr. Daly for proving PEG hydrogels for our second publication, and finally Dr. Crone for providing access to the Instron Microtester and donating Polyacrylamide for experiments done in my second publication.

I would like to acknowledge all the funding that has supported me during my time at UW-Madison. First, I would like to thank all of the GERS community, starting with Kelly Burton with

all of her support over the years in making sure all of us felt like at home in Madison, and for providing funding for 2 years of my research. I would also like to mention the research grants awarded to my PI that have supported my research such as NSF, the EPA, the Burroughs Welcome Fund, the Stem Cell and Regenerative Center (SCRMC), and the National Institute for Neurological Disorders.

I would like to thank the Wisconsin Institute for Discovery (WID) for providing the home for my research experience. It has been amazing to work in such a collaborative workspace and I truly appreciate everyone that has made my stay in the WID so great.

I would also like to thank my friends in Madison, who helped keep a balanced lifestyle and made this journey even more enjoyable. Starting with those I knew through my lab or program, thanks to Gavin Knight, Jared Carlson – Stevermer, John Krutty and Ana Porras for the fun times playing volleyball during the summers. Thanks to Alireza Aghayee Meibody and Brett Napiwocki, who became like brothers to me and provided many fun times playing in Pool Leagues. I would like to also thank the Latin dance community for making Madison feel a little like Puerto Rico even during the winter. And finally, thank you to all my friends in the Madison Puerto Rican community including Ricardo Rivera, Diana Guzman, Carlos Baez, Carla Principe, Angel Perez, Xavier Arzola, Karla Esquilin, Carlos Milan, Luis Carmona, Dianiris Luciano, Sofia Macciavelli, and Lorraine Rodriguez. You have all become family to me and I will always be grateful for the wonderful experience we have had throughout our time here.

I would also like to thank my family who have supported me throughout the years. I would first like to thank my dad for always pushing me to do my best. He always saw potential in me even

when I doubted it and in large part it is thanks to him this day has come. I would also like to thank Nestor Hernandez, while not related by blood he is like my brother since the 7th grade and a fellow UW-Madison graduate. Our friendly or brotherly competition has always been a driving force for me into become as knowledgeable as I can both in my career and in general. Finally, I would like to thank my partner Cristina Zambrana, who has been the rock by my side always believing in me, loving me and supporting through the most difficult times of my journey. Her love and support have been fundamental during these last 3 years of my PhD program.

I would also like to thank the members of my committee for the feedback and support throughout my time here, especially during my preliminary exam and towards the final stretch leading to my thesis defense.

Finally, I would like to thank my PI and Mentor, Dr. Randolph Ashton. Thank you for the opportunity to join your lab as undergraduate and then as a graduate student. Thank you for your guidance not only as a research mentor, but also as a career and life mentor. I will always be grateful for your support towards my career goals and for always providing useful feedback in my research project as well as useful advice for my career goals.

Table of Contents

Chapter 1: Introduction and Background

Most of the introduction and background information presented in this chapter appear in the following review article:

> Marti-Figueroa, C. R., & Ashton, R. S. (2017). The case for applying tissue engineering methodologies to instruct human organoid morphogenesis. Acta Biomaterialia. Elsevier Ltd. https://doi.org/10.1016/j.actbio.2017.03.023

1. Neurological Disorders

Neurological diseases are a range of conditions which yield functional deficits primarily due to the loss of neurons in the human brain. Neurons are post-mitotic and not readily regenerated, so when they become damaged or die, they cannot be replaced by the body. As such, neurodegenerative diseases are incurable and debilitating conditions that result in the progressive loss of nerve cells. This causes problems with movement (ataxias) or mental function (dementias). Currently, over twenty million Americans experience some form of neuropathy, and 16% of U.S. households contain an individual with brain impairment[[1]]. The current estimated annual cost to American society of just 9 common neurological diseases is staggering, totaling nearly 800 billion dollars a year[[2]]. Given the extraordinary and rapidly growing costs of neurological disorders and the low success rate of clinical translation[3], a concrete strategy is urgently needed to reduce the burden of neurological disease.

2. Limitations with current 2D and 3D cultures for disease modeling

Human pluripotent stem cells (hPSCs) provide an unlimited source for generating all tissues of the human body in vitro. Over the past two decades, efforts have been focused on deriving a

plethora of cell types in 2-D culture for regenerative medicine applications such as transplantation [4] and in vitro disease modeling [5][6]. These cultures have been widely implemented as pre-clinical high-throughput screening platforms. Yet, it remains debatable as to how well standard 2-D cultures recapitulate the normal physiology and disease pathologies of in vivo tissues that contain organotypic cell phenotype diversity within intricate micro-to-macroscale cytoarchitectures. To create improved human tissue models, researchers over the past two decades have developed varied hydrogel formulations for encapsulating and culturing cells in 3-D [7]. Still, even with groundbreaking advances in bioprinting [8], the ability to controllably engineer anatomically correct substitutes of human tissues in vitro remains limited. Novel approaches and methodologies are needed to reproducibly engineer such hPSC-derived tissues, which would contain in vivo levels of cell phenotype diversity spatially organized in biomimetic cytoarchitectures at both the micro and macroscale.

3. Organoids as an Alternative Model to Tissue Engineering Approaches

Recent breakthroughs in organoid technology provide a basis for such ‘next-generation’ tissue-engineered organogenesis approaches [9]. To date, tissue-specific organoids are commonly created from 3-D spherical aggregates of hPSCs, their respective germ layer or organ stem/progenitor derivatives, or primary progenitor cells of equivalent developmental immaturity. Within these aggregates, the cells spontaneously morph (i.e. differentiate and self-organize) recapitulating critical facets of early-stage human embryogenesis to generate millimeter-size tissues that have microscale regions mimetic of fetal tissues [10], [11]. In this thesis, a distinction is made between these organoids, which start as a microscale cell aggregate,

versus engineered organotypic cultures typical of traditional tissue engineering approaches, which use bottom-up or top-down engineering of tissues by spatially assembling their differentiated cellular components within a matrix [12]–[14] (**Fig. 1**). While organotypic 3-D cultures have also been referred to as organoids and may functionally mimic some aspects of their respective organ, they generally lack the remarkably biomimetic cell phenotype diversity and tissue cytoarchitecture that arises during morphogenesis processes [9], [11], [15].

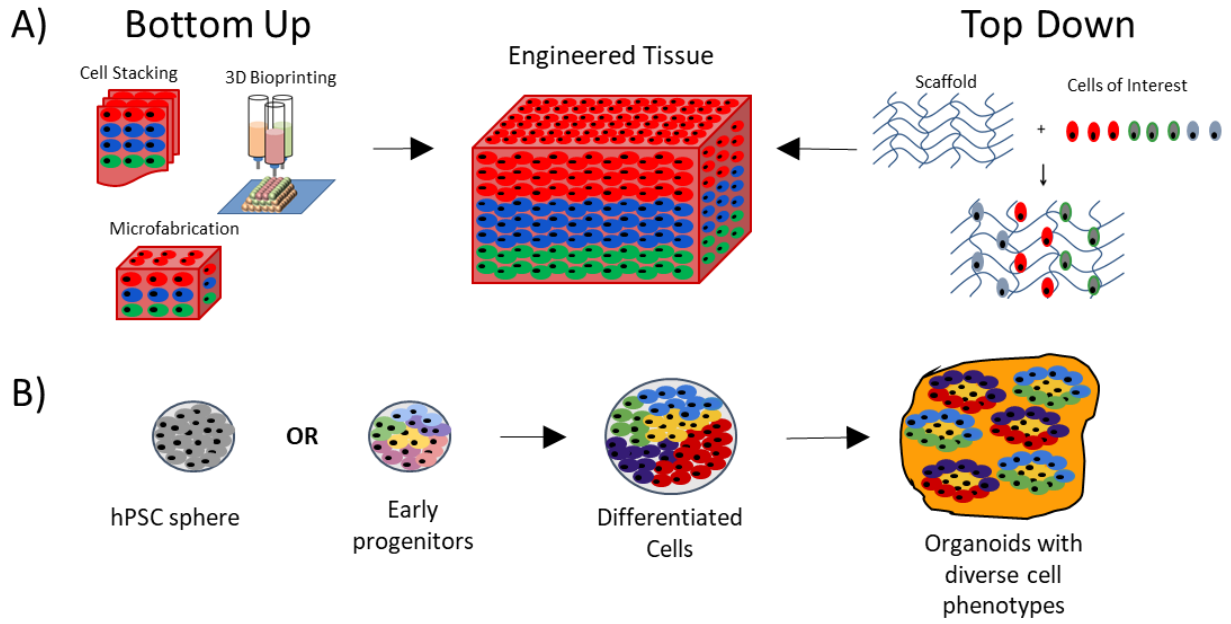

Figure 1: Engineered organotypic tissues vs. organoid morphogenesis. (A) Current methods for generating in vitro tissues involve either bottom up or top down tissue engineering approaches. In bottom-up approaches, diverse methods are used to create modular tissue units, which are assembled or grow into larger tissues with specific cytoarchitectural features. In top-down approaches, cells and biomaterial scaffolds are combined and cultured until the cells fill the support structure to create an engineered tissue. Both approaches typically use a limited subset of progenitors or differentiated cell types. (B) Alternatively, organoids are generated from a microscale pluripotent or germ-layer specific stem cell aggregate and allowed to undergo spontaneous morphogenesis. This yields a biomimetic population of tissue-specific progenitors that produce organotypic levels of different cell types within microscale tissue cytoarchitectures that closely resemble those found in endogenous developing organs.

4. Organoids replicate tissue morphogenesis but remain developmentally immature

Within the past decade, there has been significant progress in devising a variety of human organoid protocols for brain [16], liver [17], kidney [18], [19], prostate [20], retina [21], lung [10]

and gastrointestinal tissues [22]. The protocols generally entail formation of 3-D cell aggregates either by forced aggregation or self-organization followed by culture on or within an extracellular matrix of choice, commonly matrigel [23] or collagen [21]. For example, brain organoids of up to 4 mm in diameter were derived via neural differentiation of hPSC aggregates encapsulated within Matrigel hydrogels and cultured in a stirred-tank bioreactor for 1-3 months. Immunohistochemical analysis revealed that brain organoids can contain a variety of brain tissues including miniature cerebral cortex formations with all six laminar neuronal layers [16]. Vascularized liver organoids, termed liver buds, were generated from self-aggregating 2-D co-cultures of induced pluripotent stem cell (iPSC)-derived hepatic endodermal progenitors, human mesenchymal stem cells, and human umbilical vein endothelial cells. Upon transplantation, the liver organoids could functionally engraft and increase survival in a liver failure mouse model [17]. Kidney organoids were generated from 3-D aggregates of hPSC-derived ureteric epithelium and metanephric mesenchyme formed using forced centrifugation. After in vitro culture at a simulated air-water interface, the aggregates morphed into organoids containing nephrons associated with a collecting duct network surrounded by renal interstitium [18]. Also, prostate organoids have been generated from 3-D aggregates of primary luminal stem/progenitor cells cultured in 3-D Matrigel hydrogels in the absence of stroma [20]. While such organoid protocols represent significant scientific advancements, the generated tissues generally remain developmentally immature in vitro [24], [25] and recapitulate the early stages of in vivo organogenesis with only partial accuracy [26].

5. Organoids form via Spontaneous Morphogenesis

A common denominator of organoid derivation protocols is their reliance on spontaneous morphogenesis to occur freely within cell aggregates. The cells' innate morphogenetic properties produce internal cell phenotype diversity and microscale cytoarchitectural structures that are unmatched in biomimetic accuracy compared to what can be achieved using current microfabrication or tissue engineering techniques [11], [27], [28]. As such, organoids have enabled the generation of unprecedented microscale human tissue structures in vitro that enhance the clinical relevance of cell culture disease models and drug discovery studies [11]. However, the uncontrolled, spontaneous morphogenesis process at the microscale inherently results in a lack of reproducibility and biomimicry in the organoids' macroscale anatomy [29]. In the human embryo, morphogenesis is instructed at all scales by spatial and temporal perturbations in myriad biochemical and biophysical factors [30]. These factors act in a highly coupled manner through complex feed-forward and feed-back signaling loops to dynamically orchestrate the cellular composition and cytoarchitecture of developing tissues. Tissue engineering methodologies exist for exerting multiscale spatiotemporal control over these factors. Yet, they remain to be integrated into organoid derivation protocols that accurately and reproducibly recapitulate organoid morphogenesis in vitro.

6. Strategies for Providing Engineering Control over the Organoid Morphogenesis Process

Current and potential applications of tissue engineering methodologies for instructing human organoid morphogenesis will be discussed throughout the rest of this chapter. In particular, their use to exert spatial and temporal control over the organoid's biochemical environment, morphology, and cellular composition will be considered. These include methods for generating

composite hydrogel scaffolds with spatially compartmentalized microenvironments and internal architecture, controlling cellular cytoarchitecture during initial organoid assembly, and spatiotemporal regulation of morphogen gradients during organoid culture (**Fig. 2**). The use of genetic engineering to endow the organoid's cells with artificial gene circuits capable of producing programmable morphogenesis responses is a complementary approach that has recently been reviewed elsewhere [29]. Only through integration of such engineering approaches with organoid derivation protocols will the requisite control over in vitro morphogenesis be achieved to enable standardized biomanufacture of functional human tissues with mimetic anatomy and physiology.

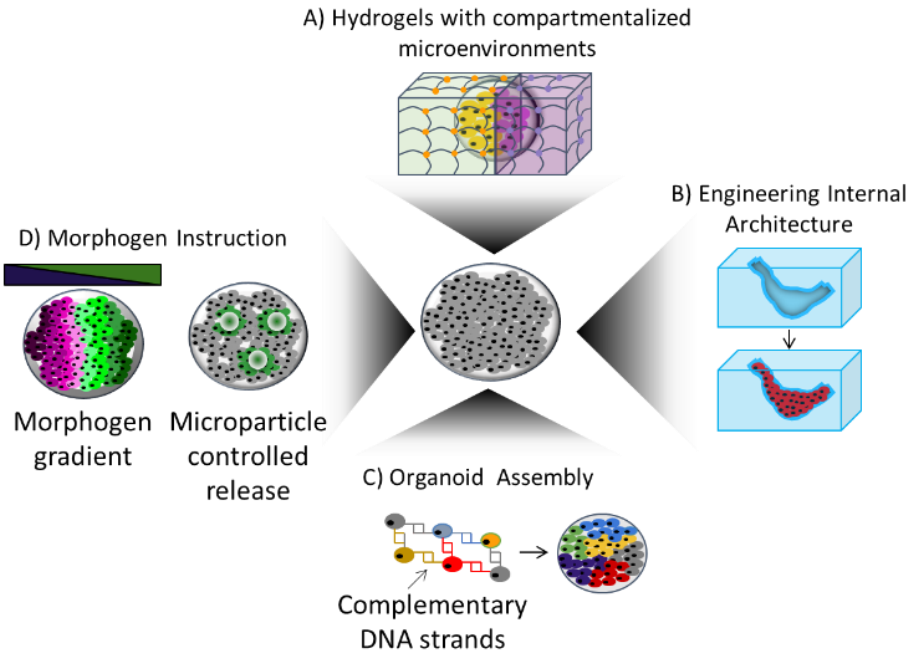

Figure 2: Potential engineering approaches for instructing organoid morphogenesis. (A) Hydrogels with compartmentalized microenvironments could be used to mimic spatiotemporal interactions with proximal tissues encountered during development to instruct cell differentiation. (B) Hydrogel molds with predefined internal architecture could be used to impose morphological constraints on embedded/encapsulated organoids. (C) Direct control of cellular arrangement, composition, and aggregate morphology upon initial assembly could be used to influence subsequent organoid morphogenesis processes, e.g. spatial orientation of cell progeny/tissues. (D) Global or localized morphogens gradients generated by microfluidics or microparticles, respectively, could be used to spatially instruct cellular differentiation and migration during organoid morphogenesis.

6.1. Engineered Hydrogel Scaffolds

Hydrogels are water-swollen, hydrophilic, polymeric networks that remain insoluble due to the presence of chemical or physical crosslinks [31]. They can be generated using a plethora of natural [32] and synthetic [33] materials and engineered with numerous biochemical or biophysical properties to influence cell fate [30]. Hydrogels represent an ideal culture system for guiding 3-D morphogenesis of embedded organoids. However, most organoids are currently formed by encapsulation within Matrigel hydrogels, a heterogeneous, ill-defined mixture of solubilized basement membrane proteins from mouse sarcomas [34]. A few groups have begun to demonstrate the possibility of using more chemically defined hydrogels to support organoid morphogenesis. Lindborg et al. demonstrated formation of rudimentary cerebral organoids within a hyaluronan-chitosan hydrogel blend [35]. Also, Meinhardt et al. observed spontaneous morphogenesis of neural tube organoids generated from single mouse embryonic stem cells (mESCs) within a pure PEG hydrogel, although at a significantly lower rate than Matrigel hydrogels [36]. These represent initial steps towards developing ‘blank-slate’ chemically defined scaffolds that support the morphogenesis of embedded human pluripotent or progenitor cell aggregates. Such defined hydrogel substrates will be necessary to experimentally deduce design principles for predictable instruction of tissue-specific organoid morphogenesis.

In vivo, the morphogenesis of organ anlagen is spatially and temporally diversified, in part, through interactions with proximal tissues that provide distinct microenvironments [37]. A potential approach for mimicking these interactions in vitro is to embed organoids within composite hydrogels presenting spatially compartmentalized microenvironments (**Fig. 2A**). Each microenvironment can be tailored with distinct biochemical factors, e.g. ECM peptides [38],

recombinant growth factors [39], [40] and receptor ligands motifs [41], [42], and biophysical properties, e.g. elasticity [43], [44], topography [45], or traction [46], to instruct tissue-specific fates when populated by the growing organoid. Technologies for dynamically regulating microenvironments will also be necessary to recapitulate the temporal dependence of cues during morphogenesis [47]–[50]. Furthermore, since such cues act in a synergistic and coordinated manner to instruct cell fate [30], [51], systems level approaches using high-throughput hydrogel culture screening technologies [52]–[54] will be required to assess and model their combinatorial effects [55], [56]. In aggregate, these types of studies could be used to deduce guidelines for engineering hydrogel microenvironments that instruct tissue-specific morphogenesis processes.

6.2. Composite hydrogels with compartmentalized microenvironments

A variety of tissue engineering techniques are capable of synthesizing composite hydrogels by either differentially modifying an existing hydrogel monolith, assembling hydrogel building blocks, or fabricating composite hydrogels de novo. For example, the Anseth group combined the use of wavelength-specific, photoactivated thiol-ene click chemistry and nitrobenzyl ether degradation to create a versatile platform for modifying both the biochemical and biophysical properties of PEG hydrogels using laser scanning microscopy [48], [49] (**Fig. 3A**). When combined with multiphoton microscopy, this platform can be used to ‘direct write’ discrete microenvironments within PEG hydrogels up to a millimeter thick with microscale precision. Additionally, when integrated with a live-cell imaging platform, it enables dynamic and in situ microenvironmental perturbations during organoid culture. As an alternative composite hydrogel synthesis approach, Qi et al. developed a method for programmable assembly of

hydrogel building blocks using embedded, rolling circle generated DNA strands as 'glue' [57] (**Fig. 3B**). The complementarity of each block's DNA sequence can be designed to tailor the hydrogel's macroscale geometry and composition. In principle, this approach could be used in both one-off composite hydrogel synthesis or to add new microenvironments or signaling sources to an existing organoid-hydrogel complex in real-time. The latter option being used to recapitulate spatiotemporal juxtapositions of proximal tissues that arise during organogenesis in vivo [40]. For a more simplistic method to build composite scaffolds, the Kaplan lab combined hydrogels and mechanically superior silk scaffolds to enable manual and adhesive-free assembly of concentric subunits [58] (**Fig. 3C**). They used this method to generate 3-D multi-layered brain-like cortical tissues with compartmentalized microenvironments. Composite hydrogels can also be synthesized de novo using photochemistry and 3-D printing techniques. Multiphoton excitation of Rose Bengal, a singlet oxygen generator, within a solution of whole ECM proteins can be used to build 3-D, covalently linked ECM hydrogels of defined shape using automated raster sequences [59] (**Fig. 3D**). The use of whole ECM proteins as the hydrogel substrate versus recombinant fragments or peptides may better mimic in vivo microenvironments since myriad motifs throughout ECM proteins are involved in forming a complex signaling milieu that affects cell fate [60][57]. There are numerous other 3-D printing methods that could be used to fabricate composite hydrogels. These methods could generate compartmentalized microenvironments with dimensions down to tens of microns using a spectrum of different hydrogels (reviewed by [61]). Additionally, bioprinting could be integrated to precisely orient a cell aggregate within the 3-D printed, composite hydrogel's macroscale structure. However, bioprinting can have issues

with cell viability due to suboptimal nozzle, cartridge, and bioink designs and environmental control during printing [8].

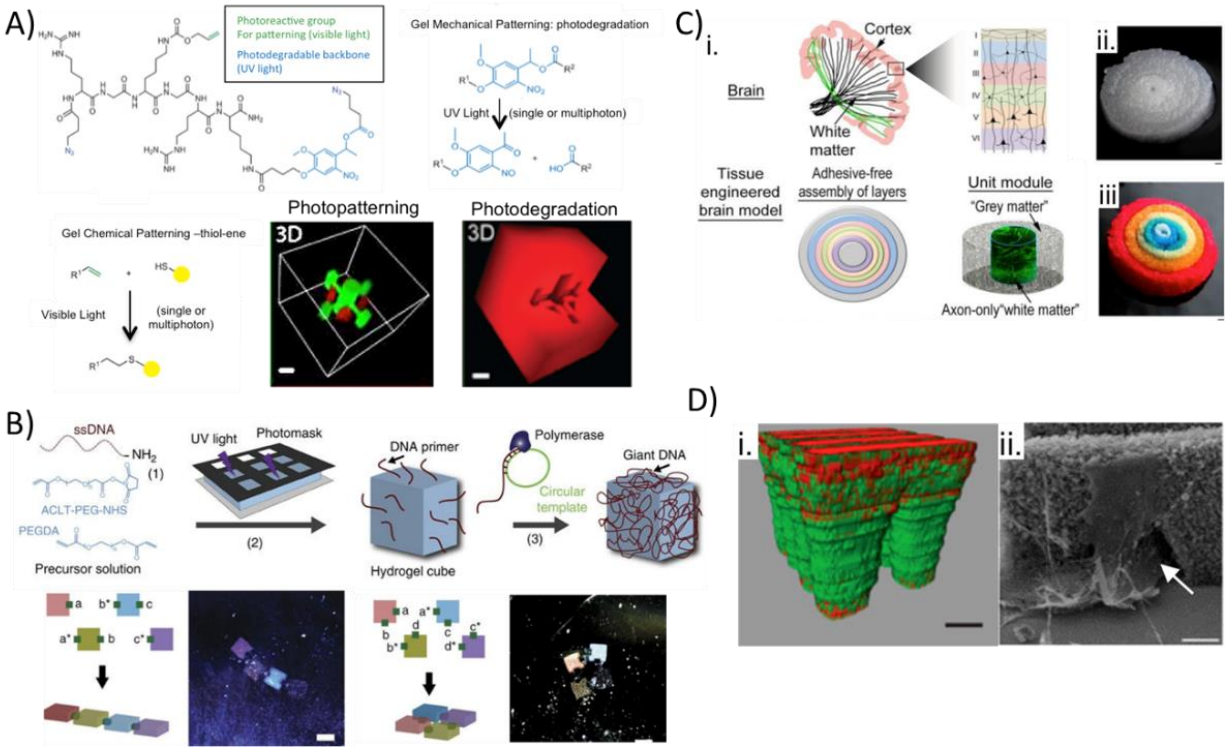

Figure 3: Engineering hydrogels with compartmentalized microenvironments. (A) Hydrogels containing clickable (green) and UV-degradable (blue) bis(azide)-functionalized polypeptides form a 3-D substrate onto which biochemical (click-additions, 'Photopatterning') and biophysical (UV-degradation, 'Photodegradation') properties can be directly written using focused visible light or UV lasers, respectively. Scale bar 100 µm. Images from [46]. (B) Schematic of DNA-hydrogel composite synthesis (top) that enables programmable assembly at the microscale (bottom). Scale bar 1mm. Images from [54]. (C) A modular design of bioengineered brain-like cortical tissues. (i) Cytoarchitectural features include neocortex tissues with neuronal layers and an underlying white matter region (top). Mimetic tissue constructs were engineered using adhesive-free assembly of concentric silk scaffold layers within a unit module consisting of neuron-rich grey and axon-rich white matter regions (bottom). Image of assembled concentric silk scaffolds of (ii) original or (iii) dyed color. Scale bar is 1 mm. Images from [55]. (D) 3D reconstruction of (i) a Rose Bengal (red) and BSA/Texas Red-Laminin (green) hydrogel fabricated by multiphoton excited photochemistry. Scale bar is 10 µm. (ii) Scanning electron micrograph of a mesenchymal stem cell (arrow) migrating into a BSA/Laminin hydrogel. Scale bar is 10 µm. Images from [56].

6.3. Hydrogels with internal architecture

In traditional tissue engineering, the morphology of the engineered tissue is mostly fixed and provided by the macroscale geometry of the impregnated scaffold [62], [63] (**Fig. 1A**, Top-down engineered tissue). However, in vivo, developing organs begin as microscale formations that

grow orders of magnitude in dimension and often morph through several transient geometries before achieving their final tissue morphology [37][34]. Similar to their in vivo counterparts, human organoids begin morphing early in their derivation process and start producing internal tissue cytoarchitecture before reaching dimensions of even 100's of microns in diameter [10], [16], [19], [21], [22]. Hence, it will be necessary to control organoid morphology from the micro- thru macroscale to instruct anatomically correct morphogenesis. Recent publications showing that regulating the 2- and 3-D morphology of hPSC-derived tissues in vitro can predictably induced gastrulation [64] and self-organization of cytoarchitectural structures such as polarized epithelial rings [36], [65] and lumens [66], [67] further support this conclusion. Many potential tissue engineering methods for controlling microscale organoid morphology exist. However, there has been limited application to organoid systems, and they lack the ability to instruct dynamic spatiotemporal changes in organoid morphology.

A potential approach to controlling microscale 3-D organoid morphology is to have the cell aggregate morph inside of a hydrogel with a defined internal architecture (**Fig. 2B**). In this manner, the hydrogel's internal void space would provide a physical barrier to which the growing organoid would conform. Current methods for generating versatile internal features within hydrogels include 3-D printing, sacrificial molding, and light-induced photocleavage. For example, the Fienberg lab recently developed a novel, low-cost 3-D printing method called freeform reversible embedding of suspended hydrogels (FRESH). It uses syringe-based extrusion to print suspended hydrogels into a bath of gelatin microparticles that act as a Bingham plastic— behaves as a solid at low shear rates but is fluid at higher shear rates. Using CAD design files, the system can rapid prototype hydrogels with thickness down to ~150 microns, and as indicated by personal

communication, upgrades to the FRESH method now enable printing of hydrogels with internal architectures of dimensions down to ~300 microns [68]. Sacrificial molding is capable of producing hydrogels with internal cavities of micro-to-macroscale dimensions. It entails encapsulating a dissolvable or degradable material within a second orthogonal hydrogel material. Once the composite hydrogel has been formed, removal of the internal sacrificial material yields an outer hydrogel with defined internal architecture. Miller et al. developed the first tissue engineering sacrificial molding platform using 3-D printed, water soluble carbohydrate glass templates. They demonstrated its broad utility by molding channels for vascular network formation within a variety of hydrogels materials [69]. The Huang lab also developed a platform for generating vascularized gelatin hydrogels using a calcium alginate sacrificial unit. Calcium alginate lattices were cast using PDMS molds, and dissolved from within a gelatin mold using an EDTA solution to chelate crosslinking calcium ions [70]. While both sacrificial molding techniques are highly versatile, both alginate hydrogels and the carbohydrate glass material suffer from weak and brittle mechanical properties, respectively. As an alternative, Toocio et al. has demonstrated sacrificial molding using mechanically superior poly-vinyl alcohol (PVOH) templates cast using PDMS molds [71]. Still, due to their rapid dissolution in water, both the carbohydrate glass and PVOH templates provide poor control over microscale cavity dimensions within slow gelling and thermoset hydrogels such as alginate monoliths and Matrigel, respectively. These sacrificial molding techniques have been primarily used in top-down tissue engineering with human endothelial cells to create vascularized tissues. However, they could also be applied to creating hydrogels with internal void spaces to which the morphology of encapsulated, growing organoids would conform.

While 3-D printing and sacrificial molding are versatile techniques that can be widely disseminated, their use to generate internal architecture within a hydrogel monolith is currently a one-off proposition. It would take an entirely new printed or molded hydrogel to instruct secondary or tertiary organoid morphologies, which are common facets of organ morphogenesis in vivo. A merger of these techniques with the photocleavable PEG hydrogel material created by the Anseth group could alleviate this issue by enabling spatiotemporal changes in internal hydrogel architecture [49]. Whichever approach is pursued, the placement of organoids within the hydrogel's internal cavity post-fabrication remains a tricky problem. This exemplifies how innovation is needed to fully integrate tissue engineering methods with organoid derivation protocols.

6.4. Controlling Organoid Assembly

The earliest cell fate decisions in the developing embryo are based upon the spatial orientation of cells within an aggregate. The human embryo begins as a spherical aggregate of identical totipotent cells (up to the 4-cell stage) [72], but a divergence in fates occurs between cells on the exterior (i.e. trophectoderm) and interior (i.e. inner cell mass) by the 16-cell stage [73]. This exemplifies how microscale tissue morphology and cell positioning upon tissue assembly can cause slight variations in the immediate microenvironment that induce divergent morphogenetic fates. The cellular composition of nascent tissues is also critical for morphogenesis since juxtacrine and paracrine signaling between neighboring cells is known to instruct divergent cell fates [41]. James Wells' lab recently observed such effects when adding hPSC-derived neural crest cells (NCCs) to hPSC-derived mid/hindgut tube spheroids to generate human intestinal organoids (HIO's) with a functional enteric nervous system (ENS). Intrinsic cues within the HIO

instructed developing ENS cells to acquire biomimetic positioning within the organoid's cytoarchitecture, and signaling from the ENS cells induced differential organoid growth factor levels, absorptive and secretory cell gene expression profiles, and proliferation rates of progenitor cells within the HIO's intestinal crypt compartments [74]. It is predicted that controlling cellular arrangement and composition as well as the microscale tissue morphology during initial organoid assembly will have significant effects on subsequent morphogenesis (**Fig. 2B** and **C**).

Several methods have been developed that could be used to generate organoids with custom morphologies and compositions via guided cellular assembly. The Gartner lab has developed DNA-programmed assembly of cells (DPAC) and demonstrated its ability to spatially program the arrangement of cells within 2-D and 3-D organoids of diverse shapes [75] (**Fig. 4A**). The programmed assembly is orchestrated using 2-D DNA-patterned substrates to guide the organized adhesion of cells presenting complimentary lipid-modified oligonucleotides. After assembly, the cell aggregate can be released from the substrate using a DNase treatment and encapsulated within a 3-D matrix for subsequent organoid formation. Laser-based direct write bioprinting can also be used to precisely deposit cells in 2-D and 3-D formations [76], [77] (**Fig. 4B**). This technique uses a focused laser beam to rapidly volatilize a support layer underlying a cell containing matrix on the donor print ribbon. The resulting shock waves force the overlying cells to transfer onto an adjacent collector substrate [8], [78]. The Chrisey group has used matrix-assisted pulsed laser evaporation direct writing (MAPLE-DW) to print small clusters of cells onto and within matrigel substrates [76], [79], and variations of laser-based direct writing can achieve single cell resolution [80]. Combining such methods with microfabricated chambers [81], [82] or

hydrogels with internal architecture would create powerful approaches for controlling cellular arrangement and composition within an organoid of defined, microscale 3-D morphology.

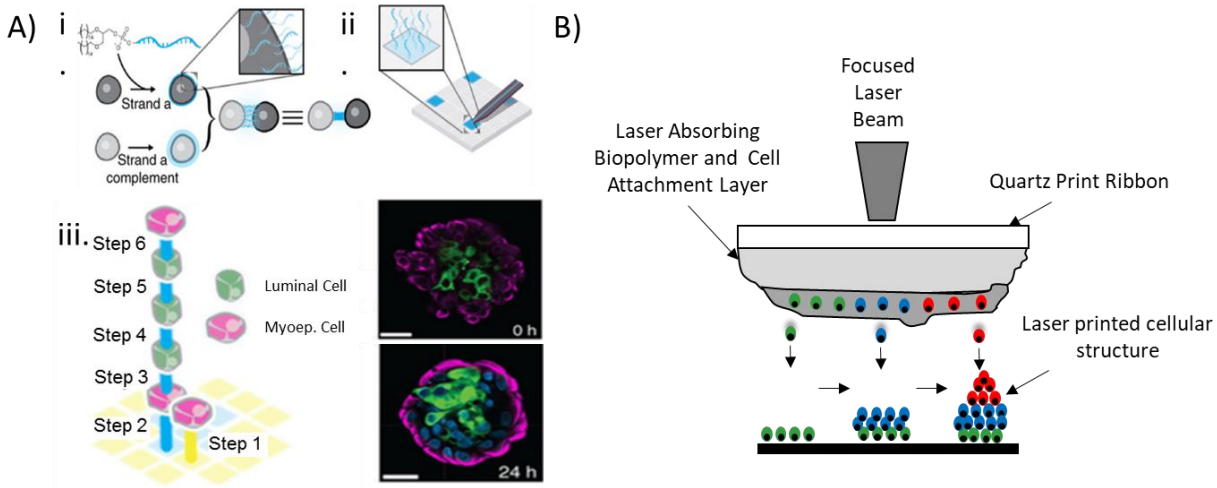

Figure 4: Exemplary methodologies for controlling initial organoid assembly. (A) Schematic of DNA-programmed assembly of cell aggregates (DPAC). (i) Assembly is programmed using the complementarity of lipid-modified oligonucleotides that spontaneously intercalate within cell membranes upon incubation. (ii) To control the morphology, arrangement, and composition of cellular aggregates, DNA-presenting micropatterned substrates with complementary sequences are used as a scaffold to spatially organize the adhesion and subsequent aggregation of multiple cell types. (iii) Depiction of DPAC approach to engineering aggregates of human luminal and myoepithelial cells. Scale bar is 30 µm. Images from [72]. (B) Side view illustration of a MAPLE DW print ribbon where the laser pulse creates a shock-wave to bioprint cells onto an underlying substrate with precise spatial control. 3-D tissues can be engineered by bioprinting onto an automated X-Y-Z stage. Image adapted from [75].

Analogous to the developing embryo, the signaling that guides morphogenesis begins immediately within presumptive organoids upon assembly. While the vast majority of organoid protocols initiate as spherical cell aggregates, many human organs, including the brain and spinal cord, heart, and gut tissues, develop from epithelialized tubes instead of spherical cell assemblies [37]. Therefore, several groups are using microfabrication to investigate how instructing non-spherical organoid morphologies upon assembly can enhance the biomimicry of subsequent morphogenesis events to yield organoids with anatomical micro-to-macroscale tissue cytoarchitecture. For example, we are integrating 2-D micropatterned substrates with neural organoid protocols to investigate how spatiotemporal control over the morphology of hPSC-derived neural stem cell (hNSC) aggregates affects subsequent neural tube-like morphogenesis

processes. Using micropatterned, multicomponent PEG-grafted substrates and copper-free click chemistry, we have demonstrated that polarized neural tube-like tissue formation and subsequent radial tissue growth can be recapitulated in a biomimetic manner by dynamically controlling the hNSCs' tissue morphology [65], [83]. In an improvement to their seminal cerebral organoid protocol [16], the Knoblich lab has used poly (lactide-co-glycolide) microfilaments as a scaffold to generate elongated 3-D hNSC aggregates. They show that applying this microscale control over hNSC aggregate assembly enhanced biomimicry of neural tube formation and the radial cytoarchitecture of subsequently formed cortical tissues as compared to organoids generated from spherical cell aggregates [26]. Furthermore, use of the Takeuchi group's double-coaxial flow method for 3-D cellular fiber tissue engineering could perhaps provide a scalable means of generating elongated or tube-like organoids [84]. Integration of such microfabricated methods to control the morphology of organoids upon assembly is an underdeveloped research area, which will likely be critical to controlling early morphogenesis events that subsequently yield tissues with anatomically biomimetic cytoarchitectures.

6.5. Spatiotemporal regulation with morphogen gradients

While microenvironmental control of cell fate is multifaceted, morphogens are arguably the most potent regulators of early tissue development in vivo. Morphogens are defined as small molecules (e.g. retinoic acid), growth factors (e.g. fibroblast growth factors, bone morphogenetic proteins (BMP), WNTs, etc.), or hormones that form diffusion gradients within tissues to regulate cell fate in a concentration dependent manner. Transient morphogen gradients generated by secretions from 'organizers' are well known spatiotemporal regulators of tissue morphogenesis in vivo [9], [85], [86]. The presence of analogous morphogen gradients arising during organoid

derivation is strongly suggested by the mere fact that cell phenotype diversity and tissue structure complexity increase drastically during organoid culture. Furthermore, Elly Tanaka's and Hans Clevers' groups have respectively observed the presence of Sonic Hedgehog and Wnt3 gradients within neural tube cysts [36] and the intestinal crypts of gut organoids [87] derived from mouse cells. Integrating engineering methods for spatiotemporal regulation of morphogen gradients within human organoids represent a potent, but yet under explored, approach for instructing anatomically biomimetic morphogenesis (**Fig. 2D**).

Spatiotemporal regulation of morphogen gradients in tissue engineering is traditionally achieved using microfluidics [88] or micro/nanoparticles [89]. Microfluidic devices can be engineered to produce morphogen gradients of diverse geometries and have been applied to 3-D stem cell culture. For example, the Kamm lab developed a microfluidic device in which diffusion driven, perpendicular, linear gradients of retinoic acid (RA) and SAG, a Sonic Hedgehog (Shh) signaling agonist, were generated across a 3D collagen hydrogel containing mouse embryonic stem cell-derived embryoid bodies (EBs) [90] (Fig. 5A). This mimics ventralizing morphogen gradients that arise in the developing spinal cord [91]. After a 5 day differentiation period, they observed a correlated 'ventral' localization of EBs generating HB9+ motor neurons, a RA and Shh-dependent spinal cell phenotype. Demers et al. conducted a similar microfluidic study but also included the presence of an opposing dorsalizing BMP4 gradient [92] (**Fig. 5B**). These examples demonstrate the power of using microfluidics to generate temporal morphogen gradients that spatially pattern 3-D stem cell differentiation. However, to apply this to human organoid morphogenesis, the microfluidics must be designed in a manner that accommodates the order(s) of magnitude increase in organoid size over the extended culture periods required for hPSC vs. mESC

differentiation. Also, the standard enclosed microfluidic design needs to be altered to permit extraction of the organoid after morphogen patterning.

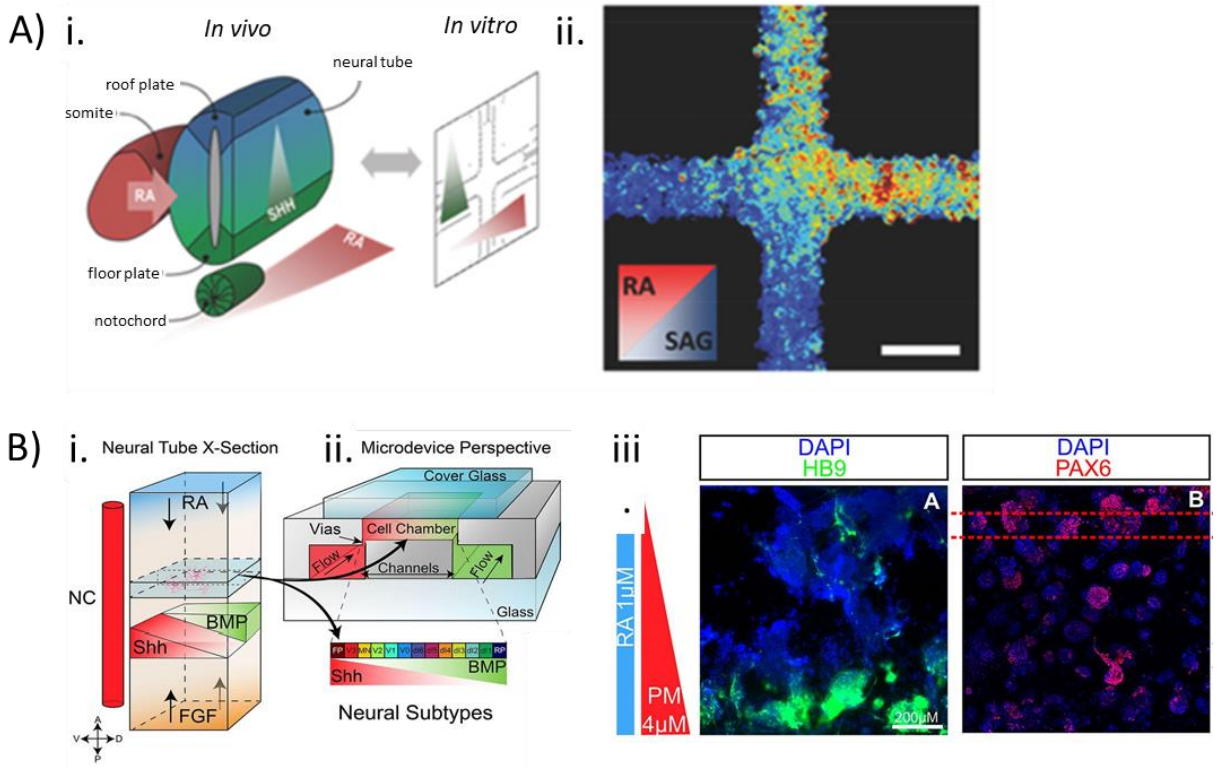

Figure 5: Exemplary methodologies for inducing morphogen gradients within organotypic cultures. (A) Demonstration of orthogonal retinoic acid (RA) and sonic hedgehog agonist (SAG) gradients on motor neuron differentiation of mouse embryoid bodies encapsulated within 3-D hydrogels. (i) Schematic comparing the morphogen concentration profiles in the developing neural tube to those created by the microfluidic device. (ii) Heat map demonstrating the local expression of GFP (i.e., red = high; blue = low) which corresponds to HB9+ motorneuron differentiation. Scale bar is 2 mm. Images from [87] (B) Graphical overview of microfluidic reconstruction of the neural tube. (i) Schematic of a neural tube cross-section highlighting (ii) the 100 μm 'slice' recreated by the microfluidic device. (iii) Spatial distribution of transcription factor expression within mouse embryoid bodies encapsulated within 3-D hydrogels that is consistent with in vivo neural tube expression. Scale bar is 100 μm. Images from [89].

Micro/nanoparticles can also be used to induce gradients by either local controlled-release or sequestering of morphogens (**Fig. 2D**). Whereas, microfluidics can only be used to induce trans-organoid morphogen gradients, micro/nanoparticles provide a means for inducing spatially discrete, internal morphogen gradients and in cases where complex organoid geometries prohibit the use of standard microfluidics. In 2001, the Saltzman group pioneered co-aggregation of microspheres and fetal rat cells to create 'neo-tissues' with 'programmable' synthetic microenvironments. They used PLGA microspheres pre-coated with poly-D-Lysine to promote co-

aggregation via electrostatic interactions with negatively charged sialic acid residues present in the cell membrane's glycocalyx [93]. This technique could be directly translated to organoid protocols to enable localized controlled-release of morphogens as demonstrated by the McDevitt lab. They used controlled release of retinoic acid from PLGA microspheres co-aggregated within mouse EBs to induce homogeneous, synchronous and organized spheroid cyst morphogenesis that resembled E6.75 mouse embryos with an exterior visceral endoderm encapsulating an epiblast cell layer [94]. These results demonstrate the potency of controlled and localized delivery of a single morphogen within organoids. However, during development multiple morphogens act in concert, i.e. in varied combinations and temporal periods, to specify tissue fate. To mimic such dynamics, the Alsberg and Murphy labs developed a dual gelatin and mineral-coated hydroxyapatite microparticle system to enable delivery of two morphogens with each having a discrete controlled release profile. Using this system, they were able to effectively recapitulate the two-stage process of endochondral ossification within human bone marrow-derived mesenchymal stem cell (hMSC) aggregates. Gelatin microparticles that rapidly released transforming growth factor-β1 induced chondrogenesis and alkaline phosphatase activity by week 2 of culture, and mineral-coated hydroxyapatite microparticles that provided sustained release of BMP-2 induced mineralized bone formation by week 5 [95]. The possibilities for instructing human organoid morphogenesis using microparticles is clearly wide-ranging. Furthermore, combining controlled release of growth factors with microparticles engineered for morphogen-specific sequestration [96] would make a versatile tool set for advanced gain and loss of morphogen gradient studies without the need for genetically engineered cell lines. To further advance this approach, methods to spatially concentrate microspheres within discrete

regions of microscale cell aggregates, versus a typical homogenous distribution, need to be developed to provide true spatiotemporal regulation of organoid morphogenesis.

7. Concluding Remarks

Human pluripotent stem cell-derived organoids are quickly becoming the biologists' culture tool of choice for exploring physiology and disease in a human genetic background. Patient specific, iPSC-derived organoids represent a significant advancement in experimental platforms for conducting personalized medicine studies due to their biomimicry of human tissue cell phenotype diversity and cytoarchitecture. However, there is still much room for improvement in standardizing and enhancing both of these aspects at the micro thru macroscale to generate tissues in vitro that could serves as anatomically mimetic analogues to their endogenous counterparts and potentially tissue transplants [9], [97]. Scientists' current reliance on uncontrolled morphogenesis produces deficiencies and inconsistences in organoid anatomy and cellular composition. Future advancements in applying tissue engineering methodologies to instruct multiscale organoid morphogenesis in a manner that mimics human development even further will be necessary to overcome this limitation.

The application of tissue engineering principles to organoid derivation protocols requires several conceptual changes from traditional tissue engineering practices. First, biologists are constantly discovering that the mixture of cell phenotypes within complex organs, e.g. brain [98], [99] and spinal cord [100], heart [101], intestine [102], lung [103], pancreas [104], etc., is highly diverse. Hence, it is not feasible to engineer anatomical and physiological mimetics of such organs ex vivo by deriving each cell phenotype separately and then bioprinting them with microscale precision

into analogous tissue cytoarchitectures. For such organs, in vitro morphogenesis of hPSCs/progenitor cell aggregates has been the only method to date that displays the potential to generate such levels of cell phenotype diversity and tissue cytoarchitecture mimicry. Second, tissue engineers traditionally focus on starting with vascularized tissue constructs, but inception of organ development in vivo is initially an avascular process quickly followed by subsequent vascularization in a stereotyped manner [37]. For this reason, most organoid morphogenesis protocols do, and may have too, begin as avascular microscale tissues. However, bioprinting blood vessels and nerves around the developing organoid to induce subsequent vascularization and innervation would be biologically appropriate. Third, current organoid morphogenesis protocols generate microscale tissues that grow at least one order of magnitude in size, and this is compounded even further in in vivo organ development. Therefore, the ideal tissue engineering platforms for organoid morphogenesis will be versatile enough to be applied effectively over multiple length scales, e.g. micro-to-centimeter [29]. Alternatively, they should at least permit facile isolation of a growing organoid, so it can be transferred to a secondary platform for continued culture. These conceptual shifts differentiate how tissue engineering methodologies would be applied to instruct organoid morphogenesis versus construct organotypic tissues.

As engineers have done before, now is the time to further blend engineering and biology to develop novel approaches for harnessing the innate emergent potential of hPSC-derived organoids. This can begin by integrating existing tissue engineering methods that generate hydrogels with spatially compartmentalized microenvironments and internal architecture, methods for controlling cellular cytoarchitecture during initial organoid assembly, and

approaches to spatiotemporally regulate morphogen gradients with organoid derivation protocols. This is facilitated by the proliferation of biomaterial and microfluidic tools over the past few decades and more recent advancements in 3-D and bioprinting, sacrificial molding, and photochemistry. However, due to the expansive experimental space of organoids, engineers should become well versed in developmental biology aspects of their respective tissues to reduce the problem's dimensionality to a manageable set of key factors. Additionally, the use of novel high-throughput screening and systems biology approaches to decipher the proper regimen of biochemical and biophysical factors necessary to instruct anatomically correct organoid morphogenesis will likely be necessary. We hypothesize that only a minimal set of instructive exogenous cues will be necessary to significantly advance the biomimicry of organoids due to their inherent and impressive morphogenetic potential. However, with all conundrums, the challenge lies in sifting through the possibilities to elucidate the simplistic solution, thereby making it a sophisticated one.

Chapter 2: Micro-Injection Molded, Poly (vinyl alcohol)-Calcium Salt Templates for Precise Customization of 3D Hydrogel Internal Architecture

The information presented in this chapter appears in the following publication:

McNulty, J. D.*, and Marti-Figueroa, C*. et al. (2019). Micro-injection molded, poly(vinyl alcohol)-calcium salt templates for precise customization of 3D hydrogel internal architecture. Acta Biomaterialia. https://doi.org/10.1016/j.actbio.2019.04.050

1. Introduction

Hydrogel biomaterials are used throughout the tissue engineering field as versatile scaffolds to support three-dimensional (3D) cell growth and shape the morphology of tissue constructs [68], [69], [105]–[108]. In vivo, normal tissue development and physiology relies upon proper cytoarchitectural organization at multiple length scales [37]. Hence, several methods have been developed for engineering the macro-to-microscale architecture of hydrogel scaffolds, including layer-by-layer 3D printing technologies, such as fused deposition modeling (FDM) and stereolithography (SLA) [68], [69], [109], [110].

Recently, these methods have been used to fabricate sacrificial templates that enable unprecedented, rapid casting of intricate architectures within hydrogel monoliths [69], [111], [112]. For example, Miller et al. used an FDM printer to create interconnected 3D lattices composed of water-soluble carbohydrate glass filaments [69]. Subsequently, the lattices could be encapsulated within hydrogels, and upon dissolution, leave behind channel networks suitable for generating microvasculature within prospective 3D tissues. Alternatively, sacrificial poly(vinyl alcohol) (PVOH), alginate, gelatin, and polyethylene glycol (PEG) templates casted within SLA

fabricated molds have also been developed to engineer microscale hydrogel architecture [70], [71], [113], [114]. While these approaches enable casting of complex hydrogel architectures, the fabrication techniques and sacrificial template materials impose several limitations. First, FDM and SLA/solvent casting fabrication techniques are not easily scaled for mass production due to extended manufacturing cycle times per sacrificial template. Second, carbohydrate glass templates are brittle and inelastic, suggesting limited durability during normal handling, whereas those of PVOH and alginate templates were not directly determined [69]–[71]. Third, current sacrificial template materials have only been proven to effectively cast complex geometries within bulk curing hydrogels such as PEG, fibrin, and methacrylated gelatin [69], [113]. Poorer dimensional fidelity was observed when Miller et al. used carbohydrate glass lattices to cast channels within diffusion limited, ionically crosslinked alginate hydrogels, a widely used tissue engineering scaffold and clinically approved biomaterial [44], [69], [71], [107], [115]. Alginate has several advantageous biomaterial properties for tissue engineering applications: facile and gentle cell encapsulation, ease of chemical modification via densely presented carboxylic acid groups, and enzymatic degradation mechanisms that are orthogonal to the mammalian genome [44], [107]. Thus, there remains a need to develop a scalable mass production process for generating durable sacrificial templates capable of accurately casting internal architectural features within both bulk curing and diffusion limited, ionically crosslinked hydrogels.

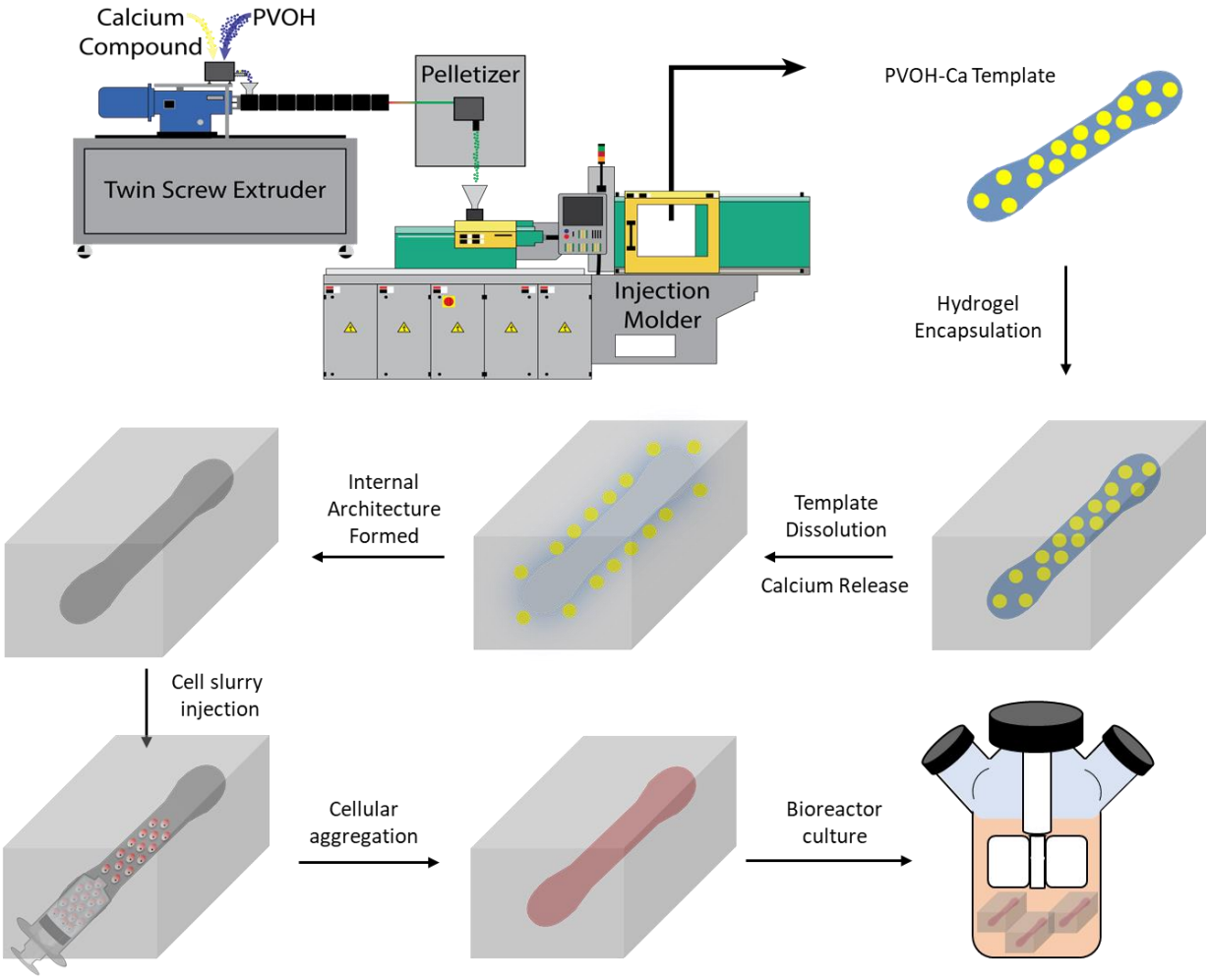

Schematic 1: Illustration of PVOH and calcium salt compounding followed by injection molding of a sacrificial PVOH-Ca template, which is subsequently encapsulated and dissolved within a hydrogel monolith.

To address these limitations, we have developed micro-injection molded PVOH-calcium salt composites (PVOH-Ca) as enhanced sacrificial templates for engineering 3D hydrogel molds with complex internal architecture (**Schematic 1**). Injection molding processes are unmatched in manufacturing scalability due to their automated, parallel production of finished polymer components within seconds [116]–[118]. Interestingly, calcium salt solubility was discovered to be a critical parameter in optimizing the PVOH-Ca composite's micro-injection molding processability and the resulting templates' durability and casting efficacy. PVOH composited with calcium acetate ($Ca(C_2H_3O_2)_2$) salts produced templates with enhanced mechanical properties

and calcium release upon aqueous dissolution, which accelerated the curing rate of alginate hydrogels at the template/hydrogel interface. PVOH- $Ca(C_2H_3O_2)_2$ templates were observed to cast 500 μm diameter channels within alginate hydrogel monoliths with an average dimensionality error of only 6.4 ± 7.2%, and equivalent performance was observed within bulk curing polyacrylamide hydrogels. To demonstrate process scalability and versatility, modular PVOH-$Ca(C_2H_3O_2)_2$ templates were injection molded, assembled into multicomponent Lego-like structures, and used to generate 3D channel networks within alginate and polyacrylamide hydrogels. The biocompatibility of the PVOH- $Ca(C_2H_3O_2)_2$ template-mediated hydrogel molding process was demonstrated in the presence of hESC-derived neurospheres. Additionally, the templates were used to engineer hESC-derived neuroepithelial organoids with a biomimetic, microscale cylindrical morphology. These results demonstrate the utility, biocompatibility, and versatility of PVOH-calcium acetate templates for sacrificially molding hydrogels with custom internal architectures for tissue engineering applications.

2. Materials and Methods

2.1 Materials

Sterile Pronova SLG1000 sodium alginate was purchased from Pronova Biopolymer. Calcium salts (CaCO3, $Ca(C_2H_3O_2)_2$, CaI2 and CaCl2), Eriochrome Black T, Ammonium Chloride, and Magnesium Chloride were purchased from Sigma Aldrich. Calcium sulfate and ammonia were purchased from Acros Organics. Polyacrylamide, tetramethylethylenediamine (TEMED), and ammonium persulfate were purchased from Biorad. Functionalized PEG-norbornene hydrogel materials were kindly provided by Prof. William Murphy (UW–Madison). Polypropylene 6061 aluminum and 316

stainless steel raw materials were purchased from McMaster-Carr Supply Company. Dexron-VI automatic transmission fluid (ATF) was purchased from Autozone and used as the imaging contrast dye for alginate perfusion.

2.2 Extrusion Compounding

Calcium salts were ground via mortar and pestle and sieved until less than 300 µm in dimension. The salts were hand mixed with PVOH (Monopol C100, Monosol Inc.) and conditioned under vacuum at 70 °C for 4 hours. The mixture was fed through a volumetric feeder (Tuf-Flex 100, Schenck Accurate) into a co-rotating twin screw compounding extruder (18 mm Leistritz AG) equipped with a screw designed with only feedforward elements and a 6 mm strand die (Schematic 1). Post compounding, the extrudate was run through a pelletizer to prepare the composite for injection molding. Compounding parameters are listed in Table 1.

2.3 Mechanical and Thermal Analysis

Tensile properties were measured using an Instron 5967 Universal Tensile Testing Machine (30 kN) with injection molded ASTM D638 Type V tensile bars elongated at 50 mm/min [119]. Thermogravimetric analysis (TGA) was performed on PVOH-Ca composite samples ranging from 20-60 mg within platinum pans (DSC Consumables Inc.) ramped to 600 ºC at 10 ºC/min (Q50 TGA, TA Instruments). Differential scanning calorimetry (DSC) was performed using hermetic aluminum pans (DSC Consumables Inc.) between 0 and 210 °C at a ramp rate of 10 ºC/min (Auto Q20, TA Instruments). Viscosity characterization was performed with a parallel plate rheometer (AR2000, TA Instruments) using injection molded discs with a 24.5 mm diameter and 2 mm thickness.

2.4 Micro-Injection Molding

Custom injection molds were designed with 3D modeling software (Solidworks 2014, Dassault Systems) and fabricated from 6061 aluminum blocks with a computer numerical control (CNC) vertical machining center (MiniMill 2, Haas) programmed using computer aided design/manufacturing (CAD/CAM) software (Master CAM X7, CNC Software, Inc.). All micro-injection molding was performed on a 38 ton Arburg Allrounder 270A machine with an 18 mm injection unit using processing parameters found in Table 1.

2.5 Complexometric Calcium Titration

A complexometric titration was performed to quantify the amount of Ca ions released from PVOH-Ca templates upon dissolution. 1.4 g of each composite was completely dissolved in 50 ml of deionized water. Then, 100 mL of 50 mM ethylenediaminetetraacetic acid (EDTA) was added to the solution to chelate all free Ca atoms. Eriochrome black T (EBT), a weaker chelating agent used as an indicator, was subsequently added to the solution causing a blue color that changes to pink upon its complexing with cations. Then, MgCl2 was titrated into the solution to react with the excess EDTA to completion, which was indicated by the solution's color change due to Mg's reaction with EBT. Once the solution turned pink, we could estimate the amount of Ca released upon PVOH-Ca template dissolution from the amount of titrated MgCl2. For each template composition, the titration results were compared with the total Ca salt content detected by thermogravimetric analysis (TGA).

2.6 Hydrogel Fabrication

2.6.1 Polyacrylamide

Polyacrylamide hydrogels were fabricated within custom polypropylene devices that suspended PVOH templates between inlet and outlet needles. Five milliliters of 12% acrylamide/bisacrylamide was prepared, and 100 uL of ammonium persulfate and 4 uL of TEMED were added to initiate the bulk polymerization reaction. After 5 min, the polyacrylamide solution was added to the device to completely encapsulate the suspended PVOH template. The solution polymerized for one hour. Then, the device was transferred to a 45ºC water bath and incubated overnight for PVOH dissolution.

2.6.2 Polyethylene Glycol (PEG)

PEG-norbornene (PEG-NB) hydrogels were fabricated within custom stainless-steel devices that suspended PVOH templates between inlet and outlet needles. 4.5 milliliters of 4% (w/v) PEG-NB was prepared to achieve 60% crosslinking [120]. The solution was added to the device to completely encapsulate the suspended PVOH template. The device was placed under a UV lamp and exposed to UV light at 365 nm wavelength for 20 seconds to induce polymerization. Then, the device was transferred to a 45ºC water bath and incubated overnight for PVOH dissolution. Post dissolution, the internal channel network was perfused with a mixture of green food colorant and water to enhance imaging contrast.

2.6.3 Alginate

Alginate hydrogels were fabricated within custom polypropylene and stainless-steel devices that suspended PVOH templates between inlet and outlet ports. To form alginate hydrogels, a 5 mL solution of 2% sodium alginate in sterile, deionized water was prepared by overnight mixing at 4 ºC. A $CaSO_4$-alginate slurry was prepared by adding 300 µL of 7.5% $CaSO_4$ in deionized water to the 5 mL of 2% sodium alginate solution. The slurry was pipetted into the device to encapsulate

the suspended PVOH template, and allowed to pre-gel for 10 min. Then the device was submerged in a room-temperature bath of 2% (w/v) $CaCl_2$ in deionized water overnight to induce bulk hydrogel gelation and completely dissolve the PVOH template. Post dissolution, the internal channel network was perfused with Dexron-VI automatic transmission fluid to enhance imaging contrast. For cell culture studies, stainless steel devices and components are autoclaved, and the devices are assembled and injected with Sodium Alginate and Calcium Chloride solutions in a sterile cell culture hood. The PVOH templates are sterilized in a cell cultured hood with UV for 1hr prior to assembly into stainless steel device.

2.6.4 Hydrogel Imaging and Reconstruction

Hydrogels were imaged using standard photography or a MicroCATII (Siemens AG.) at the University of Wisconsin Carbone Cancer Center's small animal imaging facility. The Digital Imaging and Communications in Medicine (DICOM) image stacks were then reconstructed and converted into STL graphic bodies using Mimics software (Materialize NV.). Image analysis was performed using a combination of Magics (Materialize NV.), MeshLabs, and Solidworks (Dassault Systemes).

2.7 Statistical Analysis

RStudio® was used to conduct all statistical analysis. Experimental replicates or number of groups are detailed in figure legends, and error bars show standard deviations. One-way ANOVAs with post-hoc Tukey-Kramer tests were conducted to determine statistical significance. $P < 0.05$ was considered statistically significant.

Twin Screw Extruder Processing Parameters	
Zone 1 (°C)	160
Zone 2 (°C)	165
Zone 3 (°C)	170
Zone 4 (°C)	173
Zone 5 (°C)	175
Zone 6 (°C)	177
Zone 7 (°C)	178
Zone 8 (°C)	180
Load (%)	< 40
Screw Speed (rpm)	50-70
Injection Molding Process Parameters	
Mold temperature (°C)	46
Barrel temperature (°C)	190-200
Injection pressure (bar)	1250-1400
Holding pressure (bar)	1000
Injection speed (cm^3/s)	55
Holding time (s)	2
Cooling time (s)	20

Table 1: Twin screw extrusion and microinjection molding processing parameters.

3. Results

3.1. Injection molded, sacrificial PVOH and PVOH-$CaCl_2$ templates

In contrast to brittle carbohydrate glass sacrificial templates[3], we opted to produce sacrificial templates using durable, water-soluble, and biocompatible PVOH similar to Tocchio et al. [71]. Micro-injection molding was chosen as the fabrication technique to mitigate manufacturing scalability concerns. Aluminum molds were CNC-milled to produce sacrificial PVOH templates with a lattice geometry consisting of cylinders that transitioned from 3 to 1 mm in diameter (**Fig. 1**). To evaluate their hydrogel molding utility, the templates were encapsulated within

polyacrylamide, PEG, and alginate monoliths, and dissolved overnight in a water bath to generate hydrogels with replicate internal architecture. Post template dissolution, bulk curing polyacrylamide and PEG hydrogels displayed discernable internal channel lattice networks (**Fig. 2A-B**). The PEG hydrogel's channels displayed a higher deviation from the PVOH template's dimensions presumably due to the hydrogel's characteristic swelling [120], [121] (**Fig. 2H**). However, a series of disconnected and non-uniform voids were generated in alginate hydrogels, suggesting that the PVOH template dissolved prior to the inward diffusion of crosslinking Ca^{2+} ions (**Fig. 2C and 2E-F**).

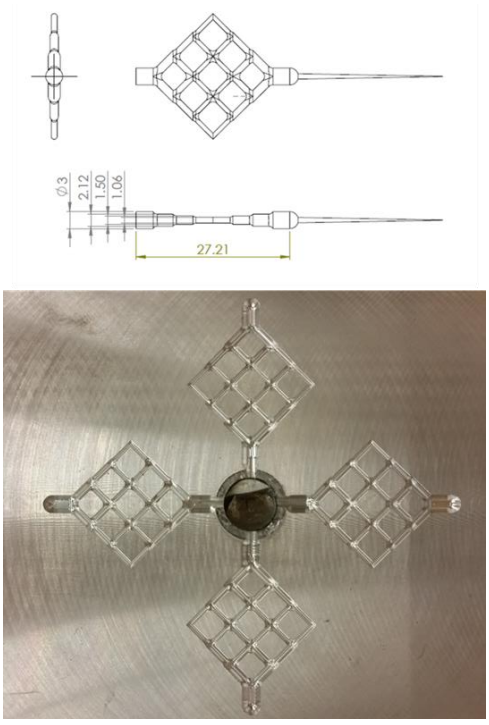

Figure 1: CAD drawing of the 2D, sacrificial PVOH lattice templates with associated CNC-milled aluminum mold. All dimensions in millimeters.

To enable effective sacrificial molding of alginate hydrogels, we hypothesized that compounding calcium salts into the PVOH template material would accelerate the crosslinking rate at the template/hydrogel interface and enable more precise sacrificial molding. PVOH was

compounded with 5% and 10% (w/w) $CaCl_2$ using twin screw extrusion, and the PVOH-$CaCl_2$ composite was injection molded into a lattice geometry (**Fig. 2E**). Sacrificial molding with PVOH-$CaCl_2$ templates yielded continuous channel networks within alginate hydrogels indicating that release of the compounded calcium ameliorated casting efficacy (**Fig. 2D-G**). Metrological analysis of cross-sectioned hydrogels (**Fig. 2E-G**) revealed that compounding 10% vs. 5% (w/w) $CaCl_2$ into the PVOH lattice template significantly improved molding of the channel network geometry (**Fig. 2H**). However, the casted architecture's dimensions still deviated from those of the PVOH-$CaCl_2$ template by ~30%. Thus, the addition of $CaCl_2$ to PVOH template material significantly improved molding of internal architecture within ionically crosslinked alginate hydrogels, but the molding fidelity could be further improved.

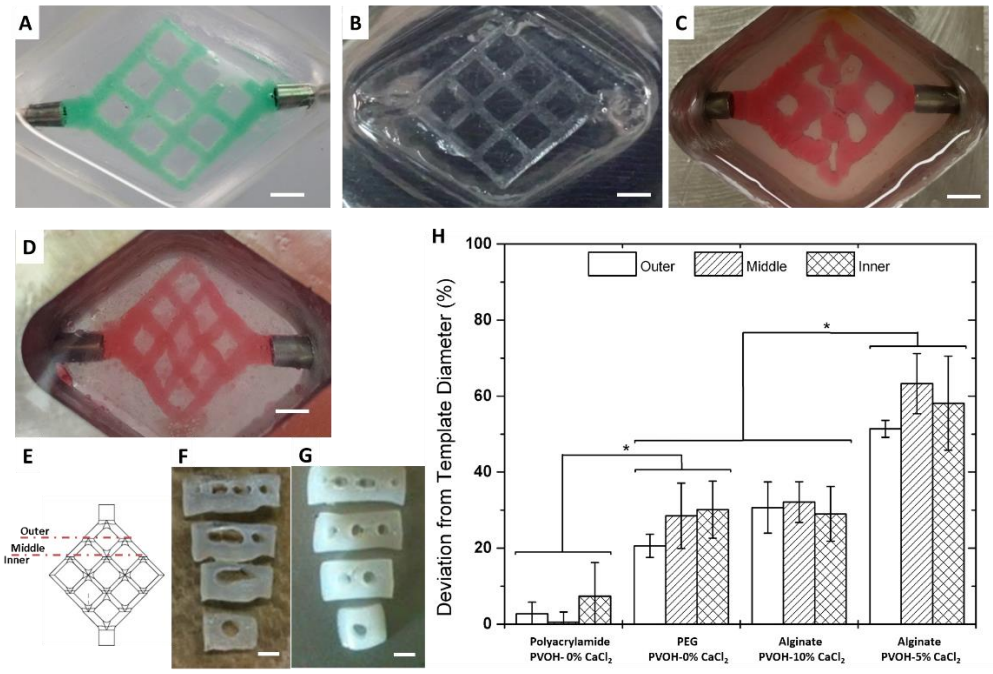

*Figure 2: Channel laden hydrogels molded using PVOH and PVOH-$CaCl_2$ sacrificial templates. (A) polyacrylamide, (B) PEG, and (C) alginate hydrogels cast using PVOH lattices. (D) Alginate hydrogel cast using a 10% (w/w) loaded PVOH-$CaCl_2$ template. (E) Schematic of cross-sectional hydrogel slices made to measure outer, middle, and interior channel diameters. Representative cross-sectional images of alginate hydrogels cast using (F) PVOH and (G) 10% PVOH-$CaCl_2$ templates. (H) Percent deviation of hydrogel channels' diameter from the sacrificial template's dimensions. Data combined from duplicate experiments to yield n=8, 16 and 24 for outer, middle, and inner channels, respectively. Error bars represent standard deviation; *P<0.05, One-way ANOVA; Scale bars are 3 mm.*

3.2. Optimizing mechanical properties of PVOH-Ca templates

Although the PVOH-$CaCl_2$ sacrificial molding results were promising, the addition of $CaCl_2$ into the PVOH substrate also yielded undesirable fabrication side effects. Notably, the composite was much more difficult to process via extrusion and injection molding than neat PVOH material. For example, thermal degradation of the 10% PVOH-$CaCl_2$ composite was apparent both visually and aromatically. According to a prior cement study, dissolved Ca^{2+} ions can produce crosslinking-like interactions between hydroxyl groups within the PVOH polymer backbone [122]. Since $CaCl_2$ solubility in water is high and increases with temperature (**Table 2**), it was hypothesized that the thermal processing of extrusion and injection molding amplified Ca^{2+} crosslinking within the polymer composite. Increased polymer chain cross-linking would make PVOH-$CaCl_2$ templates more difficult to injection mold, and it could decrease the release of Ca^{2+} ions upon the templates' aqueous dissolution. Therefore, we investigated whether compounding PVOH with calcium salts of lower solubility would minimize crosslinking interactions during material processing. PVOH was compounded with 10% (w/w) calcium iodide (CaI_2), calcium acetate ($Ca(C_2H_3O_2)_2$), or calcium carbonate ($CaCO_3$) salts, which are listed in order of decreasing solubility (**Table 2**) and each composites' mechanical and calcium release properties were analyzed in detail (**Fig. 3 and 4**).

IUPAC-NIST Solubility Table (g/100cc water)						
Compound	Formula	Temperature (°C)				
		0	10	20	30	40
Calcium Carbonate	$CaCO_3$	0	0	0	0	0
Calcium Sulfate	$CaSO_4$	0.2	0.2	0.3	0.3	0.3
Calcium Acetate	$Ca(C_2H_3O_2)_2$	37.4	36	34.7	33.8	33.2
Calcium Iodide	CaI_2	64.6	65.3	66	67.6	70.8
Calcium Chloride	$CaCl_2$	59.5	64.7	74.5	100	128

Table 2: Quantification of water solubility of various calcium compounds adapted from IUPAC-NIST solubility database [29].

Tensile strength tests on injection molded PVOH-Ca ASTM D638 Type V specimens showed that the compounded calcium salts decrease the material's ductility, i.e. strain at break, and increases its modulus and ultimate axial tensile strength (UTS) compared to neat PVOH (**Fig. 3A and 3B**). The Ca salts' effect on the composite's modulus and UTS is directly correlated with their solubility while the effect on the composite's ductility is inversely correlated. These results agree with traditional polymer filler theory considering polymer chain crosslinking by solvated Ca^{2+} ions. Notably, sacrificial templates produced from PVOH-$Ca(C_2H_3O_2)_2$ or $CaCO_3$ composites versus carbohydrate glass have enhanced handling durability due to a 50-fold increase in ductility [69].

Rheological measurements were conducted to assess each PVOH-Ca composite's viscosity and thereby relative ease of manufacturing by extrusion and injection molding. Using a parallel plate rheometer to measure viscosity at continuous shear rates, PVOH-CaI_2 or -$CaCl_2$ composites displayed a viscosity ~10 fold higher than PVOH-neat, -$Ca(C_2H_3O_2)_2$, or -$CaCO_3$ across an order of magnitude shear rate range (0.1-1 per sec) (**Fig. 3C**). Similar to modulus and UTS data, the composite's viscosity was directly correlated to Ca salt solubility. The decreased viscosity of PVOH-neat, -$Ca(C_2H_3O_2)_2$, or -$CaCO_3$ composites was observed to facilitate extrusion and injection molding processes as well as minimized noticeable polymer degradation compared to PVOH-CaI_2 or -$CaCl_2$. As discussed later, optimizing the PVOH-Ca composite's viscosity was critical for feasible injection molding of sacrificial templates with microscale dimensions, i.e. micro-injection molding.

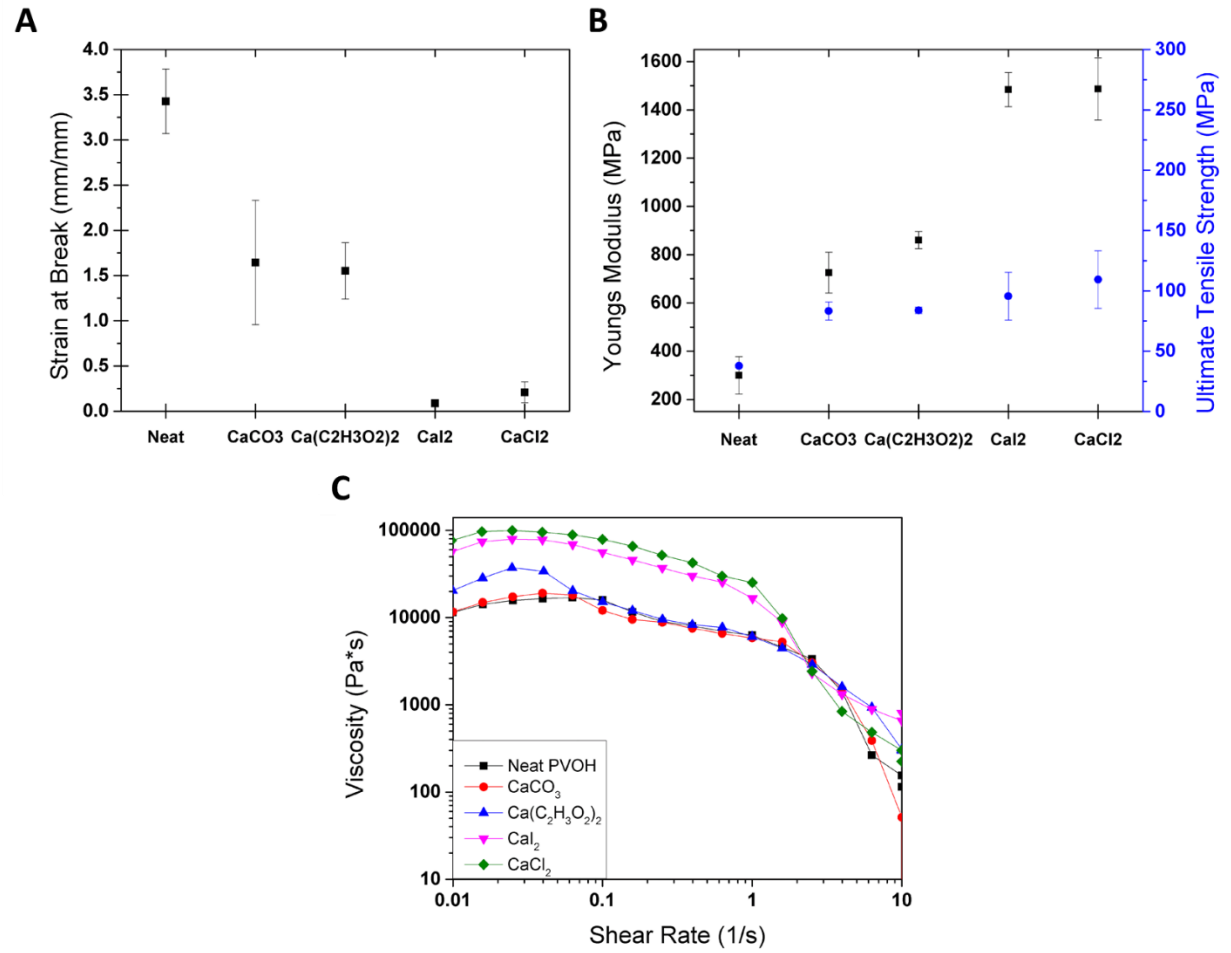

Figure 3: PVOH-Ca composite materials' mechanical property analyzed at 25 °C. Tensile test of injection molded PVOH and PVOH-Ca materials' (A) ductility and (B) Young's modulus and ultimate tensile strength (UTS), n=10 experimental replicates and error bars represent standard deviation. (C) Rheological analysis of each materials' viscosity over a range of shear rates.

3.3. Optimizing calcium release properties of PVOH-Ca templates

The lower solubility of calcium acetate and carbonate salts made them ideal compounding agents for producing PVOH-Ca composites with optimal mechanical properties. However, it remained unknown how their decreased solubility would affect Ca^{2+} ion release upon composite aqueous dissolution. To calculate this quantity, we first needed to know the actual weight percent of calcium salt in each PVOH composite. Since PVOH but not the compounded calcium salts decompose below 600ºC, thermogravimetric analysis (TGA), which measures mass loss over

increasing temperatures, was conducted on PVOH compounded with 10% (w/w) calcium salts. As shown in **Fig. 4A**, the compounded salts persisted in the ash content at 600 ºC. When normalized to the remaining neat PVOH ash, the salt masses were found to be consistent with compounded values except for the PVOH-CaI_2 composite. Considerable PVOH degradation was observed during PVOH-CaI_2 extrusion, and this likely skewed the TGA results since degraded PVOH does not burn off at 600ºC. Furthermore, the TGA curves revealed that the onset of degradation (first curve inflection point) of all PVOH-Ca composites occurred at lower temperatures than the neat composite, potentially indicating disruption of PVOH crystallinity by Ca^{2+} ions. This further corroborates the presence of intra-composite PVOH polymer/ Ca^{2+} crosslinking.

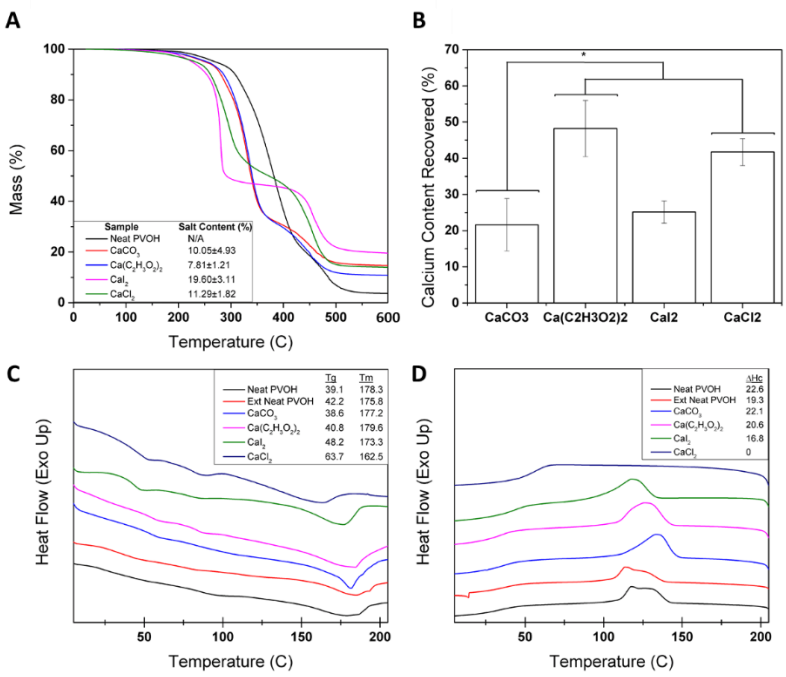

*Figure 4: Analysis of the PVOH-Ca composite composition, material, and calcium release properties. (A) Representative thermogravimetric scans, n=3 experimental replicates. (B) Complexometric calcium titration results, n=5 experimental replicates, *P<0.05, One-way ANOVA. Differential scanning calorimeter's (C) second heating and (D) first cooling curve traces of neat and extruded (Ext) PVOH and PVOH-Ca composites.*

A complexometric calcium titration was performed on the PVOH-Ca composites to assess the amount of Ca^{2+} ions released upon dissolution in deionized water (**Fig. 4B**). Calculating from the titration and TGA data, the average percent of released Ca^{2+} content was determined to never be greater than ~50%. Also, the Ca^{2+} released from PVOH-$Ca(C_2H_3O_2)_2$ or -$CaCl_2$ composites was equivalent and significantly higher than that released from PVOH-CaI_2 and -$CaCO_3$. The lower Ca^{2+} content release from PVOH-CaI_2 composites could be due to the considerable observed polymer degradation during extrusion and the skewed TGA data whereas that of the PVOH-$CaCO_3$ is likely due to the salt's low solubility in water (**Table 2**).

As a final analysis to explain <50% calcium recovery from PVOH-$Ca(C_2H_3O_2)_2$ or -$CaCl_2$ composites, we performed differential scanning calorimetry (DSC). This analytical technique measures the thermal energy input required to induce a 1 ºC temperature change in the sample, thereby allowing characterization of the composite's glass transition (T_g) and melting (T_m) temperatures and crystallization enthalpy (ΔH_c). In DSC second heating curves (**Fig. 4C**), the T_g is indicated by the curve's first inflection point, and the T_m is indicated by the curve's last inflection point. We observed a direct correlation between the composites' T_g and an inverse correlation between the composites' T_m relative to its calcium salt's solubility (**Table 2**). Thus, crosslinking interactions between calcium ions solvated during the extrusion and injection molding process with the composite's PVOH polymers correlates directly with the salts' solubility. In the DSC cooling curve (**Fig.4D**), the ΔH_c is calculated as the area under the curves' exothermic peak. In analyzing this material property, we observed an inverse correlation between the composites' ΔH_c and the compounded calcium salt's solubility. Moreover, the presence of a double exothermic peak in the neat PVOH and extruded neat PVOH samples versus the single peak in the extruded PVOH-

Ca samples indicates that less types of crystals are being formed in salt containing samples. Collectively, the DSC results strongly suggest that the total compounded calcium content is not released from the PVOH-Ca composites upon dissolution due to intra-composite PVOH polymer/Ca^{2+} crosslinking which disrupts polymer crystallization. Importantly, our detailed analysis of each composites mechanical and calcium release properties imply that PVOH-$Ca(C_2H_3O_2)_2$ templates would provide enhanced sacrificial molding capabilities, handling durability, and micro-injection molding feasibility due to its comparatively high calcium ion release upon aqueous dissolution (**Fig. 4B**), moderate ductility (**Fig. 3A-B**), and low viscosity (**Fig. 3C**).

3.4. Micro-injection molded PVOH-$Ca(C_2H_3O_2)_2$ template

To fabricate sacrificial templates with microscale feature dimensions, a micro-injection mold was CNC-milled in aluminum with a fiber template geometry 2.2 cm in length that immediately tapered from a 3mm inlet/outlet diameter to a main fiber diameter of 500 μm (**Fig. 5A and Fig. 6)**. PVOH- $Ca(C_2H_3O_2)_2$ templates of 10% (w/w) salt loading were successfully microinjection molded. However, fabrication of equivalent PVOH-CaCl2 templates failed indicating the enhanced processability of the PVOH- $Ca(C_2H_3O_2)_2$ composite material. Post sacrificial molding of alginate hydrogels using the PVOH- $Ca(C_2H_3O_2)_2$ templates, the resulting micro-channels were filled with pigmented oil for photographing, and they were quantitatively analyzed by micro-CT imaging and reconstruction analysis (**Fig. 5A**). Dimensional analysis of the microCT reconstructions revealed that the molded channel diameter deviated from the template geometry by an average of 6.4 ± 7.2% at any point along its long axis, i.e. 10 measurements per molded channel (**Fig. 5B**). This demonstrates repeatable and precise casting of microscale

architecture within diffusion limited, ionically crosslinked alginate hydrogels. Additionally, similarly dimensioned neat PVOH templates left no discernable micro-channel within alginate monoliths (data not shown).

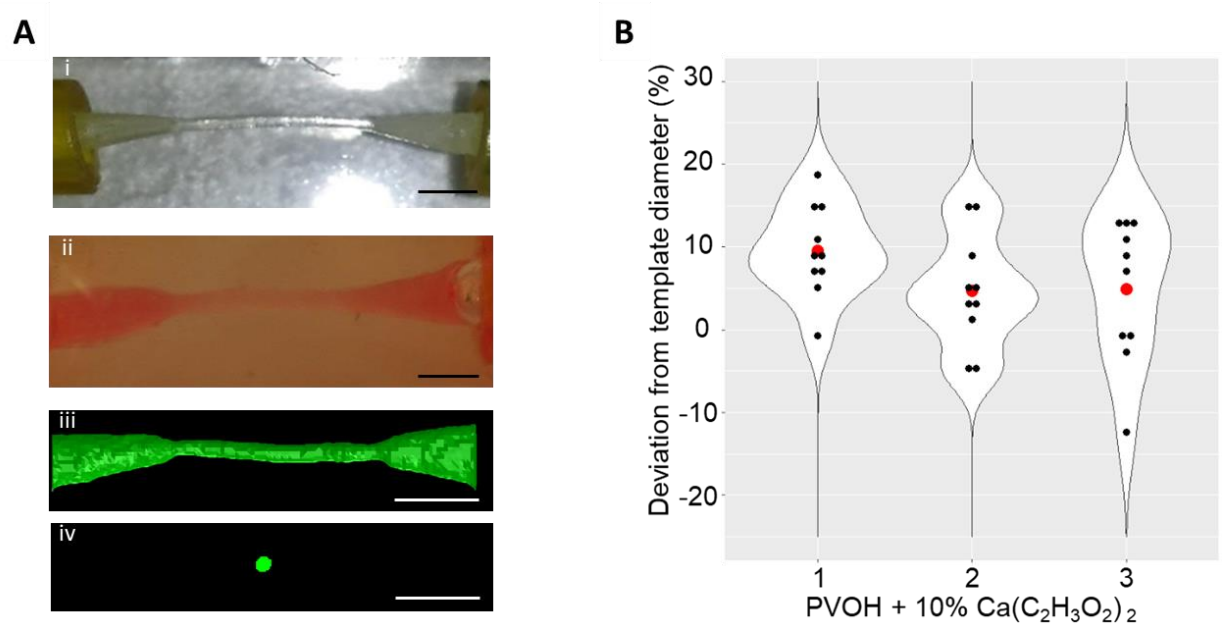

Figure 5: Sacrificial molding using PVOH-Ca(C2H3O2)2 templates. Representative images of (A) micro-injection molded 10% (w/w) PVOH-Ca(C2H3O2)2 sacrificial fiber templates (i), the molded channel within an alginate hydrogel (ii), and a profile (iii) and cross-sectional (iv) view of the microCT-imaged channel geometry. (B) Dimensional analysis was performed on microCT scan reconstructions (A, iii and iv) of three separately cast alginate hydrogels at 10 points along each micro-channel. Black dots represent individual measurements, red dot represents the mean. Scale bars are 3 mm.

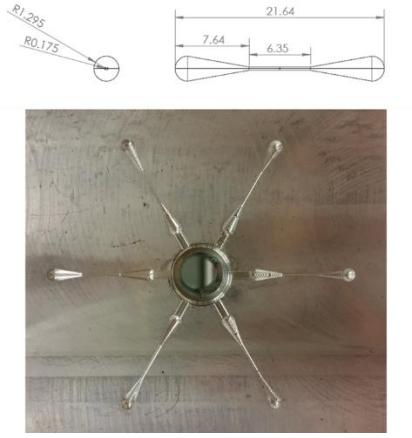

Figure 6: CAD drawing of the 2D, sacrificial filament templates with associated CNC-milled aluminum mold. All dimensions in millimeters.

3.5. Biocompatibility of the PVOH-Ca template sacrificial molding process

To verify biocompatibility of the PVOH-Ca($C_2H_3O_2$)$_2$ templates, H9 hESC-derived neurospheres were co-encapsulated within alginate hydrogels during the sacrificial molding process (**Fig. 7B**). Neuroepithelial cells (NECs) were derived using the E6 protocol [123] and re-seeded at 180,000 cells/well in 96 well plates. The cells aggregated over 2 days of culture in E6 media to formed spheroids that were collected and mixed into 2% (w/v) alginate pre-hydrogel solutions. Then, the alginate/neurosphere solution was pipetted into stainless steel hydrogel molding devices and encapsulated the suspended sacrificial PVOH-Ca($C_2H_3O_2$)$_2$ template. After template dissolution over 24 hours in E6 media under standard culture conditions, the hydrogels were fixed and sectioned to analyze cell viability within the neurospheres using TUNEL staining (**Fig. 7A**). As a cell death control, a cohort of hydrogel samples were subjected to a freeze-thaw cycle prior to fixation. As a positive control, alginate hydrogels containing neurospheres in the absence of sacrificial templates were also analyzed. TUNEL staining revealed that the presence of the sacrificial template had no significant deleterious effect on cell viability compared to Freeze-Thaw (negative) and non-template (positive) controls (**Fig. 7A and 7C**). Moreover, minimal cell death was observed during the sacrificial molding process overall (**Fig. 7A**). These results indicate that the PVOH-Ca($C_2H_3O_2$)$_2$ template and sacrificial molding process is compatible with standard cell culture.

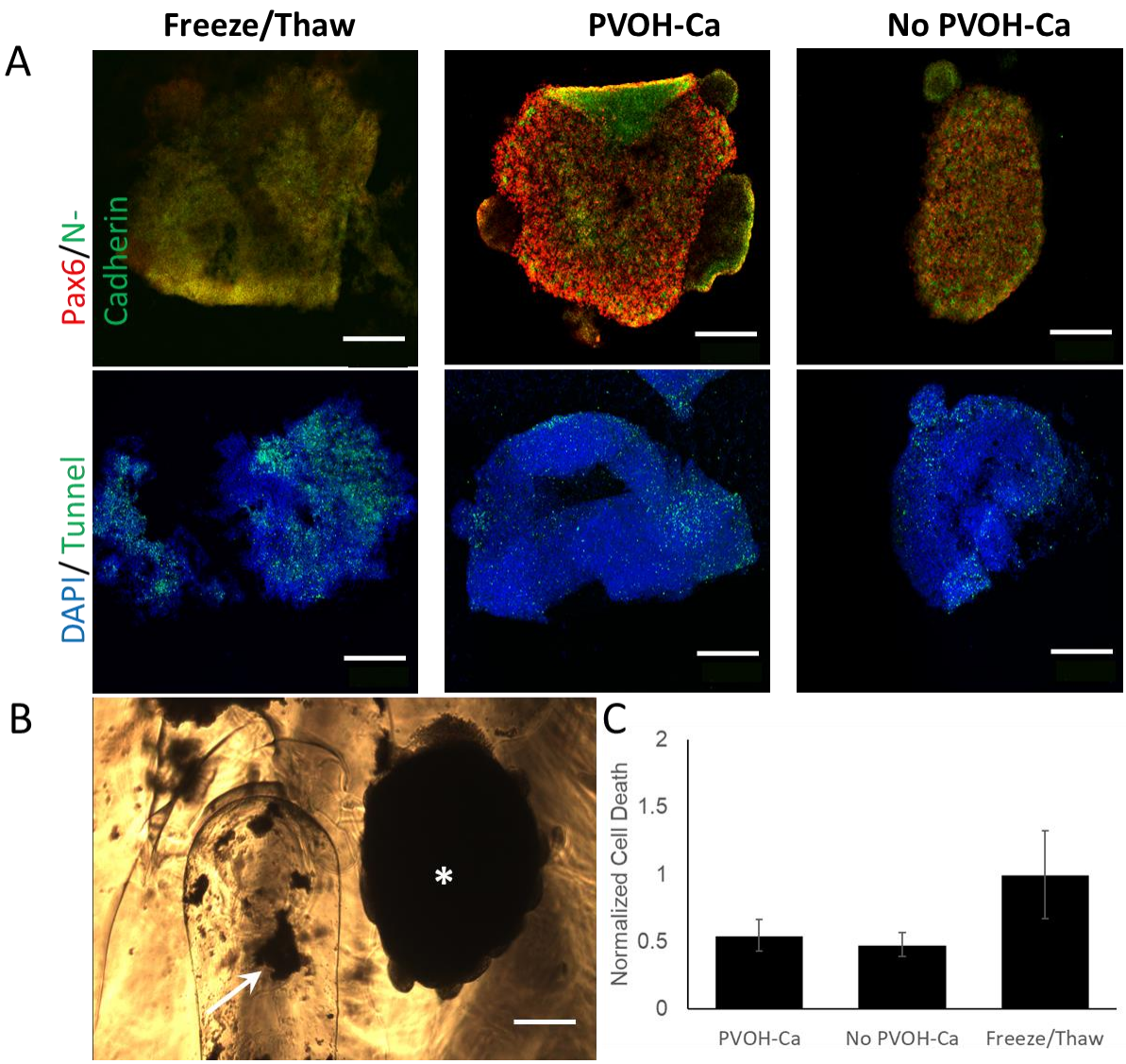

Figure 7: Biocompatibility of sacrificial molding using PVOH-Ca(C2H3O2)2 templates. (A) TUNEL stain of hESC-derived neurospheres that were cultured within alginate hydrogels (right), PVOH-Ca(C2H3O2)2 template molded alginate hydrogels (middle), and alginate hydrogels that were freeze/thawed to serve as a cell death control (left). (B) Representative image of a neurosphere cultured within a PVOH-Ca(C2H3O2)2 template molded alginate hydrogel. Arrow indicates dissolved template remnants in the channel. Asterisks indicates a hESC-derived neurosphere. (C) Normalized quantification of the number of cells that survived in all 3 conditions. Scale bars are 200μm.

3.6. Scalable 3-D Molding of Hydrogel Architecture

Lastly, we attempted to demonstrate the injection molded PVOH-Ca$(C_2H_3O_2)_2$ templates' 3D scalability and versatility. Sacrificial templates with a manifold design that connected via an interference fit with the previous lattice geometry were fabricated (**Fig. 8A**). This enabled

assembly of 3D PVOH-Ca($C_2H_3O_2$)$_2$ templates in a Legos®-like manner (**Fig. 8B**), and the assembly was used to sacrificially mold 3D channel networks within polyacrylamide (**Fig. 9**) and alginate hydrogels (**Fig. 8C**). After template dissolution, the hydrogels were scanned using a micro-CT and image reconstruction verified the resulting 3D channel networks' patency and continuity (**Fig. 8D**). Thus, the design and injection molding of modular, PVOH-Ca($C_2H_3O_2$)$_2$ components that can be assembled into 3D sacrificial templates represents a scalable and potentially limitless approach to precisely customize the internal architecture of both bulk curing and ionically crosslinked hydrogels.

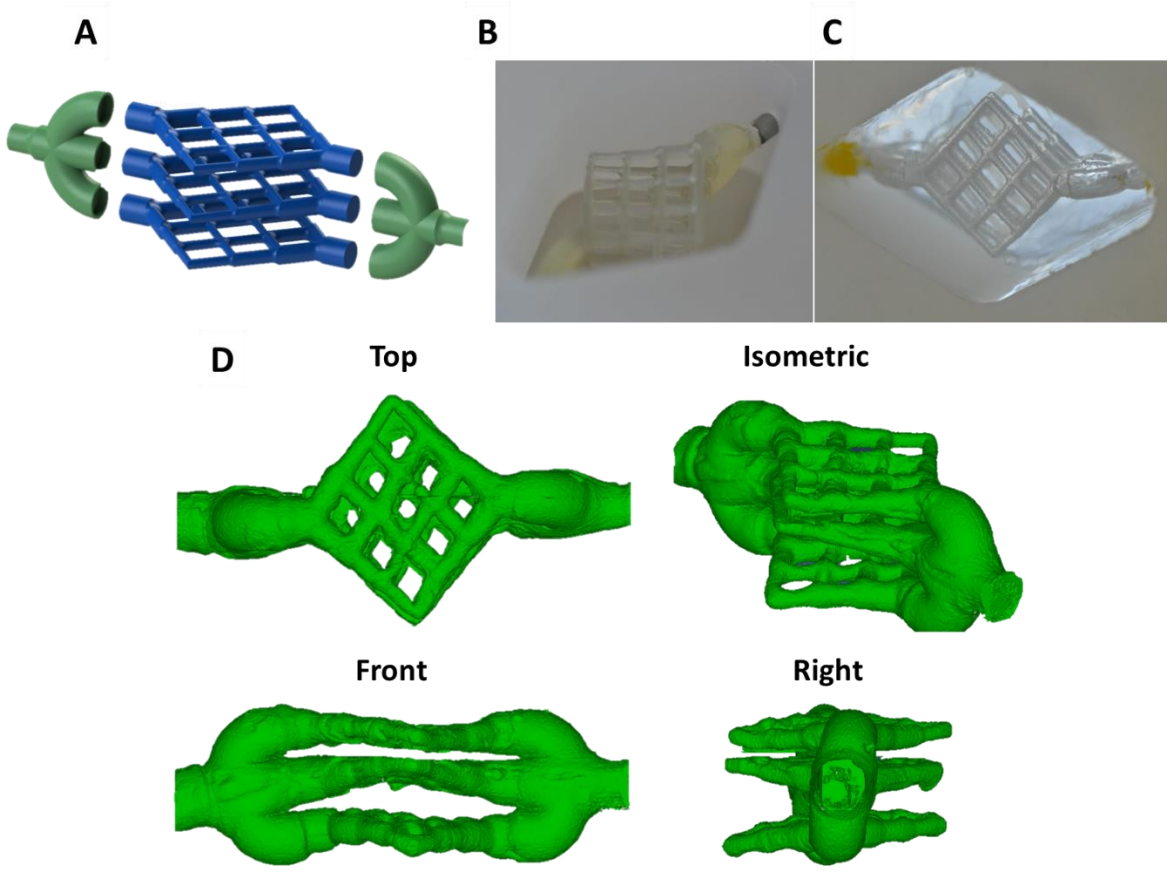

Figure 8: Modular 3D sacrificial molding using PVOH- Ca($C_2H_3O_2$)$_2$ templates. (A) Exploded CAD model of modular, 3D sacrificial template design. (B) An assembled 3D template as micro-injection molded, and (C) a sacrificially molded channel network within an alginate hydrogel. (D) microCT scanned reconstruction of the channel network within an alginate monolith. Scale bars are 3 mm.

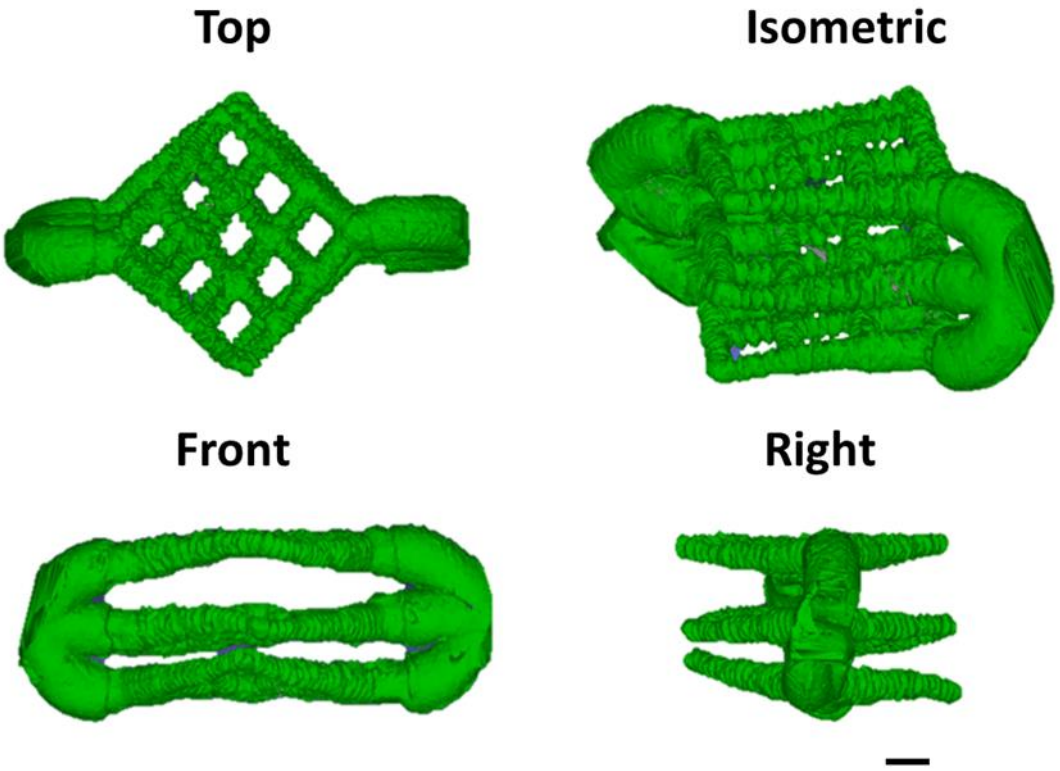

Figure 9: MicroCT scanned reconstruction of a 3D channel network within a polyacrylamide monolith. Scale bar is 3mm.

4. Discussion

The ability to engineer tissue constructs with biomimetic morphologies and cytoarchitectures has been greatly enhanced by the development of techniques to fabricate biomaterial scaffolds with macro-to-microscale features. Sacrificial molding is a promising and scalable technique for rapidly casting complex, internal architectures within hydrogel scaffolds. Yet, while previous studies demonstrated its efficacy using bulk curing hydrogels, noticeably less molding fidelity was observed when applied to diffusion limited, ionically crosslinked hydrogels such as alginate. Furthermore, these studies performed limited to no quantitative analysis of their sacrificial molding approach's feature casting fidelity [69], [71], [111].

Here, we fabricated injection molded, PVOH-Ca templates to facilitate and enhance sacrificial molding within ionically crosslinked hydrogels. Injection molded PVOH templates effectively mold bulk curing hydrogels such as polyacrylamide and PEG. However, the addition of calcium salts to the sacrificial templates was both necessary and sufficient to enable precise molding of microscale features within alginate monoliths. Extensive characterization unveiled that the PVOH-Ca composite mechanical, material, and calcium release properties could be tuned based on the compounded calcium salt's solubility. Also, this analysis proved that PVOH- $Ca(C_2H_3O_2)_2$ composite possessed enhanced manufacturability and sacrificial template properties, which were further demonstrated by precise casting of microscale 2D and 3D internal architecture within alginate hydrogels.

5. Concluding Remarks

The micro-injection molded, PVOH- $Ca(C_2H_3O_2)_2$ templates described herein were developed to maximize production scalability and hydrogel engineering design versatility. We have demonstrated their applicability to sacrificial molding of both bulk-curing and ionically crosslinked hydrogel monoliths, and the templates can be mass-produced using micro-injection molding. The complexity of internal hydrogel architecture that can be molded is only limited by the need to create injection molds for each template design, which can be costly if template designs features of < 300um are desired. Here, we demonstrated molding of channels within hydrogel monoliths but this platform can be used for any geometry, and once the PVOH-$Ca(C_2H_3O_2)_2$ templates are fabricated, the scalability of hydrogel engineering by sacrificial molding is unmatched. Modular template geometries can even be fabricated and assembled in

Lego®-like configurations for rapid and precise customization of hydrogels with complex, 3D internal architecture.

In the following chapters, the feasibility for micro-injection molded, PVOH- $Ca(C_2H_3O_2)_2$ sacrificial template's to be used for tissue engineering of neuroepithelial organoid morphology will be explored. Unlike prior efforts to engineering neural organoid morphology [26], this approach was designed to maintain a microscale cylindrical neuroepithelial organoid morphology that is mimetic of the developing neural tube [124]. In chapter 3, we will attempt to use this platform to develop the first standardize formation of hPSC cylindrical aggregates, which would be analogous to EB formation in the initial stages of cerebral organoid differentiation[16], [23], [26]. In chapter 4 we will differentiate the engineered cylindrical aggregates into neural epithelial organoids and investigate the optimal conditions to form neuroepithelial tube organoids exhibiting a biomimetic, singularly polarized, neuroepithelial cytoarchitecture throughout length of the organoid.

Chapter 3: Engineering 3-D, microscale cylindrical cell aggregates using alginate hydrogels with PVOH-Ca template-casted internal architecture.

1. Introduction

Organoids are 3D tissues in a dish derived from stem cells that undergo spontaneous morphogenesis leading to a diversity of cell types and microscale cytoarchitectural structures that mimic in vivo developmental tissues. The ability of organoids to generate high cell diversity and microscale self-organization has allowed researchers to develop cerebral organoids in vitro that mimic the in vivo neural development process to generate remarkable biomimetic microscale organization.

Cerebral organoid formation typically occurs in 3 distinct stages: Embryoid body (EB) formation, neural epithelial organoid formation, and finally cerebral organoid formation (**Fig. 1A**). EBs are 3D human pluripotent stem cell (hPSC) spherical aggregates typically formed by centrifugation of a cell suspension in 96 well plates or aggrewell plates. Once formed, EBs are cultured for 5 days to undergo germ layer specification yielding aggregates with bright and smooth surfaces. In the next stage of differentiation, EBs undergo neural induction for 5 days in which the bright and smooth surfaces of the aggregates will form optically translucent neuroepithelium between the 7^{th} and 10^{th} day of culture. Finally, the neural epithelial organoids are embedded in Matrigel to undergo cerebral differentiation, during which the optically translucent neuroepithelium typically gives rise to neuroepithelial buds from which the microscale cerebral structures of the cerebral organoids will emerge. and after, further Corticogenesis is achieved via long term culture of such tissues in spinner/shaker flask bioreactors [16].

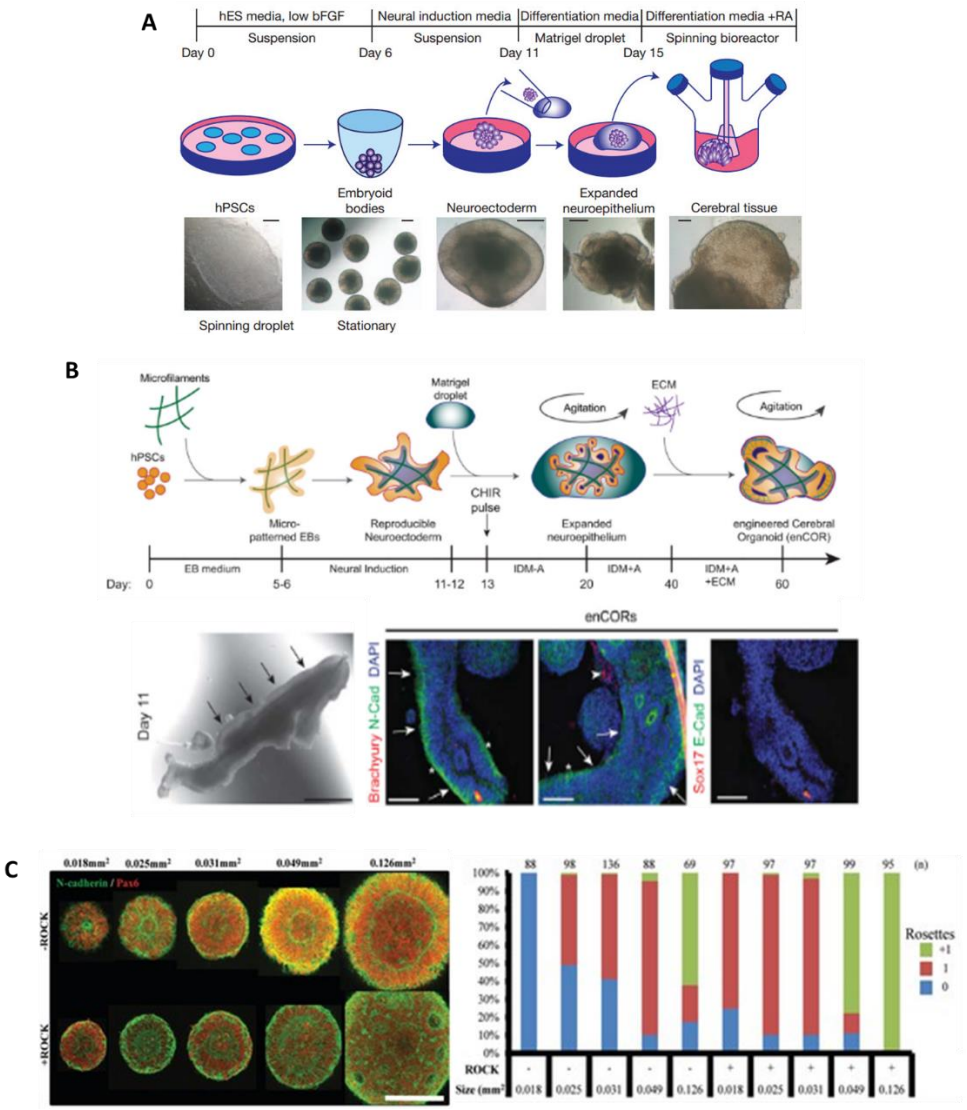

Figure 1: Cerebral organotypic platforms using (A) 3D spherical organoids, (B) 3D engineered elongated organoids, and (C) 2D micropatterned rosettes. A) Timeline of spherical cerebral organoid formation. On day 0, ESCs or iPSCs are plated in ultra-low binding 96-well plates in hES media with low bFGF and 50uM ROCK inhibitor (germ layer differentiation) to form EBs and cultured for 6 days. EBs are then transferred to low adhesion 24-well plates in neural induction media, during which they began forming translucent neuroepithelial tissues, and these were cultured for 5 more days (neural induction). On Day 11 of the protocol, tissues are transferred to droplets of Matrigel which were allowed to gel at 37C and were subsequently grown in cerebral differentiation media for 4 days, during which they began forming expanded neuroepithelial cavities. Finally, the tissue droplets are transferred to a spinning bioreactor containing cerebral differentiation media as above except B27 supplement with vitamin A. B) Engineered cerebral organoids reproducibly generate elongated neuroepithelium using PLGA microfilaments. Schematic of the method, timeline and media used for generating engineered cerebral organoids (enCORs) are shown at the top. Bioengineered EBs from H9 cells at day 11, during neural induction, showing clearing along the edges and polarized neural ectoderm (arrows) are shown bottom left. Immunohistochemical staining of day 10 bioengineered H9 EBs for the germ layer markers Brachyury for mesoderm, N-Cadherin for neural ectoderm, Sox17 for endoderm, and E-Cadherin for non-neural epithelium are shown bottom right. Note the prevalence of polarized neural epithelia (arrows) displaying the apical domain on the surface (white asterix) with only occasional other germ layer identities (arrowhead). C) Singular neural rosette emergence within forebrain and spinal neuroepithelial tissues. Representative images of neural rosette emergence in micropatterned, hESC-derived forebrain neuroepithelial tissues of various areas with and without ROCK inhibitor, and quantification of polarization foci/rosettes per forebrain tissue with the number of tissues analyzed per condition above each bar, showing a micropatterned-size dependence on single neural rosette emergence. A) was adapted and modified from Lancaster et al. 2013, B) was adapted and modified from Lancaster et al. 2017, C) was adapted and modified from Knight et al. 2018.

Current cerebral organoid protocols can generate unprecedented microscale organization, in which ventricular zone (VZ)-like organizing centers of differentiation are formed that resemble the developing neural tube. However, due to the lack of control over the macroscale structure of the organoids, multiple organizing centers of differentiation are typically formed, leading to inconsistency and lack of reproducibility. As reviewed by Huch, Knoblich, Lutolf, and Martinez-Arias [125], reproducibility, which they define as consistency in phenotypic traits including organoid size, shape, cellular composition and 3D architecture, is essential in order to (1) understand the mechanisms that underlie organoid development in normal and pathological situation and (2) to use them as targets for manipulation or drug testing. Additionally, they that the reason model organisms studies have been so informative is because of their reproducibility, which enables the systematic detection abnormal deviations[125].

Previously, it has been reported that the variability of typical organoid protocols is first observed during the stages of neural induction. Since most brain organoid protocols initiate from spherical EBs and the neuroepithelium develops on the exterior of the EBs, the Knoblich group hypothesized that the variability may be due to low surface area to volume ratio generated from uncontrolled formation of the spherical aggregates. To test this hypothesis, they showed that by decreasing the size of the aggregates to increase the surface area to volume ratio, they were able to demonstrate that the smaller EBs showed more relative neuroectoderm formation, decreases in the amount of cells with non-neuroectodermal identity, such as mesoderm and endoderm, and less non-neural tissues upon Matrigel embedding. Additionally, to increase the size of the organoids while keeping a large surface area to volume ratio, they developed PLGA microfilaments to serve as a floating scaffold to generate what they termed microfilament

engineered organoids (enCORs). They showed that the enCORs displayed elongated EB morphologies while maintaining dense cell composition, exhibiting clearing along the edges, forming polarized neural ectoderm that was elongated, and improving the efficiency of neuroectoderm formation (**Fig. 1B**). This study demonstrates the potential of introducing engineering techniques to improve the reproducibility and efficiency of deterministic cerebral organoid formation. However, this approach still provides minimal morphological control over the initial size and shape of the EBs, which results in organoids with varying amounts of ventricular zone-like centers of differentiation, as compared to the single ventricular zone formed in vivo[26].

Previous Ashton lab publications have demonstrated that control over the initial microscale morphology of organotypic tissues in 2D culture is critical to generate single rosette tissues, which are 2D analogs of the neural tube's neuroepithelium that develops into the ventricular zone. Using 2D microcontact printed platforms in which the size of patterned tissues was systematically controlled, it was demonstrated that single neural rosette emergence can be obtained with >80% reproducibility [126] (**Fig. 1C**).

Based on such published studies, it is hypothesized that control over the microscale morphogenesis of organoids during the initial stages of derivation is a critical factor in generating reproducible biomimetic neural tube-like organoids. In vivo, the brain and spinal cord develop from the neural tube, which has 3D cylindrical annulus morphology. In contrast, cerebral organoids and engineered enCORs are usually formed from spherical EBs in which the overall size and shape remains unrestricted, which after differentiation results in organoids with varying number of ventricular zone-like regions[26]. In this chapter, we translate the 2D culture

microscale control strategy that generated single rosette neuroepithelial tissues to a 3D platform. Our methodological approach was to inject hPSCs into alginate hydrogel monoliths with a PVOH-Ca-molded central microscale channel (see *Chapter 2*). This was hypothesized to produce cylindrical aggregates of the channel's shape and diameter, which was mimetic of the developing neural tube. In the literature, it has been shown that platforms which utilize hydrogels with internal architectures are useful in vascularization tissue engineering strategies that typically rely on forming an endothelial cell lining [69]. These protocols utilize low concentration cell slurries to generate hollow channels lined with cells. However, hPSC injection strategies to form high cell density tissues within hydrogels with internal architecture, which is required for successful organoid formation, are limited [84]. Thus, we developed such an injection strategy optimized to formation of hPSC cylindrical aggregates within PVOH-Ca-molded alginate hydrogel channels.

We hypothesized that the cell concentration post injection would be a critical factor to achieve contiguous, highly compacted, cylindrical aggregates inside PVOH-Ca casted tubular channels. To test this hypothesis, variables such as the initial cell injection concentration, the method of injection, and physical restriction of the hydrogel channel outlet were investigated to determine optimal conditions for reproducible hPSC cylindrical aggregate formation. Also, the hydrogel fabrication device was redesigned to increase the rate and probability of successful hPSC injections.

2. Materials and Methods

2.1. Materials

Sterile Pronova SLG1000 sodium alginate was purchased from Pronova Biopolymer. Calcium Chloride was purchased from Sigma Aldrich. 316 stainless steel raw material was purchased from McMaster-Carr Supply Company. Monopol C100 Polyvinyl Alcohol was purchased from Monosol Inc. Dental SG Resin to make the 3D printed devices was obtain from FormLabs and devices were printed by the MakerSpace at UW-Madison. Calcium sulfate was purchased from Acros Organics. Glass pipette needles (#Custom Pipette PIP50BV30) and Micromanipulator MPC-385 setup are purchased from Sutter Instruments. PHD UltraTM syringe pump was purchased from Harvard Apparatus. Gel-loading pipette tips (1-200 uL, Cat. No. 37001-150) for cell injections and hydrogel fabrication device assembly were purchased from VWR. ROCK inhibitor (Y27632) was purchased from R&D Systems. NanoFil needle-tip stainless steel needles (35g beveled) were purchased from World Precision Instruments. Four-well Nunc™ Lab-Tek™ II Chamber Slide were purchased from ThermoFisher. Penstrep (15140122) and FL Countess II Instrument Automated cell counter (AMQAF1000) were purchased from Invitrogen.

2.2. PVOH-Ca casted Alginate Hydrogel Fabrication

2.2.1. Fabrication for Micromanipulator Injections

Alginate hydrogels with internal tubular channels were cast in a 4 well chamber slide. One milli-liter of Sterile 2% (w/v) Sodium alginate mixed with a 40µL of a 5% (w/v) $CaSO_4$ slurry was pipetted into each well of the chamber slide. Injection molded Polyvinyl Alcohol-Calcium Acetate templates (PVOH-Ca) cylindrical templates were immediately placed inside the alginate solution to serve as a sacrificial material and the alginate solution was pre-gelled for 5 minutes. The

chamber slide was submerged in a room-temperature bath of 2% (w/v) $CaCl_2$ in deionized water overnight to induce bulk hydrogel gelation and completely dissolve the PVOH-Ca template. All hydrogel fabrication is performed inside a sterile cell culture hood. Tweezers to handle the PVOH-Ca templates were sterilized with 70% Ethanol and UV for 1hr. PVOH-Ca templates were sterilized under UV for 1hr. $CaCl_2$ was sterilized by filtration or autoclave. $CaSO_4$ slurry was sterilized by autoclave. Hydrogels were kept up to 1 day in E6 or E8 media + Penstrep until ready for injections.

2.2.2. Fabrication in 316 Stainless Steel Devices

The fabrication devices were comprised of a stainless steel base with a well to add precursor alginate and crosslinking calcium chloride solutions, an acrylic bottom lid, an o-ring to create a tight seal between the acrylic lid and the stainless steel, flathead screws to secure the lid in place, and stainless steel inlet and outlet needles to hold the PVOH-Ca templates (**Appendix Fig. 1**). To form alginate hydrogels, 1.5 mL solution of 2% sodium alginate, dissolved in sterile deionized water and prepared by overnight mixing at 4ºC, was combined with 60 µL of 5% $CaSO_4$ in deionized water create a slurry. Then, the slurry was pipetted into the assembled device to encapsulate the suspended PVOH-Ca template, and allowed to pre-gel for 5 - 10 min. The device was submerged in a room-temperature bath of 2% (w/v) $CaCl_2$, in deionized water, overnight to induce bulk hydrogel gelation and completely dissolve the PVOH-Ca template. Stainless steel devices and components were autoclaved, and the devices were assembled in a sterile cell culture hood. The PVOH templates were sterilized in a cell culture hood with UV for 1hr prior to assembly into stainless steel device.

2.2.3. Fabrication in 3D-Printed Dental Resin Devices

Alginate hydrogels were fabricated within 3D printed Dental Resin molds made at the UW-Madison Makerspace lab (**Appendix Fig.3)**. To form alginate hydrogels, PVOH-Ca cylindrical templates are inserted between inlet and outlet gel loading tips analogous to the stainless-steel needles in the 316 stainless steel devices. Seven-hundred and fifty microliters of 2% sodium alginate solution, in sterile deionized water, was combined with 40 µL of 5% $CaSO_4$, in deionized water, to create a slurry. Then, the slurry was vortexed and pipetted into the device to encapsulate the suspended PVOH template, and allowed to pre-gel for 5 - 10 min. The device was submerged in a room-temperature bath of 2% (w/v) $CaCl_2$, in deionized water, overnight to induce bulk hydrogel gelation and completely dissolve the PVOH template. 3D printed Dental Resin devices and gel loading tips were autoclaved, and the devices were assembled in a sterile cell culture hood.

2.3. H9 human Embryonic Stem Cell Culture

WA09 (H9, WiCell) human embryonic stem cells (Passage 28-40) were maintained in the pluripotent state in E8 medium (Thermofisher) on Matrigel^{TM} (WiCell) coated plates. The H9 line was authenticated as karyotypically normal by the provider, and within 3 months of these experiments, tested for mycoplasma with negative results (WiCell). After banking, the cells were used for no more than 15 passages during experimentation. To prepare stem cells for injection into alginate hydrogels, the cells were washed twice with 2ml of PBS and passaged using 1ml of accutase per well of a 6-well plate. After incubation at 37°C for 5 minutes, the cells were collected and added to a 15 ml conical with fresh media to centrifuge at 1000 RPM for 5 min. Cells were resuspend in 1ml of media and counted in trypan blue solution to assess cell viability using an

automatic cell counter. Cell slurry concentrations of 10-500,000 cells per microliter were used for injections. After counting, cells were centrifuged again and resuspend in the appropriate amount of media containing Penstrep and Rock Inhibitor (10μM). The cell solution was kept on ice and protected from light while preparing and performing injections.

2.4. Neuroepithelial Cell Derivation

Neural induction of well plate controls was executed as previously described [123]. Briefly, hESCs were passaged with Accutase (Life Technologies) onto Matrigel-coated plates at a density of $1x10^5$ cells/cm^2 with 10 μM ROCK inhibitor (Y27632; R&D Systems). The following day, cells were changed to E6 medium (ThermoFisher) for 5 days with daily complete media changes. On the 5^{th} day, cultures were fix with 4% PFA and stained for rosette polarization marker N-Cadherin and neuroepithelial cell marker Pax6 to validate the cells' usage for injections.

2.5. Cell Injections into Molded Alginate Hydrogels

2.5.1. Micromanipulator

A set of injections were conducted using an MPC-385 Micromanipulator (Sutter Instruments) and a Xenoworks Analog Microinjector (Cat No. V001182) under a Leica DMS1000 Digital Stereo Microscope (W. Nuhsbaum Inc.) connected to a computer monitor for real-time viewing (see Appendix **Fig. 3A**). For each injection, a 3mL syringe was inserted into the Microinjector holder and connected to a glass pipette injection needle through microfluidic tubing. The entire assembly was filled with mineral oil to facilitate the required injection pressure control. The injection needle was mounted on a micromanipulator equipped with two different knobs for injections: a coarse dial knob which allows for greater volumes (1 revolution = 39μL) and the fine

dial knob is ideal for smaller volumes (1 revolution = 3.9µL). H9 hESCs were collected using the fine dial knob on the micromanipulator from a 1.5mL Eppendorf microcentrifuge. The needle was placed on top of the surface of the alginate hydrogels under the microscope, then lowered in the z-direction to puncture through the hydrogel towards the PVOH-Ca casted channel. Cells were injected by slowly rotating the fine and coarse injector knobs. After injection, hydrogels were cultured in E8 media with Penstrep in a cell culture incubator and aggregate formation was assessed the next day via brightfield microscopy.

2.5.2. Syringe Pump

Prior to injection, alginate hydrogels fabricated within custom stainless-steel devices were removed from the devices and placed on 6 well plates with E8 media to prepare for injection. A PHD UltraTM syringe pump (Harvard Apparatus) was loaded with a 3cc syringe connected via tubing to a 1-200 µL gel-loading pipette tip (VWR, Cat. No. 37001-150). Cells were collected using the automated withdraw setting and injected into the alginate hydrogel's molded channel at rates between 1-100 nL/s in a sterile cell culture hood. The injection process was visualized using an EVOSTM XL Core Imaging System (ThermoFisher). Stem cell-injected hydrogels were cultured in E8 media with Penstrep in a cell culture incubator and aggregate formation was assessed the next day via brightfield microscopy. Tweezers to handle the hydrogels, microfluidic tubing, luer lock needles, and gel loading tips were autoclaved prior to hydrogel fabrication.

2.6. Determination of optimal injection cell slurry concentration

To determine the optimal cell suspension density, 6 different stem cell injection suspension concentrations were tested: 10k, 25k, 50k, 100k, 250k, and 500k cells/uL. H9 hESCs were washed twice with 2ml of PBS and passaged using 1ml of accutase per well of a 6-well plate. After

incubation at 37°C for 5 minutes, the cells were collected and added to a 15 ml conical with fresh media to centrifuge at 1000 RPM for 5 min. Cells were resuspend in 1ml of media and counted in trypan blue solution to assess cell viability using an automatic cell counter. After counting, cells were centrifuged again and resuspend in the appropriate amount of media containing Penstrep and Rock Inhibitor to make a cell stock solution of 500k cells/uL, from which the other densities were made by serial dilution. Cells from each condition were collected using a syringe pump and a gel loading tip to simulate the injection process. Then, the cells were injected back into new Eppendorf tubes resuspended all at the same concentration (150k cells/cm2) to seed confluently on 6 well plates. The following day, cells were imaged to assess the confluency as an indicator of viability and changed to E6 medium (ThermoFisher). Cells were cultured for 5 day with daily complete media changes. On the 5^{th} day, cells were fixed with 4% PFA and stained for polarization marker N-Cadherin and neural progenitor marker Pax6 to assess neural induction and rosette formation.

2.7. Mechanical testing on EDTA-bound Alginate Hydrogels

EDTA-bound Alginate gels were prepared in ASTM D638 standard Type 1-Specimen dog bone shape molds for tensile testing. The molds were filled with 300uL of a 2% (w/v) Alginate Solution. 500 µL of 2% (w/v) $CaCl_2$ were added to each mold for at least 5 minutes. $CaCl_2$ was replenished every 5 minutes for 3 additional incubation periods. To initiate the hydrogel binding procedure, 2 gels were treated with 170mM EDTA on the clamping region. The EDTA treated area were placed in contact and held down together for 1 min. Water was used instead of EDTA for negative controls. Calcium chloride was then added to the gels for 1 hour to allow re-binding to occur. The

bounded gels were taken to an Instron Microtester (model 5548, Crone lab) for tensile testing. Intact alginate hydrogel specimens were used as positive controls.

2.8. Post-processing of PVOH-Ca Molded Alginate Hydrogels

To promote cell compaction and formation of channel-long aggregates, alginate hydrogels were modified post-fabrication to restrict cell exit from the hydrogel outlet during the injection process. The hydrogels outlets were sealed by dipping the outlet ports in a 50mM solution of EDTA for 5-10 minutes. Then, the re-liquified end was dipped in fresh 2% (w/v) alginate solution, and subsequently dipped in 2% (w/v) CaCl2 for 10 minutes forming a new closed alginate surface. Sealed hydrogels were stored in E8 media until injection. For bioreactor culture, a secondary hydrogel encapsulation was performed the day after stem cell injections to prevent cells from exiting the inlet port due to differential hydrodynamic pressure gradients. Successful sealing of hydrogels was assessed via brightfield microscopy pre- and post-injection.

3. Results

3.1. Development of a cell injection protocol: micromanipulator vs. syringe pump

Two different strategies for injecting hESCs into alginate hydrogels with PVOH-Ca-casted channels were investigated. The first method utilized a Sutter Instruments micromanipulator injection system, which is commonly used for injections into embryos of different species such as drosophila and chicks (**Appendix Fig. 3A**) [127], [128]. Alginate hydrogels casted with single-filament PVOH-Ca templates were fabricated using a 4 well chamber slide. This produced an enclosed cavity with no inlet or outlet ports (**Fig. 2A(i)**). An enclosed cavity is designed to aggregate the cells in the cavity while allowing the media to displace through the bulk, porous

alginate hydrogel. The injection process was carried out under a standard dissection microscope, by precisely piercing though the alginate hydrogel using a 35g beveled NanoFil™ needle to reach the cavity. hESCs or E6 derived neuroepithelial cells were collected and injected into the cavity using manipulator's fine and coarse dials

Although injection needle placement into the cavity is achievable, several limitations to this method were observed. First, precisely determining the needle location after the hydrogel has been pierced is non-trivial. The small dimensions of the channels (400-600um in diameter) present a challenge for reproducible and efficient targeting and injection of cells into the hydrogel cavity. This led to inadvertent injections into the bulk of the hydrogel, which resulted in rupture of the hydrogel during the injection as cells are too large to navigate through the pores Additionally, injections in which the channel was successfully reached were hampered by backpressure resulting from a combination of factors. First, the hole created from puncturing the hydrogel to inject cells into the channel inadvertently created a path of least resistance for injected cell backflow. Second, lack of precise control over injection flow rates limited the ability to reproducibly force media inside the channels to diffuse through the hydrogel pores. This caused the media to act as a barrier for cell entry into the channel (**Fig.2A (ii)**). These limitations led a failure to inject cells into 44% of the fabricated hydrogels.

Of the remaining 56% of hydrogels that were successfully injected, only 31% resulted in aggregate formation, none of which resulted in a contiguous cylindrical cell aggregate. Hydrogels that did not result in aggregate formation exhibited cell removal from the channel into the surrounding media after a day of culture. Those that did form aggregates were typically small and spherical and rarely proliferated to conform to the geometry of the channel cavity (**Fig. 2A and 2B**).

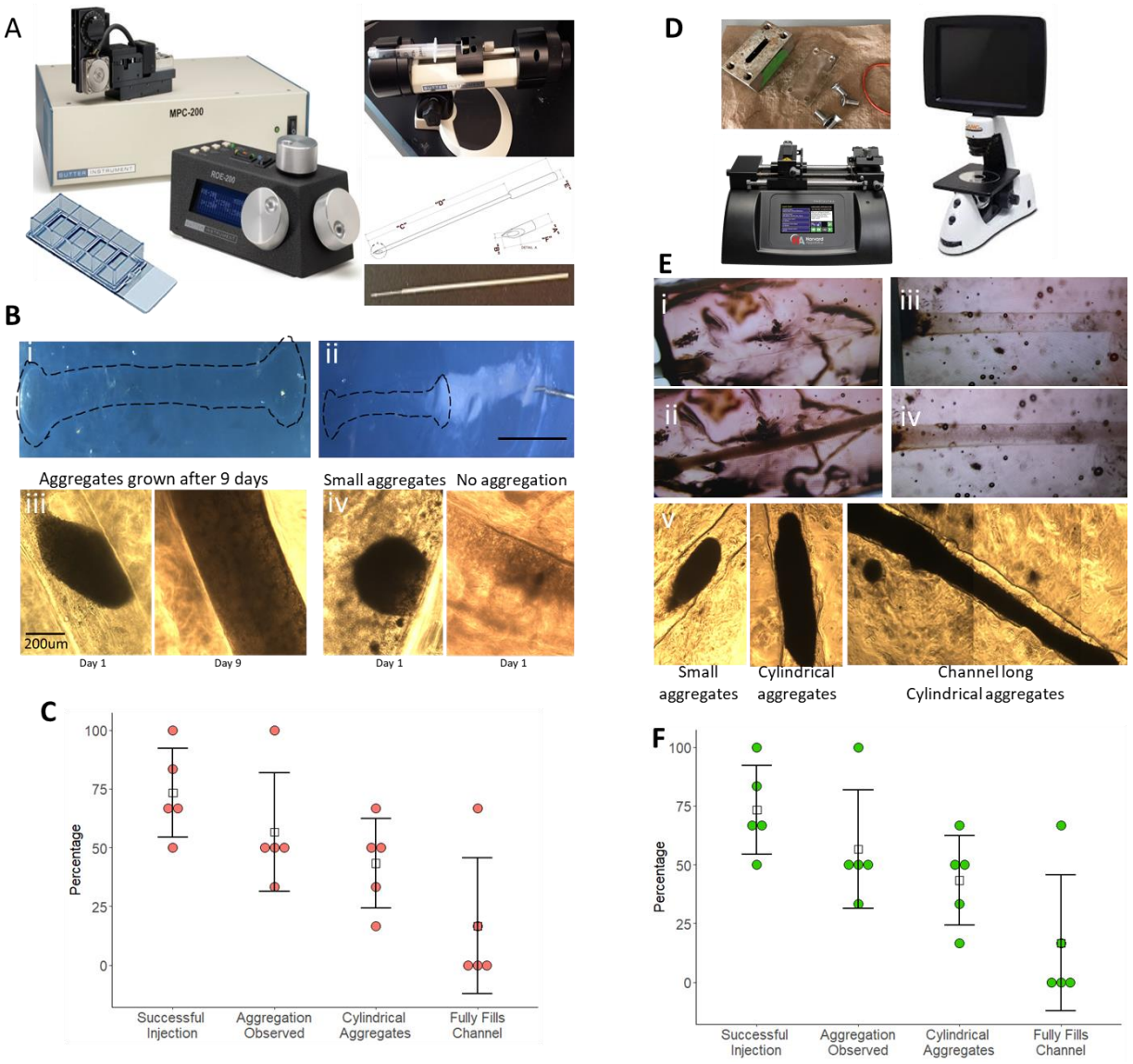

Figure 2: Cell injection strategies. A) Alginate hydrogels display tubular cavity (i) post-sacrificial molding. (ii) Injection difficulty is evidenced by failure of cells (opaque) to enter the channel post injection. Brightfield images 1-day post injection showed (iii) rare successful injections with growth after 9 days as well as (iv) the more representative small or no aggregations on Day 1. B) Quantification of each stage of tubular aggregate formation. C) Proof of principle stem cell injection into alginate hydrogel using the syringe pump system (i) pre-injection and (ii) post injection, demonstrating enhanced cylindrical aggregate formation compared to micromanipulator setup. (v) Brightfield images illustrating the differences in the type of aggregation formed post injection. D) Quantification of the different types of aggregates formed post injection as illustrated in (C).

To overcome these limitations, an alternate injection process was pursued using an automated syringe pump and an adaptation to the stainless steel 316 (SS316) device used in Chapter 2 for hydrogel molding (**Appendix Fig. 3B**). The syringe pump allowed us to have much more control over the flow rate and target volume of the injection process. Additionally, the SS316 device used

to fabricate the alginate hydrogels contained stainless steel needles that formed inlet and outlet ports in parallel orientation to the cavity. The needles were used to hold the PVOH-Ca sacrificial material in suspension to mold the channel within the alginate hydrogels. We hypothesized that a channel cavity with inlet and outlet openings would decrease the amount of backpressure buildup during the injection process.

The efficiency of cell aggregate formation using the syringe pump setup was increased compared to the micromanipulator injected hydrogels due to several process improvements (**Fig. 2D**). Most notably, the optimal injection range of 1-100 nL/s in this setup is significantly lower than the capable range of the micromanipulator (3.9-39uL/revolution). This lower flow rate allows cells to remain as a cohesive aggregate throughout the process of injection. Backpressure is significantly reduced due to improved injection parameters and the open channel outlet. This led to an increase in the number of hydrogels that resulted in successful cylindrical cell aggregate formation **(Fig. 2C (i and ii) and 1D**).

The percentage of cylindrical aggregate formation 24 hours after hESC injection into alginate hydrogel cavities was improved from 0% using the micromanipulator setup to 43% using syringe pump method (**Fig. 2D**). Several improvements in this process allowed for the increase in cylindrical aggregate formation as compared to the micromanipulator injection setup. First, the addition of inlet and outlet ports increased ability to place the needle in the channel for injection, which directly impacted the ability to successfully inject cells into the channels. Second the automation of the flow rate, particularly the ability to dramatically decrease the flowrate from roughly 3.9uL/s to 1-100nL/s, promoted an increase in injections that proceeded with high cell concentration, thereby allowing increased cell aggregation post-injection (**Fig. 2C and D)**.

However, injections with open outlet port led to inconsistent cell packing in the channels, which in turn negatively impacted the reproducibility of contiguous cylindrical aggregate formation. Quantification showed that only 17% of injections resulted in a cylindrical organoid that spanned the entire length of the channel (**Fig. 2D**). Sections 3.2 and 3.3 will describe additional optimization strategies to increase the percentage of channel-long cylindrical organoids.

3.2. Optimization of cell suspension concentration

In traditional derivation protocols, organoids form from densely packed hESCs spheroids created using gravitational and centrifugal aggregation [16], [23]. In contrast, most cell injection protocols into hydrogel channels and/or microfluidic devices are designed to form microvessels in which cells line the channel via adhesion to integrin binding peptides such as -RGD. These protocols require comparatively lower cell slurry concentrations and cell density upon initial seeding. When these cell injection strategies have been adapted generate aggregates within microscale channels, they form discontinuous spheres instead of continuous cylindrical aggregates [69], [84]. We hypothesized that injection of a high concentration cell slurry was required for successful formation of a contiguous cylindrical aggregate within sacrificially molded alginate hydrogel channels. Thus, we investigated which H9 hESC cell slurry concentrations could be injected through a gel-loading micropipette tip without decreasing cell viability due to shear (**Fig. 3A**). Cell suspensions of 100,000, 250,000, and 500,000 cells/μL were prepared, collected, and injected by syringe pump through a gel-loading micropipette tip into empty 1mL Eppendorf tubes. Then, the cells were re-seeded onto Matrigel-coated 6-well plates at a 150,000 cells/cm^2 density and cultured for 24hr to assess cell viability. Qualitative observation of the cell confluency 24 hours post-seeding indicated that cell slurries up to 250,000 cells/ μL remained viable at levels

comparable to the standard cell subculture control (**Fig. 3B**). Also, immunochemical analysis showed that the cells maintained the ability to polarize and differentiate into neural progenitors (**Fig. 3C**). Based on this result, the 250,000 cells/ μL cell slurry concentration was used for all future injections.

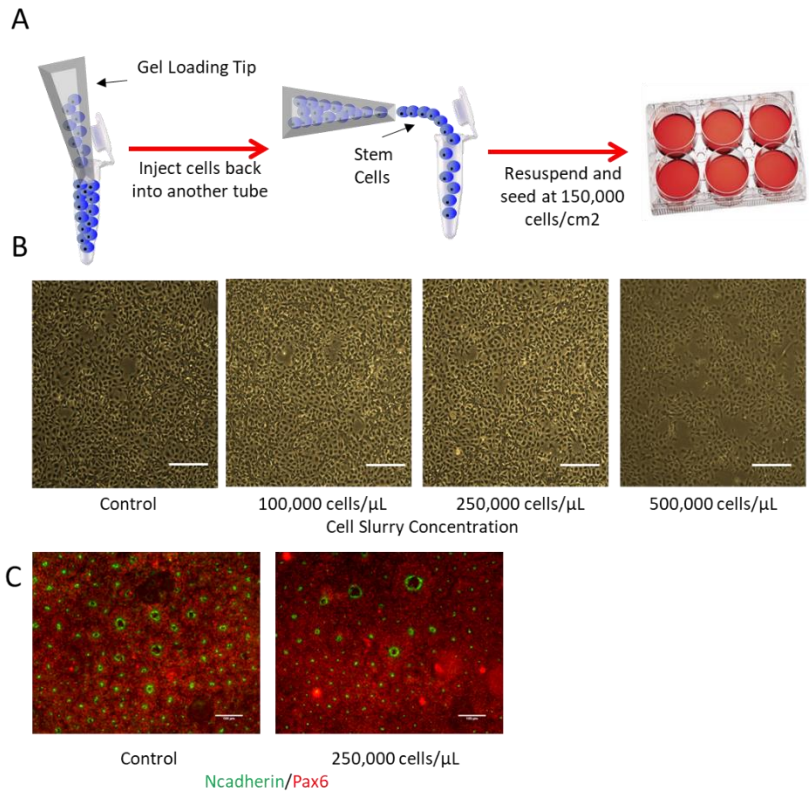

Figure 3: Determination of optimal injection cell slurry concentration. (A) Schematic of procedure used to test whether shear stress due to injection of cell slurries with various concentrations affected H9 hES cell viability. (B) Brightfield images of culture wells 24 hours after re-seeding 'injected' H9 cells slurries at 150,000 cells/cm2. (C) Immunochemistry of the control and 250K/uL cells showing N-Cadherin polarization and neural progenitor marker Pax6. Scale bars in (B) 200 and (C) 100 um.

3.3. Modification of alginate hydrogels to reproducibility achieve high cell density packing upon injection

It was hypothesized that to maximize formation of contiguous, channel-long cylindrical cell aggregates, it is necessary maintain the high-density cell packing post-injection. To test this hypothesis, cells were restricted from exiting from the hydrogel outlet during the injection

process, by sealing the hydrogels at the outlet with an extra layer of alginate. It was reasoned that EDTA, a divalent cation chelating agent, could be used to sequester calcium ions from the outlet of the hydrogel channel. This would re-liquify the surface of the hydrogel outlet, which would compromise the channel integrity in that region. Then, sealing could be finalized by adding a secondary layer of alginate solution and re-crosslinking with calcium chloride. First, this approach was validated by performing mechanical testing on ASTM D638 standard Type 1-Specimen dog bone shape alginate hydrogels using an Instron Microtester [129] (**Fig. 4A**). Dog bone samples were bound together at the clamping regions using the ETDA chelation-alginate resealing method and compared that to an intact alginate hydrogel, which served as positive controls, and alginate hydrogels bound by superficial tension via a droplet of water to serve as a negative control. It was expected that if the sealing between hydrogels is successful, the mechanical properties of the sealed sample should approximate the mechanical properties of the intact, positive control hydrogels. As expected, the maximum load before collapse for the EDTA/re-sealed alginate hydrogels (0.26N) approximated the maximum load before collapse of the intact alginate sample (0.33N). Whereas, the surface tension-bound sample had a negligible maximum load before collapse of 0.02N, due to the hydrogels slipping apart rather than breaking apart at one the neck regions (**Fig. 4A(iv)**).

Based on the previous results, this approach was applied to the PVOH-Ca casted alginate hydrogels to seal the channel outlets. PVOH-Ca casted alginate hydrogels were dipped in 50mM EDTA, then in 2% (w/v) alginate solution and immediately into a 2% calcium chloride solution to allow for re-crosslinking and sealing (**Fig. 4B**). The efficacy of the sealing process was initially assessed via brightfield imaging as determined by formation of the secondary gel sealing layer. It

was found that a secondary gel layer was formed at the outlet port, indicative of successful sealing (**Fig. 4D(i)**). Injection of hESCs into the newly sealed hydrogel further confirmed successful sealing at the outlet as evidenced by high cell packing after 1 day of culture (**Fig. 4D(iv)**). Quantification of aggregates formation showed that the sealing process significantly increased the number of hydrogels that resulted in successful injections and the number of hydrogels that had channel long-cylindrical aggregates (**Fig. 4E**). Finally, to extend the protocol to long term bioreactor culture, injected alginate hydrogels were encapsulated in an additional layer of alginate to seal the inlet by dipping into an alginate solution after 1 day of culture, followed by immersion into $CaCl_2$ solution to crosslink the additional alginate (**Fig. 4C**). This secondary sealing is necessary for bioreactor culture, as cells within hydrogels not sealed at the inlet could be removed from the hydrogel due to differential pressure caused by the bioreactor's convective flow (**Fig. 4D(iv)**). The fully encapsulated hydrogel can be cultured long-term in a spinner flask for organoid derivation, which will be further discussed in the following chapter. Moving forward, this hydrogel sealing approach was used in combination with the syringe pump injections to form channel-long cylindrical stem cells aggregates, which are hypothesize to be biomimetic replacements for spheroidal EB formation in cerebral organoid protocols [16].

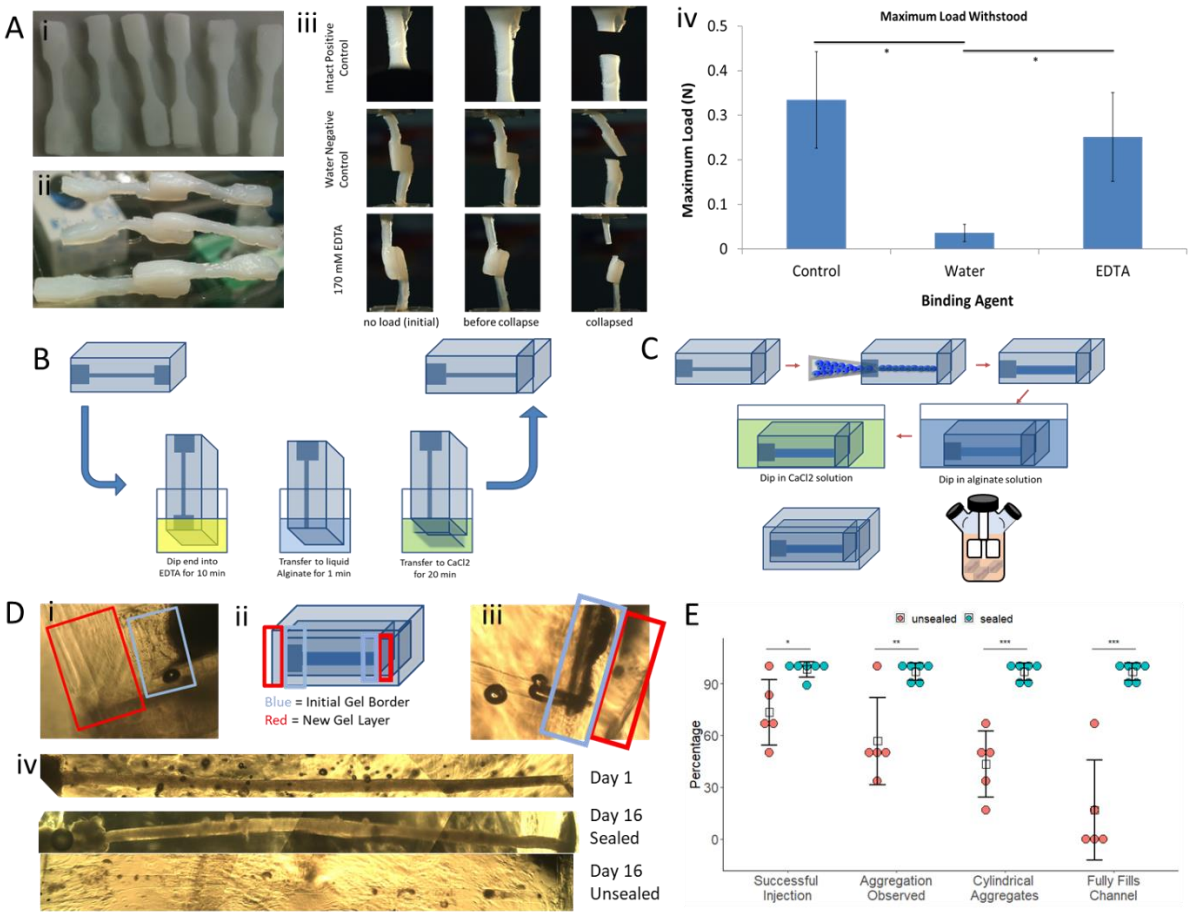

Figure 4: Hydrogel outlet post modification to restrict cell ejection from hydrogel channel during injection. A) (i) ASTM D638 standard Type 1-Specimen dog bone shape alginate hydrogels (ii) sealed together using ETDA chelation. (iii)Mechanical testing using Instron Microtester showing alginate hydrogels effectively re-liquified and bound as evidenced by the neck break of bound hydrogels and (iv) maximum load before break. B) Diagram of alginate hydrogel channel outlet sealing using EDTA mediated calcium chelation, alginate solution re-application over the channel outlet, and $CaCl_2$ re-crosslinking. C) After cell injection, the hydrogel monolith's inlet was sealed by immersion in an alginate followed by $CaCl_2$ solution to crosslink the second layer of alginate. The fully encapsulated hydrogel can be cultured in a spinner flask for organoid derivation. D) Hydrogel sealing at both stages was shown to be effective by brightfield imaging (i-iii) and secondary sealing is shown to be necessary for bioreactor culture (iv). E) Quantification of tubular aggregate formation using syringe pump injection into sealed and unsealed hydrogels showing a significant improvement in the reproducibility of generating cylindrical EB-like aggregates.

3.4. Design of Stainless Steel 316 (SS316) and 3D Printed Dental Resin (3D-PDR) Devices

Initially, the devices to fabricate alginate hydrogels with internal architectures were design to consist of a stainless steel base, which contains a well to add precursor Alginate and crosslinking calcium chloride solutions, an acrylic bottom lid to allow imaging through the bottom of the device, an O-ring to create a tight seal between the acrylic lid and the stainless steel base,

flathead screws to secure the lid in place, and stainless steel needles to hold the tube molding PVOH-Ca template (**Fig. 5A**). Using this device, alginate hydrogels with various internal architectures were fabricated using PVOH-Ca templates (*see Chapter 2*) and used as the platform to generate channel-long cylindrical aggregates. However, there are several limitations due to device design that cause the hydrogel fabrication process to be low throughput. First, large number of parts required to assemble the device makes the process non-trivial (**Fig. 5A(i)**). Second, the acrylic lid cannot withstand UV or ethanol sterilization procedures and easily cracks after a certain number of experiments. Third, as mentioned above in the previous section, the current device design does not allow for cell injections in situ, due to post injection cell disturbance caused by back pressure upon removal of the needle from the inlet port of the device (**Fig. 5B**). Thus, hydrogels must be removed from the device prior to injection, which complicates the injection procedure (**Fig. 5A(ii)**).

To increase injection throughput, a 3D printed, biocompatible hydrogel molding device was fabricated at the UW-Madison Makerspace. This device was designed to have similar basic features as the previous SS316 device. It includes a well for the addition of alginate and calcium chloride solutions, and inlet/outlet ports to hold the PVOH-Ca templates and needles for the injection of hESCs into the hydrogel channel (**Fig. 5C**). Additionally, it includes a series of upgrades. First, the device is composed of 2 easily assembled parts (**Appendix Fig. 3**). The top piece contains the alginate and calcium chloride loading well and the entry ports to hold the PVOH templates and needles for the injection of hESCs. The bottom piece contains the base for the hydrogel, and 2 long inserts that go into the top piece to prevent leaking (**Fig. 5C** and **Appendix Fig. 3**). This setup significantly reduces the amount of parts and time required for

assembly. Additionally, this design removes the need for acrylic bottom lids because the device is made by a single dental resin material that is biocompatible, autoclavable, and designed with an easily removable bottom piece to allow imaging during injections. Finally, back pressure was eliminated by reducing the length of the device inlet port. These upgrades increased the throughput of the injection process per experiment by allowing a maximum of 16 injection per single experiment compared to a maximum of 6 with the SS316 device (**Fig. 5D**).

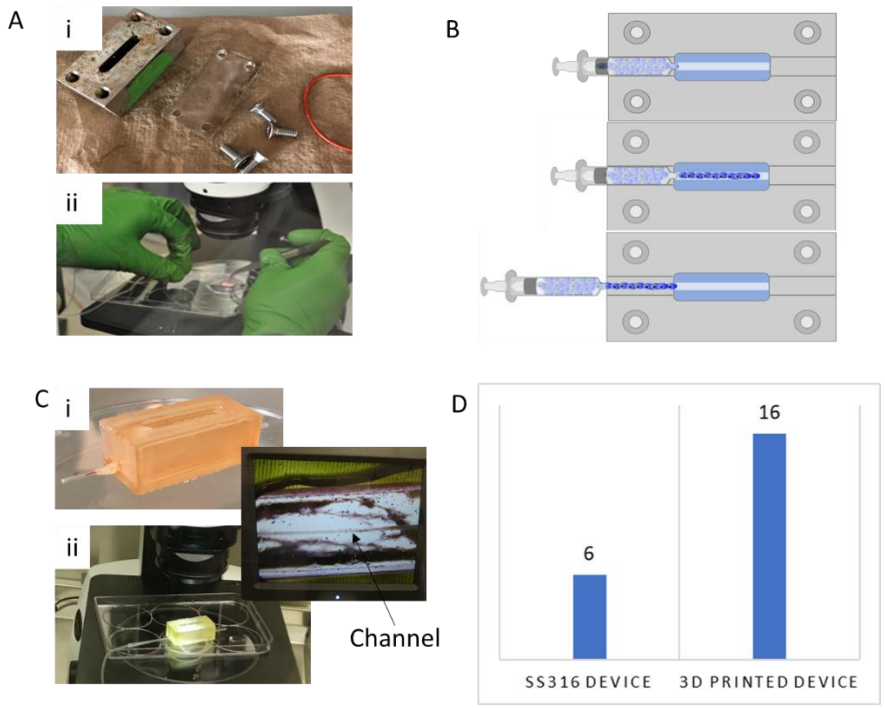

Figure 5: Development of higher throughput 3D printed Dental Resin device for formation of continuous engineered stem cell tubular aggregates using alginate hydrogels with internal architecture. A) (i) Initial device was comprised of a stainless-steel top, an acrylic bottom, an O-ring, stainless steel screws, and stainless-steel needles. (ii) This require the hydrogel to be removed from the device and be injected by hand, which limits the throughput and reproducibility of successful injections. B) One of the limiting factors of the current device design is the inability to perform injection in situ, due to post injection cell disturbance caused by back pressure upon removal of the needle from the inlet port of the device. C) 3D printed biocompatible dental resin device comprised of 2 easily assembled parts was designed to allow in situ injections to improve throughput. D) Quantification of the maximum number of injections per injection session (3-5 hours) for the Stainless Steel 316 (SS316) device and the 3D printed Dental Resin device.

4. Discussion

The ability to reproducibly generate cylindrical aggregates a critical step towards the final goal of standardizing the formation of neuroepithelial organoids. In established organoid formation protocols, EB stem cell aggregates are formed by gravity and centrifugal forces applied to hESCs that are cultured 96 well plates or aggrewell plates to yield high density spheroids [16], [23]. This approach has led to the formation of cerebral organoids can generate unprecedented microscale organization in which ventricular zone (VZ)-like organizing centers of differentiation are formed that resemble the developing neural tube. However, due to the lack of control over the macroscale structure of the organoids, multiple organizing centers of differentiation are typically formed, leading to inconsistency and lack of reproducibility. Attempts to influence EB formation by increasing their surface to volume ratio showed small improvements the reproducibility and efficiency of cerebral organoid formation [26]. However, this approach still provided minimal morphological control over the initial size and shape of the EBs, which resulted in organoids with varying amounts of ventricular zone-like centers of differentiation, as compared to the single ventricular zone formed in the in vivo neural tube. Therefore, an alternative approach was needed to form high surface to volume EB-like aggregates.

In the Ashton lab, it has been shown that single polarized neural rosettes can be reproducibly formed by controlling the size of neural tube slice cultures using microcontact printed gold slides [126]. It was reasoned that this approach could be extended to high surface to volume ratio EB-like aggregates to increase the reproducibility of biomimetic 3D cerebral organoid formation. In this chapter the injection of hESCs into PVOH-Ca casted alginate hydrogel channels was explored as the method for controlling the morphology of cylindrical aggregates. In the literature, it has

been shown that platforms which utilize injection into hydrogels with internal architectures are useful in vascularization tissue engineering strategies [69]. These protocols utilize low cell densities and will yield hollow channels lined with cells. However, injection strategies that yield dense, compact cell aggregates within hydrogels with internal architecture are required for successful organoid formation. Prior examples are limited and typically lead to formation of discontinuous spheroids within the channels instead of long cylindrical aggregates [84]. Thus, it was necessary to design an injection strategy optimized for the formation of cylindrical aggregates within PVOH-Ca-molded alginate hydrogel channels. The injection method, cell suspension concentration, post-hydrogel molding modifications, and injection device design were found to be important factors to standardize cylindrical aggregate formation. First, it was demonstrated that PHD Ultra^{TM} Syringe Pump was more optimal compared to the Sutter Instruments' Micromanipulator setup for providing enhanced control of the injection flowrate. The flow rates used ranged between 1-100 nL/s in the syringe pump injection setup, which was significantly lower than the capable range of the micromanipulator (3.9-39uL/revolution). This enhanced the ability to inject the stem cells as a high-concentration cell suspension and promoted continuous cylindrical aggregate formation.

The reproductivity of cylindrical aggregate formation was further enhanced by determining the optimal cell concentration of injection and developing a method to seal the outlet in the fabricated hydrogels. First, it was found that the optimal cell concentration for injection was 250k cells/μL, as it was the highest concentration that demonstrated no adverse effects on cell viability or rosette formation capacity. Second, it was hypothesized that by sealing the outlet, we could restrict cell exit during injection and promote cell packing in combination with the optimized

high-concentration injection solution. To seal the hydrogel outlet, it was demonstrated that EDTA could be used to liquify the outlet port to allow re-sealing using a secondary layer of alginate solution polymerized by calcium chloride. Quantification of channel-long cylindrical aggregates showed that using these optimization parameters in combination with syringe pump injection, the reproducible formation of cylindrical aggregates was achieved, as described in Patent Application US20200115677A1 [94]. In the following chapters, the morphological and biological cues to differentiate cylindrical hESC aggregates into neuroepithelial organoids will be explored.

Chapter 4: Formation of neuroepithelial tube organoids resembling the developing neural tube.

1. Introduction

The neural tube is an early developmental structure that gives rise to the Central Nervous System (CNS), comprised of the brain, retina, and spinal cord. During the initial stages of differentiation, the neural tube will give rise to a transient embryonic structure called the Ventricular zone (VZ) which is composed of radial glia (RG), the embryonic neural stem cells (NSCs) that give rise to all the cellular diversity in the CNS. Differentiation and proliferation of NSCs in the VZ produces the multiple neuronal layers formed during corticogenesis such as the subventricular zone (SVZ), the intermediate zone (IZ), and the six layers of the cortical plate (CP)(**Fig. 1A**) [130], [131].

The current gold standard to model the human neural tube in vitro are stem cell derived organoids. As discussed in detail in Chapter 3, current organoid protocols are limited by variability observed during the first stages of neural induction. Briefly, the Knoblich group showed that increasing the surface area to volume ratio of the EBs during the germ layer differentiation stage increased their relative neuroectoderm formation, decreased the amount of cells with non-neuroectodermal identity, and displayed less non-neural tissues upon Matrigel embedding [26]. However, the minimal morphological control over the initial size and shape of the EBs ultimately resulted in organoids with varying amounts of ventricular zone-like centers of differentiation, as compared to the single ventricular zone formed in vivo. Recent publications have also demonstrated the use of modified V aggrewells to create spheroids of consistent size, which in turn has improved the reproducibility of organoid cell phenotype composition. Yet these

organoids still resulted in varying amounts of ventricular zone-like centers (Fig. 1B) [132]. Another limitation with current organoid protocols is the presence of chemically undefined reagents, such as FBS, Albumin and Matrigel. These biologically derived reagents are ill characterized and as such present considerable batch-to-batch variability, limited experimental control, and inability to decouple their biochemical and biophysical properties [34], [133]. Additionally, since Matrigel is derived from cancerous murine cells, this limits its potential clinical translational. This lack of reproducibility ultimately limits the use organoids as standardized, scalable models of human development and drug discovery.

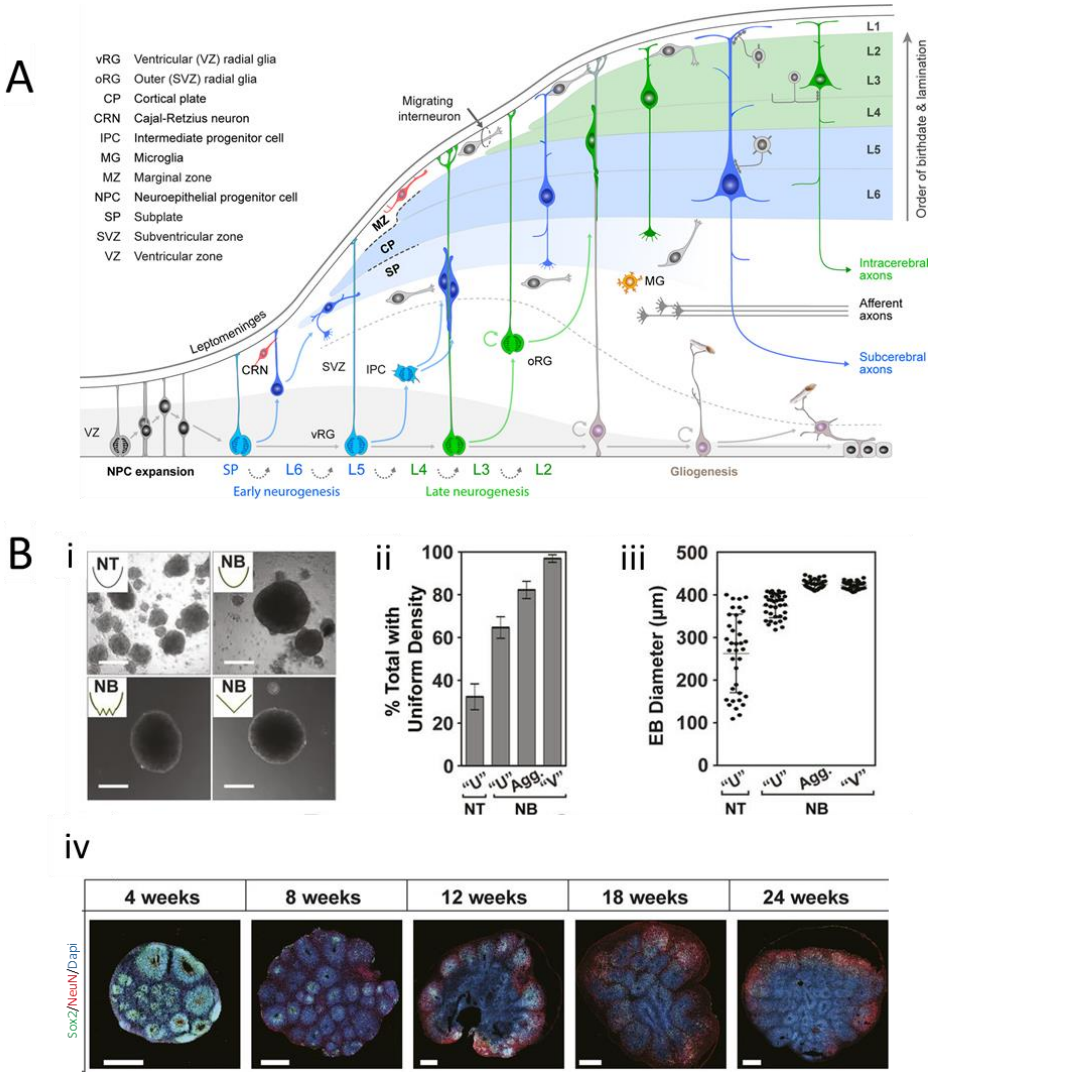

Figure 1: A) Schematic illustration of neurogenesis in the mammalian neocortex. Neuroepithelial cells (NPCs) undergo symmetric cell division to produce an initial pool of cortical progenitors that later transform into ventricular radial glia cells (vRGCs). vRGCs begin asymmetric cell division to generate another vRGC and a nascent projection neuron. The neuron then migrates radially from the ventricular zone (VZ) along the basal process of an RGC into the cortical plate (CP). The earliest born neurons migrate to form the preplate. Later migrating neurons split the preplate into the marginal zone (MZ) and subplate (SP). As neurogenesis proceeds, diverse subtypes of neurons are generated through the successive asymmetric division of RGCs. Early-born nascent projection neurons settle in the deep layers (Layers 5 and 6; red layers), and later-born projection neurons settle in towards mid-neurogenesis stage. Additionally, some populations of RGC daughter cells become intermediate progenitor cells (IPCs) or outer radial glial cells (oRGCs) in the subventricular zone (SVZ). After the neurogenic stages, the radial scaffold detaches from the apical surface and vRGCs become gliogenic, generating astrocytes, or transform into ependymal cells. Tangential migration of interneurons is observed in the MZ, intermediate zone (IZ) and SVZ. Neocortical projection neurons mature into cortical projection neurons (CPNs), which show layer- and subtype-specific morphology and axonal projection patterns. Adapted from Kwan et al. (2012) and Molnar et al. 2019. B) The effect of well shape and surface coating on the reproducibility of embryoid body (EB) formation and ventricular zone formation. (i) Representative bright-field images of EBs generated using the indicated plate format (U shape, aggrewells or V shape). Scale bar = 250 µm. Non-treated (NT), nonbinding (NB). (ii) Percent of cell aggregates displaying uniform density as assessed using phase-contrast microscopy is plotted as the mean ± SD (n = 3). (iii) Individual EB diameters (black circles) and the mean (horizontal dash) ± SD (n ≥ 30/condition) is plotted. (iv) Multiple ventricular zone – like structures are still observed in whole Cortical Organoids (COs). Localization of SOX2 (radial glia) and NeuN (neurons) in hCOs at 4, 8, 12, 18, and 24 wk of age, co-stained with DAPI, was visualized by immunofluorescence microscopy. Scale bar = 500 µm for whole COs. Adapted and modified from Sivitilli et al. 2020.

In Chapter 3, a first step was taken to build and improve upon engineering organoids at the EB stage of derivation. A protocol for reproducible formation of hESC-derived cylindrical aggregates was developed which restricted the aggregates' size and shape to that the developing neural tube. In this chapter, two hypotheses will be investigated: (1) the microscale dimensions of the cylindrical aggregate play an important role in the formation of a single polarized neuroepithelial tube; (2) chemically defined adaption of traditional 3D organoid differentiation protocols can yield the same phenotypical diversity of cerebral organoids. To test these hypotheses, engineered cylindrical aggregates were differentiated into neuroepithelial organoids using established protocols for the formation of neural rosettes in 2D chemically defined culture[123], [126] and neural organoids in 3D [16], [134] using a chemically defined adaption by removing Albumin and FBS from the formulation and using an E6 base media. First, the platforms established in Chapters 2 and 3 were used to generate 3D neuroepithelial tube organoids informed by in vivo neural tube dimensions and polarized expression of N-Cadherin, ECM basement membrane protein Laminin, and early neural progenitor marker Pax6. Different cylindrical aggregates dimensions were investigated by using fishing line to cast channels in alginate hydrogels, which served as an inexpensive and rapid way to generate channel diameters ranging from 180μm to 400μm. Second and as a proof of principle demonstration, our 3D neural organoid chemically defined media was used to generate spheroidal cerebral organoids following published protocols [23]. The formation of discrete brain regions was investigated by staining for polarization/neural progenitors markers N-Cadherin and Pax6, frontal/occipital Lobe marker TSHZ2, early neural progenitors/forebrain markers Sox2 and FoxG1, and hippocampal marker NRP2. Maturation and cytoarchitecture organization of cerebral organoids was investigated at

30 and 60 days, by staining for radial glia/outer radial glia markers Pax6 and phospho-Vimentin, neural and intermediate progenitor markers Map2 and TBR2, Cajal Retzius-CP/Pre plate markers reelin and TBR1, early neuron markers DCX1 and Tuj1, and cortical layer II and IV markers CTIP2 and SATB2 [16]. Lastly, the influence of small molecules (dual SMAD inhibitors) and neural factors (N2 supplement, B27 supplement, Neurobasal media) under defined conditions to contribute to the formation of neuroepithelial tube organoids with single N-Cadherin polarization was investigated.

2. Materials and Methods

2.1. Materials

Sterile Pronova SLG1000 sodium alginate was purchased from Pronova Biopolymer. Calcium Chloride was purchased from Sigma Aldrich. 316 stainless steel raw material was purchased from McMaster-Carr Supply Company. Monopol C100 Polyvinyl Alcohol was purchased from Monosol Inc. Dental SG Resin to make the 3D printed devices was obtained from FormLabs and devices were printed by the UW-Madison MakerSpace. Calcium sulfate was purchased from Acros Organics. PHD Ultra^{TM} syringe pump was purchased from Harvard Apparatus. Gel-loading pipette tips (1-200 uL, Cat. No. 37001-150) for cell injections and hydrogel fabrication device assembly were purchased from VWR. ROCK inhibitor (Y27632) was purchased from R&D Systems. Fishing line was purchased from Amazon (Fishinsir and OneStone US).

2.2. Stem cell culture

WA09 (H9, WiCell) human embryonic stem cells (Passage 28-40) were maintained in the pluripotent state in E8 medium (Thermofisher) on MatrigelTM (WiCell) coated plates. The H9 line was authenticated as karyotypically normal by the provider and tested for mycoplasma with

negative results within 3 months of these experiments (WiCell). After banking, the cells were used for no more than 15 passages during experimentation. To prepare for stem cell injections into alginate hydrogels, H9 hESCs were washed with 2ml of PBS 2 times. Then, one milliliter of accutase was added to each well of a 6 well plate and incubated at 37°C for 5 minutes. Cells were collected, added to a 15 ml conical with fresh media, and centrifuged at 1000 RPM for 5 min. Cells were resuspend in 1ml of media and counted in trypan blue solution to assess cell viability using an automatic cell counter. Cell suspension concentrations used for injections were 250,000 cells/mL, as determined in Chapter 3 to be the optimal cell injection diameter. Cells were centrifuged again and resuspend in the appropriate amount of media containing 1:200 Penstrep and 10μM Rock Inhibitor. The cell solution was kept on ice and protected from light while preparing and performing the injections.

2.3. Neuroepithelial Cell Differentiation

Neural induction of well plate controls for all injection in this chapter was executed as previously described [123]. Briefly, hESCs were passaged with Accutase (Life Technologies) onto Matrigel-coated plates at a density of $1x10^5$ cells/cm^2 with 10 μM ROCK inhibitor (Y27632; R&D Systems). The following day, cells were changed to E6 medium (ThermoFisher) for 5 days with daily, complete media changes. At the 5^{th} day cells were fixed with 4% PFA and stained for polarization marker N-Cadherin and neural progenitor marker Pax6 to validate the cells for injections.

2.4. Fabrication of hydrogels with varying diameters of internal architecture using fishing line

Alginate hydrogels were fabricated within custom 3D printed Dental Resin molds as described in Chapter 3 (*see Section 2.2*). Briefly, 750 μL solution of sterile 2% sodium alginate was combined with 40 μL of 5% $CaSO_4$ create a $CaSO_4$-alginate slurry. The slurry was vortexed and pipetted into

the device to encapsulate around suspended fishing line of 180, 200, 250, 300, and 400-micron diameters, and allowed to pre-gel for 5 - 10 min. The devices were submerged in a room-temperature bath of 2% (w/v) $CaCl_2$ in deionized water overnight to induce bulk hydrogel gelation. To promote cell compaction and channel-long stem cell aggregation, an alginate hydrogel fabrication post-modification was performed to restrict cell exit from the hydrogels during the injection process as described in Chapter 3 (*see Section 2.8*). Briefly, hydrogels were sealed by collecting them post-fabrication from the 3D printed devices, dipping the outlet port in a 50mM solution of EDTA for 5-10 minutes to re-liquify that end. The re-liquified end was dipped in fresh 2% (w/v) alginate solution, and subsequently dipped in 2% (w/v) $CaCl_2$ for 10 minutes. Sealed hydrogels were stored in E8 media plus PenStrep and 10μM Rock Inhibitor until injection. For bioreactor culture, a secondary hydrogel encapsulation was performed the day after stem cell injections to prevent cells from exiting the channel due to differential pressure created by sealing one end of the hydrogels, as described in detail in section 2.8 of Chapter 3. 3D printed Dental Resin devices and gel loading tips were autoclaved, and the devices were assembled in a sterile cell culture hood. The fishing line were sterilized with 70% ethanol an UV for 1hr prior to assembly into 3D printed Dental Resin device. Tweezers to handle the fishing line were sterilized by autoclave prior to hydrogel fabrication.

2.5. Injection of human embryonic stem cells into hydrogel cavities

A PHD Ultra™ syringe pump was loaded with a 3cc syringe connected via tubing to a 1-200 uL gel-loading pipette tip. The cells were collected using the automated withdraw setting and injected into the alginate hydrogel's molded channel at rates between 1-100 nL/s in a sterile cell culture hood. Injection flow rates varied depending on the diameter of the fishing line used to

mold the channels. The injection process was visualized using an EVOSTM XL Core Imaging System (ThermoFisher). This process was repeated for all the hydrogels. Stem cell injected hydrogels were cultured in E8 media with Penstrep for 1 day in a cell culture incubator and aggregate formation was assessed the next day via brightfield microscopy. Tweezers to handle the hydrogels, microfluidic tubing, luer lock needle, and gel loading tip were autoclaved prior to hydrogel fabrication.

2.6. Neural organoid derivation

One day post-injection, cylindrical cellular aggregates were differentiated under chemically defined conditions using traditional cerebral organoid protocols vs. our custom protocols for generating neural rosettes in 2D well plates [123] and single neural rosettes in 2D micropatterned substrates[126], with or without the addition of dual smad inhibitors, within or without bioreactor culture, and for 4, 8, 10 or 16 days.

2.6.1. Organoid derivation using chemically defined E6 media

A published protocol developed in our lab for efficient differentiation of hPSCs into neuroepithelium without the use of small molecule TGF-Beta family inhibitors was used [123]. Briefly, after 1 day in E8 media with Rock Inhibitor and Penstrep, as described in Section 2.5, injected cylindrical aggregates were transferred to E6 media with 1:200 Penstrep for up to 16 days of culture.

2.6.2. Chemically-defined adaptation of cerebral organoid derivation protocol

Hydrogel encapsulated, cylindrical hESC aggregates were transferred from E8 to E7 media, which consists of E6 media containing 4ng/mL FGF2 , 10mM Rock Inhibitor, 1:200 PenStrep, 1% (v/v)

Glutamax, and 1% (v/v) MEA-NEAA, for 5 days. This is Phase 1 of derivation in which germ layer differentiation occurs. FGF2 and Rock Inhibitor were removed after 3 days of culture. From day 6 to day 10 (Phase 2), cylindrical aggregates were transferred to neural induction media (NIM) consisting of E6 media containing 1% Glutamax, 1% MEA-NEAA, 1ug/mL Heparin, 1% N2 supplement and 1:200 Penstrep. If cultured onto Phase 3, neuroepithelial organoids were transferred to a cerebral differentiation media (CDM) consisting of 50/50 base media of E6 and Neurobasal containing 0.5% (v/v) of N2 supplement, 0.5% (v/v) of MEA-NEAA, 1% (v/v) B-27 without vitamin A (retinoic acid), 1% (v/v) glutamax, and 1:200 PenStrep for 6 days.

2.6.3. Dual smad inhibition

The organoid derivation protocol as described in Section 2.6.2 was used. Briefly, 1 day post-injection, cylindrical aggregates were transferred to E7 media for Phase 1 culture with 100nM LDN-193189 and 10nM SB-431542 dual Smad inhibitors to inhibit non-neural fate specification. Inhibitors were removed at the end of Phase 1 prior to neural induction Phase 2.

2.6.4. Static vs Bioreactor Culture

After injection of stem cells into alginate hydrogels and 1 of day culture in E8 media with Penstrep, cylindrical aggregates were transferred either to E7 media for differentiation using chemically adapted cerebral organoid protocols or E6 media. Organoids were cultured under static conditions in 12 well plates with 3mL of the appropriate media, and media was changed every other day according to Section 2.6.1 for E6 differentiation protocol or Section 2.6.2 for chemically adapted cerebral organoid differentiation protocol. For bioreactor organoids, injected cylindrical aggregates were transferred to a sterile 125 mL Pyrex Spinner flask (ThermoFisher)

agitated on an orbital shaker (Scilogex, Cat. No. SK-0330-Pro) after 1, 5 or 10 days of of static culture. Complete media changes were conducted every other day.

2.6.5. Determining the effect of culture period on neuroepithelial polarization

Hydrogel encapsulated, cylindrical cell aggregates were cultured for 4, 8 or 16 days using E6 differentiation protocol, or E7/NIM/CDM differentiation protocol for 10 or 16 days. Neuroepithelium formation was assessed as determined by organoid translucence under brightfield microscopy and N-cadherin polarization type and size via confocal microscopy (see more details in Section 2.7).

2.7. Organoid Fixation, Sectioning and Immunochemistry

After culture, hydrogels containing organoids were washed with PBS 3 times for 10 minutes, and subsequently fixed with paraformaldehyde (PFA) for 15 minutes. After fixation, hydrogels were transferred to a 30% sucrose-PBS solution for 1-3 days. Next, the organoids were removed from the hydrogels by incubation in a 100mM EDTA solution for 1hr, collected by gentle pipetting using a cut 1000 uL pipette tip, and embedded in OCT compound (Sigma-Aldrich) until sectioning. Organoids were sectioned as 30 - 40um thick slices onto Superfrost Plus microscope slides (ThermoFisher). The slides were washes 4 times with TBS to remove OCT, blocked with TBSDT (Tris Buffered Saline + 5% Donkey Serum + 0.3% Triton X), and incubated in primary antibodies against mouse-anti-N-Cadherin (BD Biosciences, Cat. No. 610920) and rabbit-anti-Pax6 (Biolegend, Cat. No. 901301), or mouse-anti-N-Cadherin and rabbit-anti-Laminin (Abcam, Cat. No. ab30320) for 3 days. All primary antibodies were used at a 1:250 dilution. After incubation, the slides were washed 5 times with TBST (TBS + 0.3% Triton X) and incubated for 1 day in secondary antibodies Alexa 488® donkey-anti-mouse and Alexa 555® donkey-anti-rabbit (1:250,

ThermoFisher) and stained with DAPI (Invitrogen, Cat. No. D1306) for 20 minutes prior to washing with TBS 5 times. Slides were mounted using Prolong Gold anti-fade (ThermoFisher) under No.1 coverslips (ThermoFisher) and imaged using a Nikon AR1 confocal microscope.

3. Results

3.1. Using PVOH-Ca sacrificially molded alginate hydrogels to control microscale neuroepithelial organoid morphology

Human pluripotent stem cell derived organoids have revolutionized the ability to model developmental morphogenesis in vitro. However, standard organoid derivation protocols initiate using a microscale spheroidal cell aggregate morphology, which is achieved upon spontaneous aggregation of cell suspensions but is not mimetic of many tissue-specific developmental processes [11], [135]. Here, the platform establish in Chapter 3 was used to form cylindrical aggregates within PVOH-Ca casted alginate hydrogel to engineer neuroepithelial organoids of microscale cylindrical morphology, which is mimetic to the embryonic neural tube that gives rise to all CNS tissues [37]. Published protocols developed in our lab were followed for generating highly efficient neuroepithelium derivation in 2D without small molecule TGF-Beta family inhibitors [121], and applied to the differentiation of cylindrical aggregates into neuroepithelial organoids.

In order to mimic the germinal neuroepithelial tube's tubular morphology [124], PVOH-$Ca(C_2H_3O_2)_2$, fiber templates with an elliptical cross-section of ~300 x 600um minor and major axes were used to sacrificially mold alginate hydrogels. H9 hESCs were injected into the alginate hydrogels' sacrificially molded channel, cultured for 24hrs in static well plate culture, and

transferred to stirred tank bioreactor culture for up to 15 additional days (**Fig. 2A and 2B**). Cylindrical cell aggregate morphology and morphogenesis were analyzed at 4, 8, and 16 days of culture. In comparison to the initial PVOH-Ca($C_2H_3O_2$)$_2$ templates, the morphing aggregates' dimensions never exceed that of the template, and in many cases, appeared to contract to dimensions smaller than the molded channels over the culture period (**Fig. 2B and 2C**). Formation of polarized rings by Pax6$^+$ NECs, a.k.a. neural rosettes [123], with apical N-Cadherin$^+$ polarization and basal laminin deposition were observed by both Day 8 and 16 of bioreactor culture but largely absent at Day 4 (**Fig. 2D**). At Day 4 primarily small foci of N-Cadherin$^+$ polarization were observed, and as the bioreactor culture proceeded through Day 16, the number of N-Cadherin$^+$ polarization foci decreased significantly while both the number and size of neural rosettes increased significantly (**Fig. 2E**). These results demonstrate that PVOH-Ca($C_2H_3O_2$)$_2$ template-molded alginate hydrogels can be used to engineer neuroepithelial organoids, the initial phase of neural organoid derivation [16], with a biomimetic, microscale cylindrical versus spheroidal morphology.

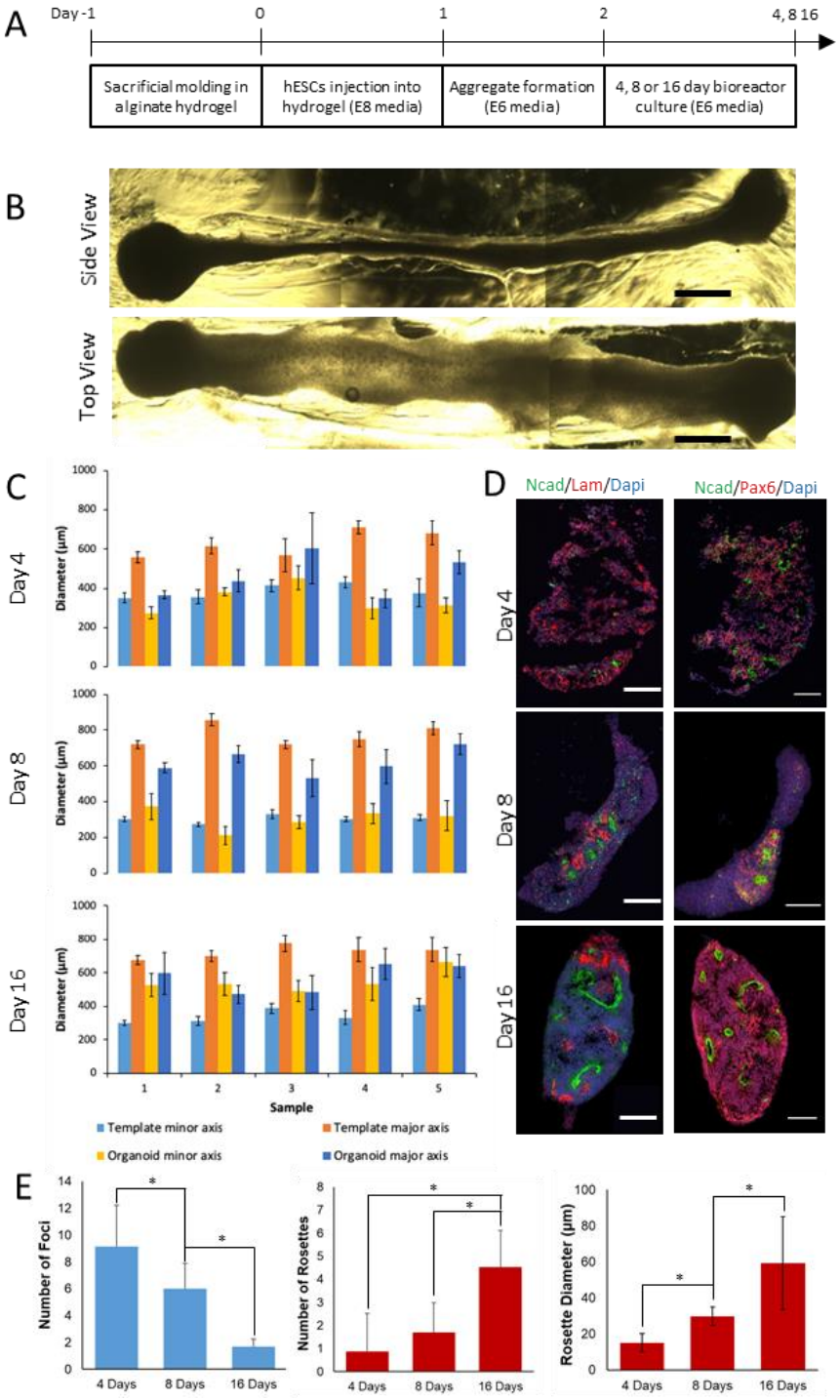

Figure 2: Engineering neuroepithelial organoids using sacrificially molded alginate hydrogels. (A) Experimental timeline of neuroepithelial organoid derivation. Alginate hydrogels were prepared the day before injection. (B) Brightfield image of organoids after 16 days of culture demonstrating their elliptical morphology. (C) Quantification of organoid dimensions after 4, 8, and 16 days of bioreactor culture (n=5 organoids). The PVOH-Ca(C2H3O2)2 template dimensions were measured before sacrificial hydrogel molding. (D) Immunocytochemistry of neuroepithelial organoid cryosections for basement membrane protein Laminin (Lam) and NEC polarization marker N-cadherin (NCad) after 4, 8, and 16 days of bioreactor culture. (E) Quantification of the average number N-cadherin+ polarization foci and rosettes per cryosection (left) and the average rosette diameter (right). Scale bars are (B) 500 and (D) 100 μm.

3.2. The influence of cylindrical aggregate diameter on neuroepithelial organoid morphogenesis.

In the previous section, the feasibility of our platform to generate neuroepithelial organoids (NEOs) with analogous cell phenotypes and cytoarchitectures found in nascent cerebral organoids [16] as well as 2D neural rosettes cultures [123] was demonstrated. However, these NEOs did not display a singular neuroepithelial tube structure, which is mimetic of the in vivo neural tube [37]. Thus, we investigated whether NEO morphology significantly affected the emergence of a singular neuroepithelial tube structure.

Previously in our lab, it was discovered that H9 hESC-derived, forebrain neuroepithelial tissues cultured on 250 μm-diameter circular micropatterns produce singular rosette structures at a >80% efficiency [126]. This contrasts with culture on larger or smaller micropatterned regions which increased the percentage tissues displaying multiple rosettes or no rosette, respectively. Additionally, it was found in the previous section that the largest rosette and polarized tissues region sizes within the organoids were observed at 16 days of culture and were approximately 60um and 200um, respectively (**Fig. 2D and 2E**). These findings were used to inform the experimental approach used in this section, in which hydrogel channels of different diameters were tested-3 different fishing line gauges of 180mm, 250um and 400mm in diameter were used to mold channels within the alginate hydrogels. Fishing line was used instead of micro-injection molded PVOH-Ca templates for testing convenience and efficiency (**Figure 3A and 3B**).

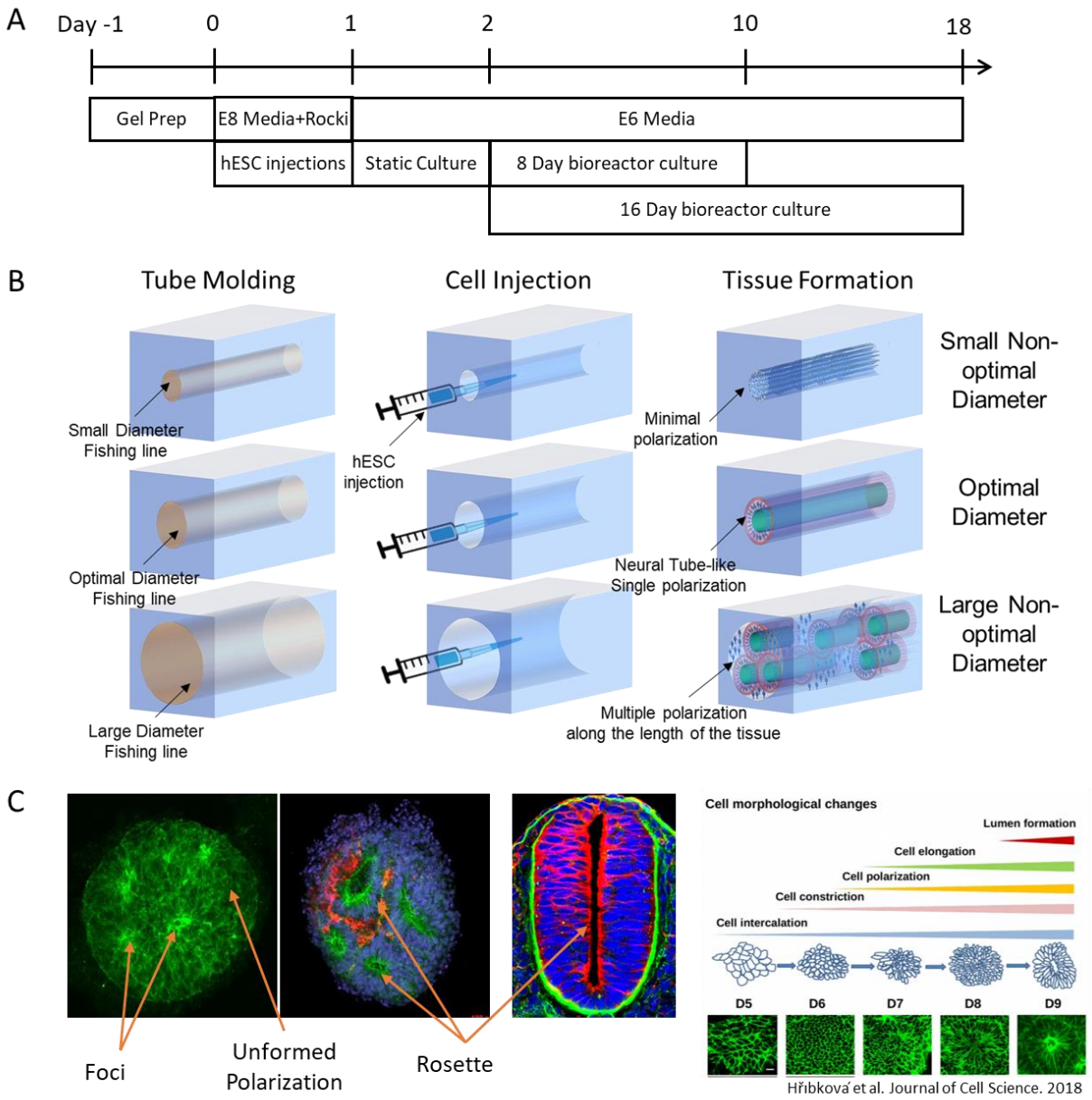

Figure 3: Strategy to optimize single polarization emergence using fishing line. (A) Timeline of hydrogel preparation, injection, media, and culture period. (B) Schematic showing the strategy for generating neuroepithelial tube organoids with a single polarized lumen the length of the tissue. Different diameters will be tested ranging from 180um to 400um. (C) Quantification of percentage of polarization types (Foci, Rosettes, Unformed), polarization number and polarization stage (stages 1-4 will be counted in one group and stage 5 in another). Cell morphological changes diagram adapted from Hřibková et al. 2018.

Post hydrogel molding, the resulting micro-channels were imaged and quantitatively analyzed (**Fig. 4A and 4B**). Dimensional analysis revealed that the molded channel diameter deviated from the initial fishing line geometry by an average of 19.77 ± 7.03%, 3.77 ± 4.62% , and 11.11 ± 9.64% for 180, 250, and 400μm diameter fishing line mold at any point along its axis, i.e. 5

measurements per molded channel. As demonstrated using the PVOH-Ca templates in Chapter 2, this demonstrates reproducible casting of microscale architecture within diffusion limited, ionically crosslinked alginate hydrogels.

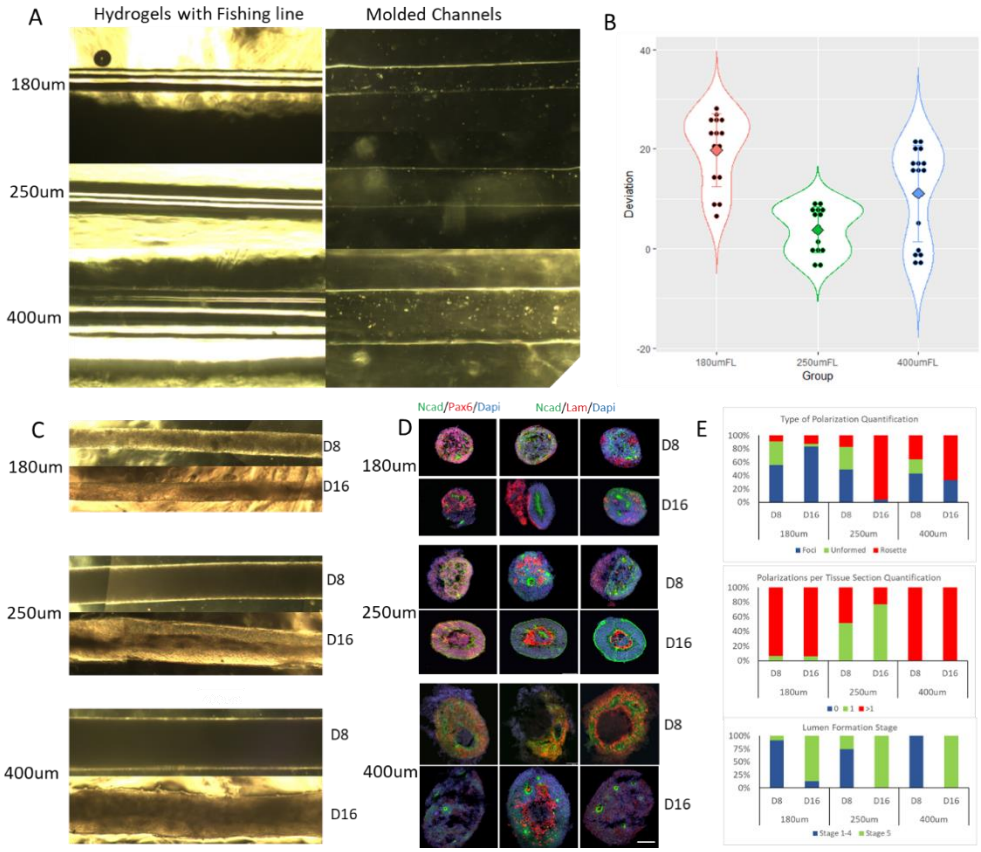

Figure 4: Proof of principle demonstration of the effect of morphological control on the formation of single polarized neuroepithelium. (A) Brightfield images of 180, 250, and 400um diameter fishing line inside an alginate hydrogel (left) and the molded channels after hydrogel crosslinking. (B) Dimensional analysis of molded hydrogel channels showing the percent deviation from the fishing line diameter. (C) Brightfield images of stem cell injected hydrogels at 8 or 16 days of culture for all sizes. (D) Immunochemical analysis of cryosections obtained from all tissues. Each section was stained for N-Cadherin and Pax6 (left) or Laminin (right). (E) Quantification of the ratio of type of polarization (Top), amount of polarizations per section (middle), and lumen formation stage of each cryosection (Bottom). 1 tissue and 3-4 sections/per tissue for 400um size for each day, 3 tissues and 10-18 sections for 180um size for each day, 3 tissues and 10-16 sections for 250um for 8 days, 1 tissue for 250um size for 16 days.

In established cerebral organoid differentiation protocols that utilize chemically undefined reagents, EB aggregates display surface clearing and brightening during the initial stages of differentiation in which neural induction is occurring (see **Fig. 1A**, Chapter 3) [134]. The bright, smooth surfaces of the aggregate are optically translucent neuroepithelium and form between

7-10 days of culture. Upon further culture, these area gives rise to neuroepithelial buds, which serve a morphogenesis centers producing the biomimetic microscale structures within cerebral organoids. Thus, in our experiments, the formation of neuroepithelium was assessed in cylindrical organoids of all sizes at 8 days and 16 days of culture. At 8 days, minimal differences we found between organoids of different sizes and neuroepithelial brightening was not observed in any of the conditions (**Fig. 4C**). This is indicative of late germ layer differentiation when compared with traditional organoid protocols. At 16 days of culture, it was found that 180um and 400um organoids displayed little neuroepithelial brightening at their edges, but rather a mixture of areas with relatively translucent areas intermixed with dark tissues areas was observed. However, the 250um organoids displayed neuroepithelial brightening spanning the entire length of the organoid, and it was primary localized around the periphery of the organoid, which is indicative of neuroepithelium formation (**Fig. 4C**) [16].

After assessing the tissues for the formation of neuroepithelium, they were sectioned and stained to assess organoid morphogenesis as a function of days in culture. During neural induction, neuroepithelium polarization occurs in 5 stages: cell intercalation (stage 1), cell constriction (stage 2), cell polarization (stage 3), cell elongation (stage 4), and lumen formation (stage 5)[136]. Formation of polarized rings by $Pax6^+$ NECs, a.k.a. neural rosettes [123], with apical N-$Cadherin^+$ polarization and basal laminin deposition were observed by both Day 8 and 16 of bioreactor culture for all organoid sizes tested (**Fig. 4D**). To determine the differences in morphogenesis of each group, the amount of polarization by type (small Foci or Rosettes) was quantified for all conditions (**Fig. 4E**), following the polarization classification shown in **Fig. 3C**. At day 8, the 180 μm diameter organoids exhibited mostly small foci of N-$Cadherin^+$ polarization

and/or a phenotype consistent with cellular polarization stage 3 of lumen formation (**Fig. 4D and 4E**). 250 and 400 μm diameter organoids displayed similar level of polarization progression (stage 3), while also showing fewer polarization foci and slightly higher levels of larger rosette emergence. Additionally, 400μm diameter organoids displayed areas of necrotic cell death, presumably due to lack of oxygen and nutrient transport to the tissue core. At 16 days of culture, all tissues displayed minimal levels of foci and appeared to be at stage 5 of N-Cadherin polarization, indicated by clear polarization of N-Cadherin to form foci or rosette lumens (**Fig. 4D and 4E**). At a 180 μm diameter, while some sections within the organoid displayed a polarization phenotype analogous to that of the in vivo neural tube, it was not observed consistently through the entire organoid (**Fig. 4D**). At a 400 μm diameter, an increased number of polarizations formed as compared to the other 2 conditions, but no single rosettes were observed in any of the sections. However, at a 250 μm diameter organoids exhibited the ability to generate a single polarized neuroepithelium with biomimetic organization of N-cadherin and laminin, as compared to the in vivo Neural Tube (**Fig. 4D and 4E**). Although the efficiency of single neuroepithelium formation was low, these results indicate that channel size and duration of culture can have a profound influence in the ability influence the microscale morphology of nascent cerebral organoids. In the next sections, additional conditions were tested to assess whether the efficiency of single polarized neuroepithelium formation could be improved.

3.3. Adaptation of traditional organoid protocols using chemically defined reagents.

In the previous section, the influence of cell aggregate diameter in the formation of singular polarized neuroepithelial organoids under the E6 chemically defined differentiation media was evaluated. While the ability to form a single polarized neuroepithelial tube was demonstrated

with 250 μm diameter aggregates differentiated over 16 days, the reproducibility of this organoid derivation paradigm remains a challenge. In this section, the use of traditional cerebral organoid differentiation media was explored to determine its effect on reproducible singular neuroepithelial tube formation within our bioengineered cylindrical aggregate paradigm.

This first stage (Phase 1) of standard cerebral organoid derivation is germ layer specification within EBs, and it is achieved using a medium consisting of DMEM-F12, KOSR, FBS, Glutamax, MEM-NEAA, 2-mercaptoethanol and low levels of bFGF2. During neural induction (Phase 2), EB's are transferred to neural induction media (NIM) consisting of DMEM-F12, GlutaMAX, MEM-NEAA, Heparin, and N2 supplement. During this phase, bright and smooth surfaces of the EB aggregates form optically translucent neuroepithelium between 7-10 days of culture. During Phase 3, the neuroepithelium-stage organoids are embedded in Matrigel and transferred to cerebral differentiation media (CDM) containing a 50/50 base media of DMEM and Neurobasal, and supplemented with MEA-NEAA, glutamax, PenStrep, insulin, reduced levels of N2 supplement, and B-27 supplement without vitamin A (retinoic acid). In this Phase, the neuroepithelium typically gives rise to neuroepithelial buds, which produce the biomimetic microscale structures of cerebral organoids. Finally, upon extended culture in a spinner flask bioreactor, the stem cells within the neuroepithelial bud execute corticogenesis to produce a cerebral organoid (**Fig. 5A and 5C**)[134].

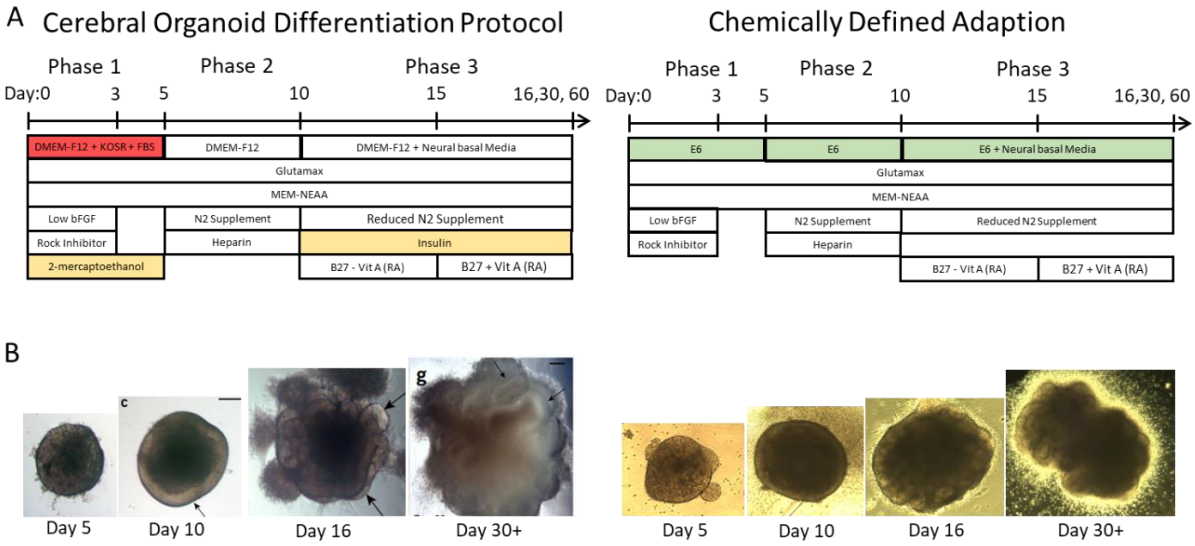

Figure 5: Chemically defined adaptation of traditional cerebral organoid differentiation protocols. (A-B) Organoid culture timelines. E6 is used as base media (B) to replace chemically undefined components (denoted in red) in published organoid protocols (A). 2-mercaptoethanol used to stabilize the components in the undefined media formation is no longer need and removed. Insulin is also removed as it is already present in E6 media. (C-D) Brightfield images of organoid culture progression, showing that organoids differentiated in the chemically defined formulation (D) exhibit similar physical characteristics as the original media formulation (C). A and B Adapted from Lancaster et al. 2014.

Using this protocol, the ability to form cerebral organoids displaying remarkable levels of biomimetic forebrain cytoarchitecture has been demonstrated widely. However, the organoids show significant variability, particularly between preparations, due to a variety of factors such as the lack of surrounding embryonic tissues important signaling cross-talk, overlying meninges, and vasculature that provides oxygenation to enable unlimited tissue growth without forming necrotic zones [134]. Additionally, the presence of chemically undefined reagents such as albumin in KOSR media, FBS, and Matrigel further exacerbates the variability between batches and between different cerebral organoid protocols. Therefore, in this section, we also aimed to test whether a chemically defined adaptation of traditional cerebral organoid derivation medias could be used to reproducibly bioengineer neuroepithelial tube organoid in our novel platform (**Fig. 5B and 5D**). For Phase 1, the media was modified by substituting the base media of DMEM, KOSR and FBS with E6 media, and supplemented the E6 with the remaining factors (glutamax,

MEA-NEAA, and low FGF2). As E8 also contains FGF2 and TGB, this media formulation was denoted as E7. For Phase 2, the DMEM base media and heparin was replaced as well with E6 and supplemented with the remaining components (glutamax, MEA-NEAA, and N2 supplement). For Phase 3, the base media of DMEM and the mercaptoethanol were replaced with base E6 media, which contains insulin, supplemented with the remaining factors (MEA-NEAA, glutamax, PenStrep, reduced levels of N2 supplement, B-27 supplement without vitamin A).

To validate the efficacy of our chemically modified media formulations, spherical cerebral organoids were formed and analyzed via immunostaining at 16, 30 and 60 days of culture. The results were compared to those of published cerebral differentiation protocols (**Fig. 6A**) [16]. After 16 days of culture, discrete brain regions were formed as evidenced by polarization/neural progenitor markers N-Cadherin and Pax6, frontal/occipital Lobe marker TSHZ2, early neural progenitors/forebrain markers Sox2 and FoxG1, and hippocampal marker NRP2. The antibody for the Frontal lobe marker LMO4 did not appear to exhibit staining, probably due to the difference in the antibody used in the published protocol and the one used herein. The antibody used in the original publication was no longer available through the original vendor. Additionally, maturation and organization was observed at 30 and 60 days, as evidenced by radial glia/outer radial glia markers Pax6 and phospho-Vimentin, neural and intermediate progenitor marker Map2, Cajal Retzius-CP/Pre plate markers reelin and TBR1, early neuron markers DCX1 and Tuj1, and cortical layer II and IV markers CTIP2 and SATB2 (**Fig. 6B**). While the intermediate progenitor marker TBR2 did not seem to have stained properly, the presence of other intermediate progenitor markers such as MAP2 suggest these cell types were present. Overall, these results validate the chemically defined modification of traditional organoid differentiation protocols. Thus, in the following

section the use of this modified protocol was investigated on our bioengineered organoid platform to further optimize reproducible single neuroepithelial formation.

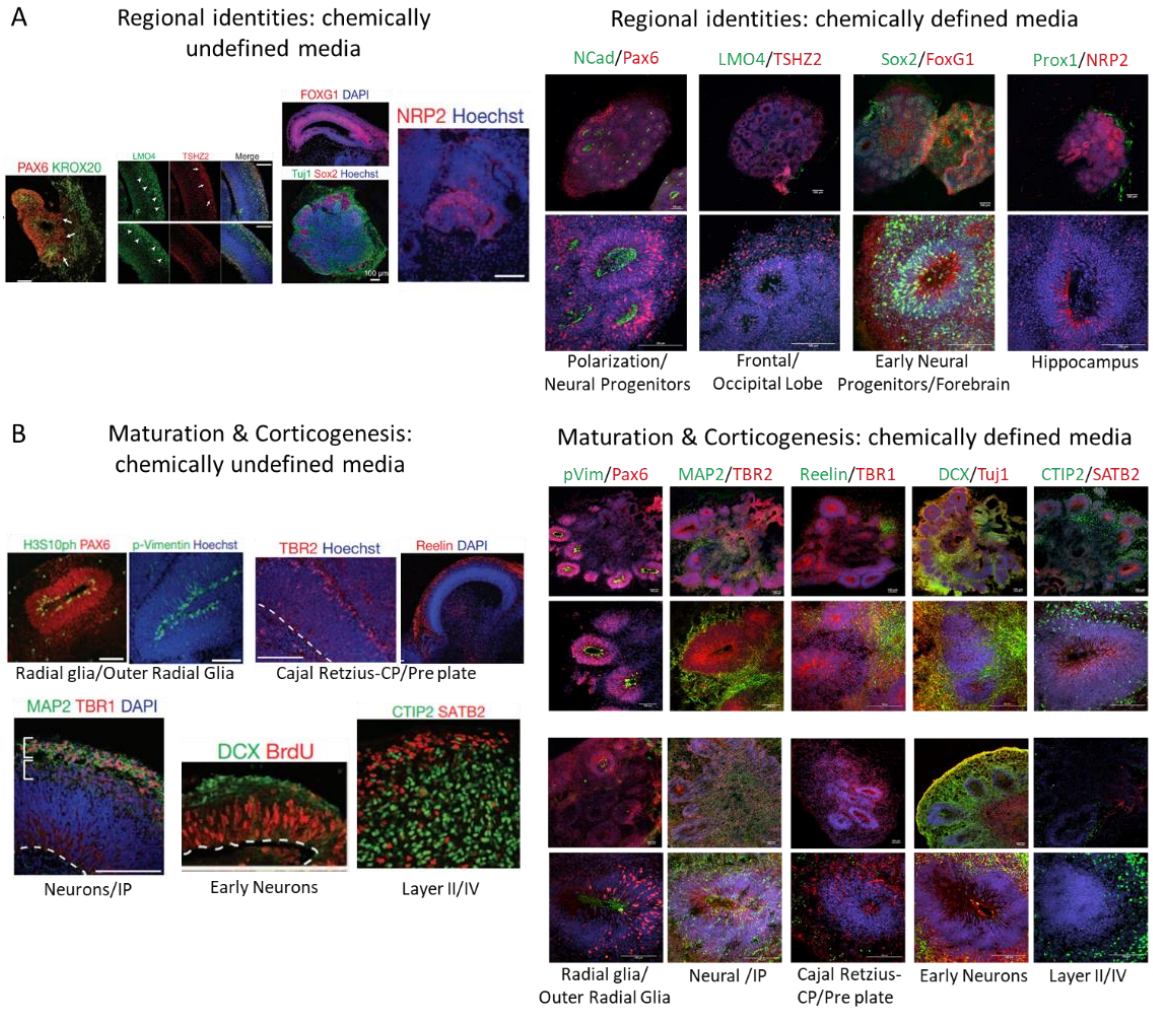

Figure 6: Immunochemical analysis of Cerebral Organoids differentiated under chemically defined conditions. (A) Organoids cultured for 16 days show discrete brain regions are formed as evidence by polarization/neural progenitors markers N-Cadherin and Pax6, frontal/occipital Lobe marker TSHZ2, early neural progenitors/forebrain markers Sox2 and FoxG1, and hippocampal marker NRP2, as compared to organoids differentiated under traditional chemically undefined media. (B) Maturation and organization is observed at 30 and 60 days of culture, as evidenced by radial glia/outer gadial glia markers Pax6 and phospho Vimentin, neural and intermediate progenitor markers Map2 and TBR2, Cajal Retzius-CP/Pre-plate markers reelin and TBR1, early neuron markers DCX1 and Tuj1, and cortical layer II and IV markers CTIP2 and SATB2, as compared to organoids differentiated under traditional chemically undefined media.

3.4. The influence of cylindrical aggregate diameter using chemically defined adaption of cerebral organoid differentiation protocol.

In Section 3.2, it was observed that a single polarized neuroepithelial tube can be derived by differentiating 250μm diameter, cylindrical hESC aggregates over 16 days in just E6 media. However, this protocol was not reproducible. One of the limitations observed was variability in cell survival during stirred-tank bioreactor culture, as evidenced by the presence of tissue discontinuity and lack of tissue brightening indicative of neuroepithelium formation. The original justification for use of bioreactor culture was the importance of convective flow for facilitating nutrients and oxygen transport through the alginate hydrogel and within growing 3D tissues growth. However, convective flow in Phase 1 and 2 of organoid derivation may contribute to the aggregate discontinuity and disassembly: even in traditional cerebral organoid derivation protocols, no convective flow is used during Phases 1-3 [134]. This methodological uncertainty was investigated using bioreactor versus static culture of 250μm diameter cylindrical aggregates and the chemically defined adaptation of cerebral differentiation media (**Fig. 7**).

Bioreactor and static culture of cylindrical aggregates in the first 2 phases of cerebral organoid derivation were compared, using E7 media for Phase 1, NIM for Phase 2, and CDM for phase 3 (**Fig. 7A**). It was found that bioreactor culture from Phase 1 caused inconsistent organoid viability, while Phase 2 bioreactor culture or Phase ½ static culture yielded intact organoids displaying neuroepithelial brightening (**Fig. 7B**).

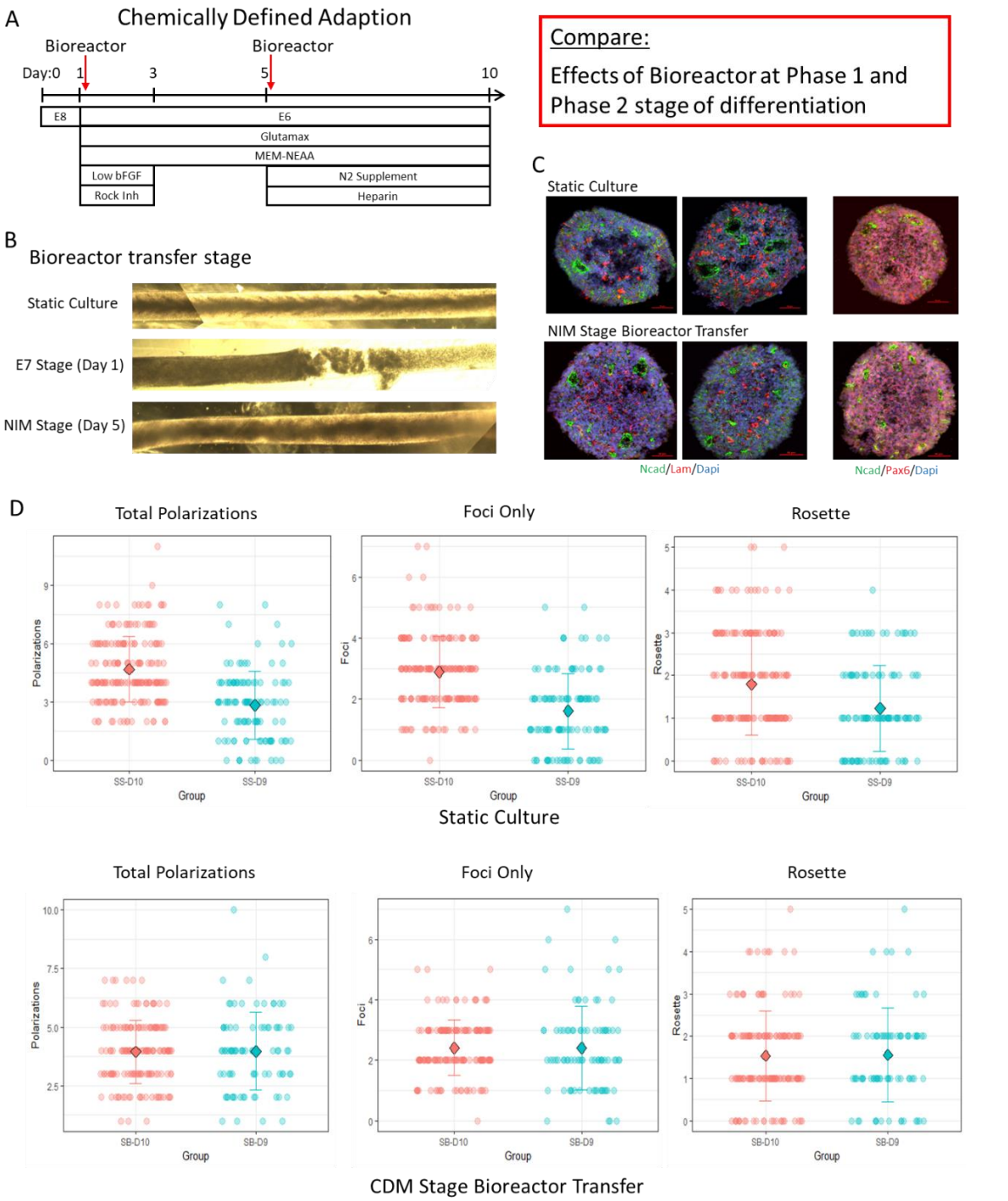

Figure 7: Chemically defined derivation of NEOs under static or bioreactor culture. A) Timeline of differentiation. Red arrows denote the different time periods in which engineered cylindrical organoids were transferred to bioreactor culture. These we compared to a static culture condition. B) Brightfield images showing the effects of bioreactor culture at the different stages of differentiation. Transfer at the NIM stage has detrimental effects on organoid integrity. Tissues in this condition were therefore not analyzed further. C) Immunochemical analysis of cryosections obtained from all tissues. Each section was stained for N-Cadherin and Pax6 (right) or Laminin (left). D) Quantification of the total amount of Polarizations (left), and of those the amount of foci (middle) and rosettes (right) for both conditions analyzed at day 9 and day 10. N=3 tissues per condition, 30+ section per tissue.

Immunochemical analysis of Phase 2 bioreactor and Phase 1/2 static culture organoids showed that they both contained polarized rings by $Pax6^+$ NECs, a.k.a. neural rosettes [123], with apical $N\text{-}Cadherin^+$ polarization and basal laminin deposition (**Fig. 7C**). No differences in polarization behavior were observed, and for both conditions the N-Cadherin polarizations seemed be to restrict to periphery of the tissue, concurrent with the neuroepithelial brightening observed under brightfield microscopy, and in agreement to neural induction patterns observed in other cerebral organoid protocols [134] (**Fig.7C**). Also, no differences between the groups were observed in the number of polarizations for both foci and rosettes, with foci being slightly more prevalent for both conditions (**Fig. 7D**).

To have a direct comparison with the single neuroepithelial organoid generated in Section 3.2 under E6 neural differentiation for 16 days of culture, a second experiment was conducted in which NIM was extended to Phase 3 and compared with the standard use of CDM in Phase 3. In both Phase 3 NIM and CDM conditions, clear neuroepithelial phenotype and spatial organization of polarization is lost (**Fig. 8B and 8C**). The number of fully formed N-Cadherin polarizations in organoids derived using Phase 3 NIM is dramatically decreased, and when observed, they have a stage 3-like phenotype of N-cadherin lumen formation [136] (**Fig. 8C and 8D**). Organoids cultured in CDM did not alter the number of total polarizations, but rather shifted the ratio of foci to rosettes more towards the prevalence of foci (**Fig. 8D**).

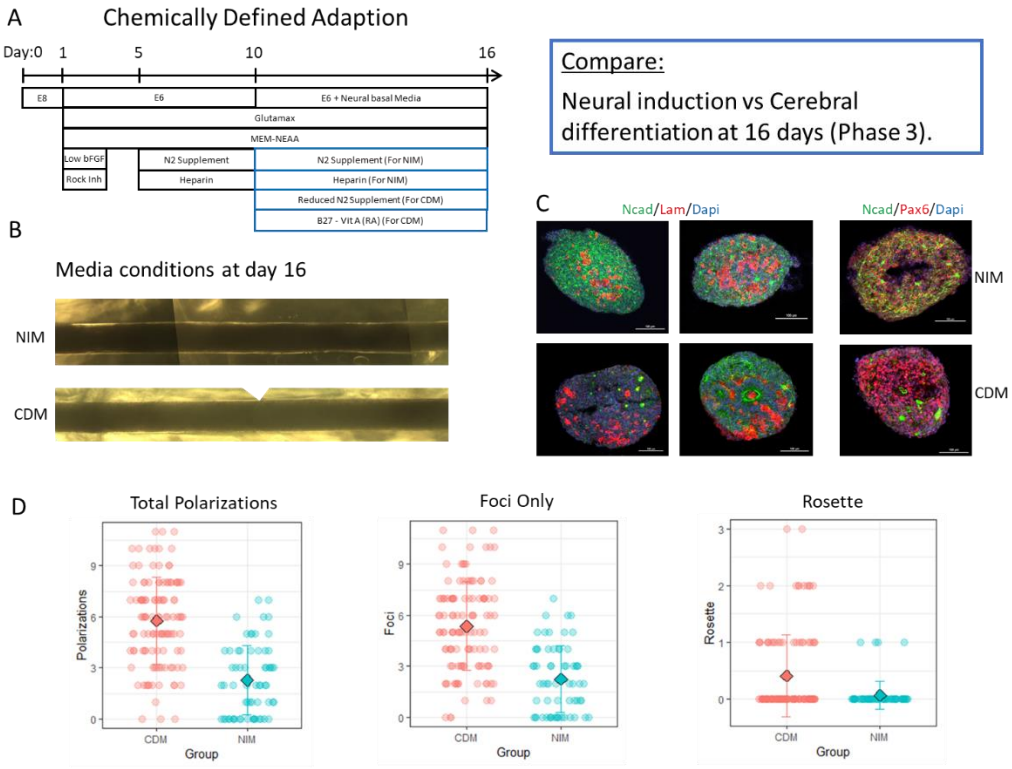

Figure 8: Chemically defined derivation of NEOs at day 16 day comparing Phase 3 NIM or CDM culture. A) Timeline of differentiation. Blue boxes denote the different media conditions used at Phase 3 of differentiation. B) Brightfield images showing the effects of bioreactor culture at the different stages of differentiation. C) Immunochemical analysis of cryosections obtained from all tissues. Each section was stained for N-Cadherin and Pax6 (right) or Laminin (left). D) Quantification of the total amount of Polarizations (left), and of those the amount of foci (middle) and rosettes (right) for both conditions analyzed showing a decrease in total polarizations and rosettes for organoids cultured in NIM, as well as an increase in the ratio of foci to rosette for organoids cultured in CDM for 16 days. N=3 tissues per condition, 30+ sections per tissue.

While this differentiation paradigm did not yield single neuroepithelial organoids, it was demonstrated that the most successful condition tested was differentiating engineered cylindrical aggregates until Phase 2 using NIM irrespective of static or bioreactor culture, as evidence by neuroepithelium formation and polarization phenotype (**Fig. 7 and 8**). It was hypothesized that the lack of single neuroepithelial formation could be in part due to the full tissue not acquiring a homogenous neuroepithelial phenotype, as evidenced by the non-uniform Pax6 expression and polarizations at the tissue's central core (**Fig. 7 and 8**).

To test this hypothesis, the size of the cylindrical aggregates was decreased to eliminate the non-neuroepithelial core observed within 250μm diameter cell aggregates. Cylindrical cell aggregates of 140 and 200μm diameters were formed in alginate hydrogels (**Fig. 9A and 9B**). Dimensional analysis of molded channel diameter deviated from the initial fishing line geometry by an average of 6.86 ± 4.51% and 10.88 ± 3.30% for 140 and 200 μm diameter fishing lines, i.e. 10 measurements per molded channel (**Fig. 9C**). Brightfield images of organoids after Phase 2 of differentiation showed intact tissues displaying neuroepithelial brightening. Additionally, decreasing the tissue diameter from 250 to 200μm minimizes non-epithelial tissue center, and eliminates it at 140μm (**Fig. 9D**). However, full tissue brightening did not translate into single neuroepithelium formation for the 140μm diameter organoids, as evidenced by immunostaining for N-Cadherin. Rather, polarizations were observed throughout the entire tissue rather than restricted to the periphery like in the 200 and 250μm diameter organoids (**Fig. 9E**).

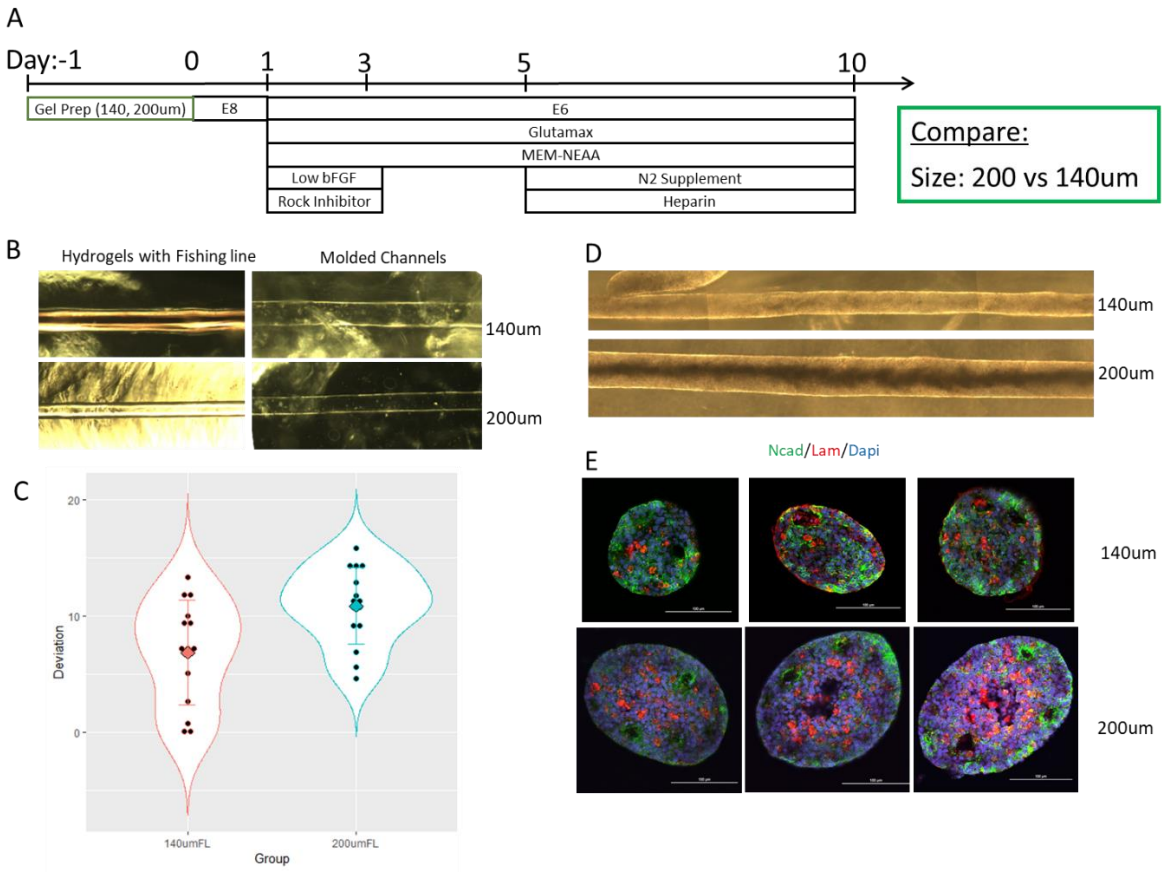

Figure 9: Using chemically defined media adaption of cerebral organoid differentiation on 140 and 200um engineered cylindrical organoids in NIM for 10 days. A) Timeline of differentiation. B) Brightfield images of 140 and 200um diameter fishing line inside an alginate hydrogel (left) and molded channels after hydrogel crosslinking. (C) Dimensional analysis of molded hydrogel channels shows the percent deviation from the fishing line diameter. D) Brightfield images of injected organoids showing neuroepithelial formation at the periphery of 200um organoids, and throughout 140um organoids. E) Immunochemical analysis of cryosections obtained from both sizes tested. Each section was stained for N-Cadherin and Laminin. Polarizations were observed throughout the entire tissue rather than restricted to the core for 140um organoids, while 200um organoids displayed similar phenotype and polarization as observed with 250um organoids.

4. Discussion

In this chapter, the role of cell aggregate diameter, differentiation paradigm and bioreactor or static culture was investigated to determine the optimal conditions for formation of bioengineered neuroepithelial organoids. First, to mimic the dimensions of the developing neural tube, PVOH-Ca templates that had an oval tubular shape were used to cast channels in alginate hydrogels. The E6 protocol was used to differentiate the cylindrical aggregates and cultured for multiple days to assess the neuroepithelium formation [123]. While it was found that the most

optimal condition tested for the formation of larger apical N-Cadherin^{+} rosette polarization was 16 days of bioreactor culture, the organoids appeared to be too large to form a single tissue-large polarization that is observed in vivo during neural tube development [37]. One of the possible factors for this can be the differences in culturing tissues in vitro vs in vivo. In vivo, as the neural tube develops, it is surrounded by the endoderm and mesoderm. As the neural tube is forming these tissues send signaling factors that influence how the neural tube organizes and differentiates [37], and are critical for the interplay of neural and non-neural tissue cross-talk [23]. Thus, the size and shape of optimal tissues generated in vitro may have to be optimized to overcome these differences.

Our lab previously developed a protocol to generate engineered neural rosettes slice cultures using micropatterned substrates that demonstrated a direct influence in the efficiency of biomimetic microscale morphology formation [126]. As with the engineered cylindrical aggregates mentioned above, the efficiency of forming single rosettes structures using biomimetic oblong micropatterned regions proved to be less effective compared to circular micropatterns. Additionally, by controlling the dimension of these circular regions, the efficacy of single forebrain neural rosette emergence was increased to >80% using 250μm diameter micropatterns. These results were used as a guideline to design experiments in which multiple 3D cylindrical aggregate morphologies were tested for biomimetic NEO formation in the presence of E6 differentiation media.

It was found that by varying the sizes from 180 to 400 μm diameter, and by varying the culture conditions, the amount and type of polarizations that were formed were directly impacted. Like in the 2D platform, it was found that by differentiating 250 μm diameter cylindrical aggregates,

in this case for 16 days of culture, a single neuroepithelial tubular organoid that resembled the in-vivo neural tube could be generated. Although this result was not reproducible under these conditions, this is the first proof of principle demonstration of effectively controlling hPSC-derived neural organoid microscale cytoarchitecture.

Our vision is that we can utilize this platform to improve on the current limitations that exist with traditional neural organoid technologies. Improving the reproducibility of neural organoid anatomy will be needed if we hope to use these to replace or build upon animal models in the clinical translation of new drugs and treatments for neurological disorders. Even with the limitations that animal models present, they remain the gold standard for clinical translations studies because of the reproducibility of their wild-type counterparts, which enables the systematic detection of any deviation from normal development [125]. Chemically undefined culture conditions and lack of reproducible macroscale cytoarchitectural features remain the biggest challenge to standardization of neural organoid derivation protocols. In this chapter it was shown that current published protocols could be adapted to chemically defined conditions, as evidenced by the formation of cerebral organoids with similar regional diversity and cortical differentiation [16], [134].

Proof of principle culture of engineered cylindrical aggregates differentiated using a chemically defined cerebral organoid protocol was done to compare with the E6 differentiation protocol. Although differentiation under these conditions did not improve single neuroepithelial tube formation as compared to the E6 method, it was shown that varying the culture conditions, tissue size, and duration of differentiation had a significant impact on the morphogenesis of these engineered organoids. For example, culturing under bioreactor conditions too early in the

protocol (i.e. Phase 1) could adversely affect the integrity of the organoids. Also, in general, no differences were observed between bioreactor culture in the Neural Induction Phase as compared to static condition. In both conditions cultured up to the end of Neural induction, no differences where observed in polarization type and number. However, culturing the engineered organoids up to 16 days by adding the 3rd phase of differentiation in cerebral differentiation media or neural induction media had detrimental effects to the presence of N-Cadherin polarizations. While culturing for 16 days in CDM shifted the ratio of foci to rosettes more towards the prevalence of foci, the number of fully formed N-Cadherin polarizations in organoids differentiated in NIM dramatically decreased and displayed stage 3-like phenotype N-cadherin lumen formation [136]. One possibility is that the loss of fully formed polarizations observed with prolonged culture in NIM for 16 days is due to the aggregates losing the ability to form neuroepithelial buds from the initially formed neuroepithelium, as in published protocols this is reported to be a possible scenario when cultured too long in NIM [23]. Additionally, it is possible that the contraction of N-Cadherin polarizations from the rosettes phenotype to foci under CDM can be due either to the physical restriction caused by the hydrogel channel or lack of Matrigel encapsulation. In traditional organoid cultures, Phase 3 of derivation involves the encapsulation within Matrigel hydrogels. During this process, neuroepithelial buds are formed from the evagination of neuroepithelium, and organoids dramatically expand in size [16], [23]. Since the protocol used herein restricts growth of organoids and Matrigel is not present, these could be contributing factors in the shift in polarizations from rosettes observed in Phase 2 to Foci in Phase 3. However, it is important to keep in mind that Matrigel is a chemically undefined matrix which can further contribute to lack of reproducibility and standardization of organoid protocols, and

thus could unreliable in further attempts to standardize the formation of single polarized Neuroepithelium. Novel chemically defined matrices that support complex organoid differentiation could thus be critical in continuing to advance the standardization of cerebral organoid development. Matrices such as those developed in the Murphy lab for the replacement of Matrigel in the standardization of vascular toxicity screening and stem cell expansion [137], or the development of neural tissues models [138], and likewise those developed in the Spence and Garcia labs for the chemically defined generation of intestinal organoids [139] are prime example of potential candidates for the replacement of Matrigel in organoid differentiation protocols.

These results indicated that the optimal condition to culture engineered organoids under chemically defined adaption of cerebral differentiation protocols is to culture with morphological restriction for 10 days under NIM, and if cultured further to Phase 3, the organoids should be released from the hydrogel restrictions and allow to expand as in traditional organoid protocols with or without Matrigel. Future work will in part be aimed to answer these questions.

Finally, while analogues phenotypes within engineered organoids cultured under chemically defined adaptations of traditional cerebral differentiation protocols were observed, none of the conditions tested yielded a single polarized neuroepithelium as observed within 250 μm diameter organoids under E6 differentiation for 16 days. Further experimentation should be done to determine if in fact the media conditions will also have a role in the formation of reproducible single NEOs.

5. Concluding Remarks

In this chapter a proof a principle formation of single neuroepithelial tube organoid using alginate hydrogels with 250 μm diameter internal cylindrical morphology was demonstrated. To our knowledge, this is the closest demonstration of a neural tube mimetic in vitro, and we believe it is the first step into standardizing the formation of cerebral organoids. To this point, we have successfully submitted a patent application describing the methodology for controlled induction of 3d cylindrical neuroepithelial tubes. Ultimately, the long-term goal is to use a standardized version of this platform to replicate developmentally relevant corticogenesis in cerebral organoids. Integrating this platform with different cutting-edge techniques such as CRISPR-CAS9 mediated gene editing and patient-specific induced pluripotent stem cell reprogramming will provide a power model to study neurodevelopmental and psychiatric diseases that affect the later structures that develop from NEOs, which are the brain, retina, and spinal cord [140]–[143].

Appendix

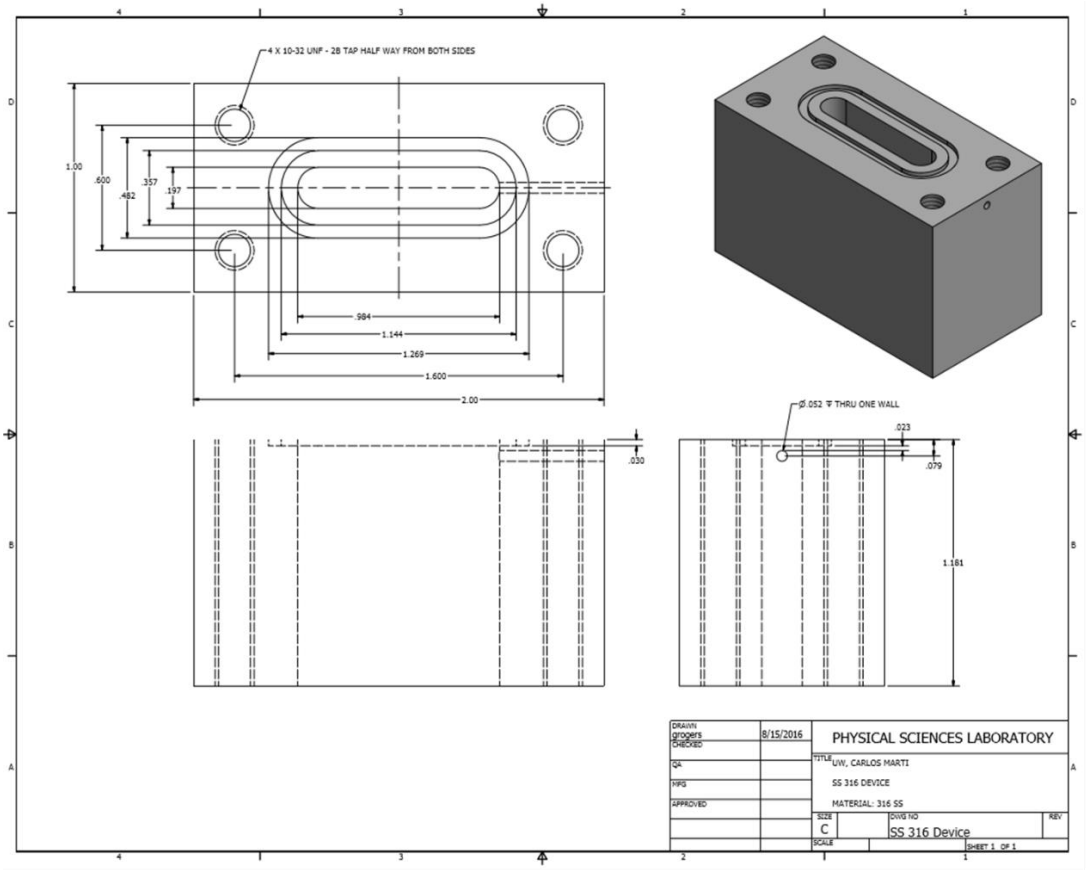

Figure 1: Diagram for the fabrication of a stainless-steel device for the formation of alginate hydrogels with internal architecture (top). The device contains inlet and outlet ports for needles to hold a tube molding material in place, an indentation in which an o-ring is held in place to seal an acrylic base in the bottom of the device, and ports for screws to hold the base in place (bottom).

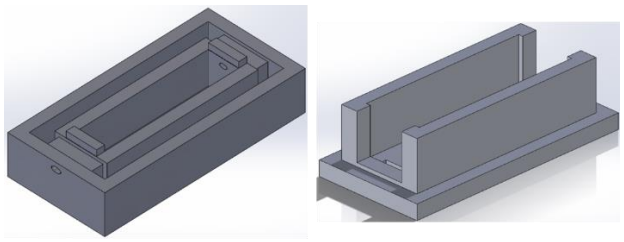

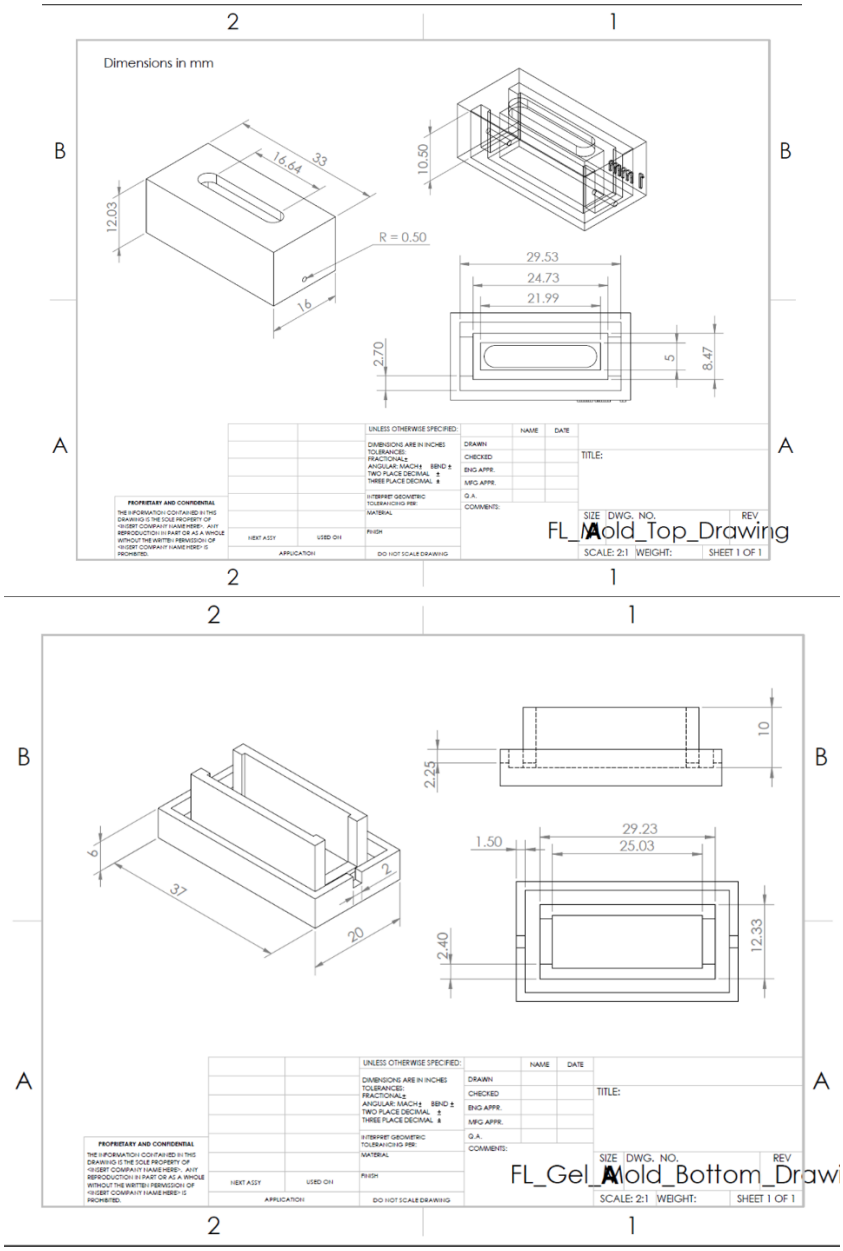

Figure 2: Diagram for the fabrication of a 3D printed dental resin device for the formation of alginate hydrogels with internal architecture. The device contains a top inlet and outlet ports for needles to hold a tube molding material in place, and a bottom piece which was designed to tight fit in place with the top piece.

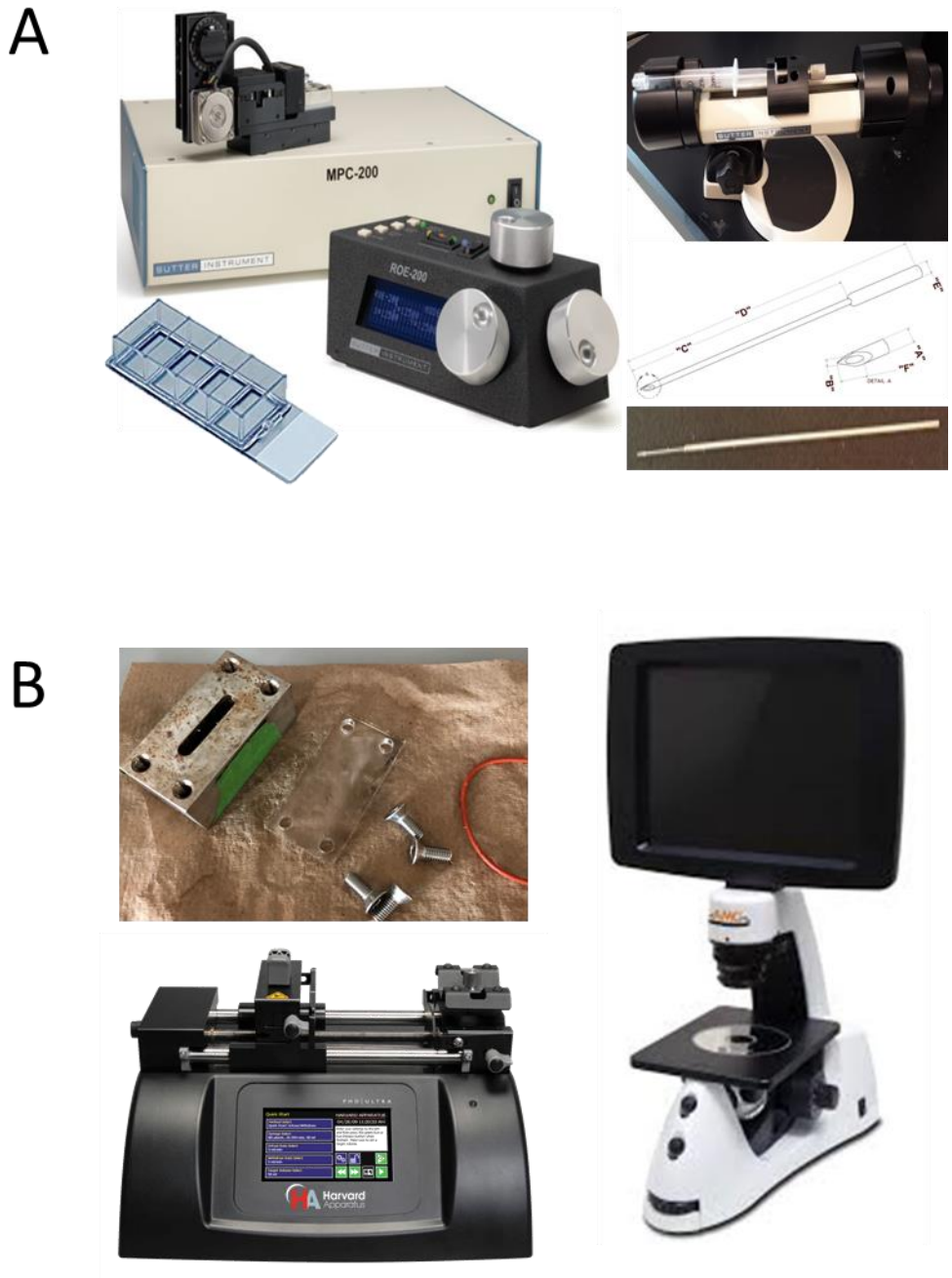

Figure 3: A) Micromanipulator setup from Sutter instruments containing a 35g beveled NanoFil needle Tip Stainless Steel needle, 4 well Nunc™ Lab-Tek™ II Chamber Slide for the fabrication of PVOH-casted Alginate hydrogels, and a manual injector. B) The second method tested for injecting stem cells into alginate cavities using a PHD UltraTM syringe pump loaded with a 3cc syringe connected via microfluidic tubing to a 1-20uL gel-loading pipette tip to inject the cells into the alginate hydrogel's molded channel within a stainless-steel device at rates between 1-100 nL/s. The injection process was imaged using an EVOSTM XL Core Imaging System.

References

[1] S. Pal, “Incidence and Prevalence of Major Neurologic Disorders,” *U.S. Pharmacist*, 2018. [Online]. Available: https://www.uspharmacist.com/article/incidence-and-prevalence-of-major-neurologic-disorders. [Accessed: 05-Nov-2019].

[2] C. L. Gooch, E. Pracht, and A. R. Borenstein, “The burden of neurological disease in the United States: A summary report and call to action,” *Annals of Neurology*, vol. 81, no. 4. John Wiley and Sons Inc., pp. 479–484, 01-Apr-2017.

[3] M. Hay, D. W. Thomas, J. L. Craighead, C. Economides, and J. Rosenthal, “Clinical development success rates for investigational drugs,” *Nat. Biotechnol.*, vol. 32, no. 1, pp. 40–51, Jan. 2014.

[4] V. Tabar and L. Studer, “Pluripotent stem cells in regenerative medicine: Challenges and recent progress,” *Nature Reviews Genetics*, vol. 15, no. 2. pp. 82–92, Feb-2014.

[5] M. Grskovic, A. Javaherian, B. Strulovici, and G. Q. Daley, “Induced pluripotent stem cells ĝ€" opportunities for disease modelling and drug discovery,” *Nature Reviews Drug Discovery*, vol. 10, no. 12. pp. 915–929, Dec-2011.

[6] J. Sandoe and K. Eggan, “Opportunities and challenges of pluripotent stem cell neurodegenerative disease models,” *Nature Neuroscience*, vol. 16, no. 7. Nature Publishing Group, pp. 780–789, 2013.

[7] H. Geckil, F. Xu, X. Zhang, S. Moon, and U. Demirci, “Engineering hydrogels as extracellular matrix mimics,” *Nanomedicine*, vol. 5, no. 3. pp. 469–484, Apr-2010.

[8] A. B. Dababneh and I. T. Ozbolat, “Bioprinting Technology: A Current State-of-the-Art Review,” *J. Manuf. Sci. Eng. Trans. ASME*, vol. 136, no. 6, Dec. 2014.

[9] Y. Sasai, “Next-generation regenerative medicine: Organogenesis from stem cells in 3D culture,” *Cell Stem Cell*, vol. 12, no. 5. pp. 520–530, 02-May-2013.

[10] B. R. Dye *et al.*, “In vitro generation of human pluripotent stem cell derived lung organoids,” *Elife*, vol. 2015, no. 4, pp. 1–25, Mar. 2015.

[11] M. A. Lancaster and J. A. Knoblich, “Organogenesisin a dish: Modeling development and disease using organoid technologies,” *Science*, vol. 345, no. 6194. American Association for the Advancement of Science, 2014.

[12] B. Guillotin and F. Guillemot, “Cell patterning technologies for organotypic tissue fabrication,” *Trends in Biotechnology*, vol. 29, no. 4. pp. 183–190, Apr-2011.

[13] J. W. Nichol and A. Khademhosseini, “Modular tissue engineering: Engineering biological tissues from the bottom up,” *Soft Matter*, vol. 5, no. 7, pp. 1312–1319, 2009.

[14] C. Du, K. Narayanan, M. F. Leong, and A. C. A. Wan, “Induced pluripotent stem cell-derived hepatocytes and endothelial cells in multi-component hydrogel fibers for liver

tissue engineering," *Biomaterials*, vol. 35, no. 23, pp. 6006–6014, 2014.

[15] E. R. Shamir and A. J. Ewald, "Three-dimensional organotypic culture: Experimental models of mammalian biology and disease," *Nature Reviews Molecular Cell Biology*, vol. 15, no. 10. Nature Publishing Group, pp. 647–664, 01-Jan-2014.

[16] M. A. Lancaster *et al.*, "Cerebral organoids model human brain development and microcephaly," *Nature*, vol. 501, no. 7467, pp. 373–379, 2013.

[17] T. Takebe *et al.*, "Vascularized and functional human liver from an iPSC-derived organ bud transplant," *Nature*, vol. 499, no. 7459, pp. 481–484, 2013.

[18] M. Takasato *et al.*, "Directing human embryonic stem cell differentiation towards a renal lineage generates a self-organizing kidney," *Nat. Cell Biol.*, vol. 16, no. 1, pp. 118–126, Jan. 2014.

[19] Y. Xia *et al.*, "Directed Differentiation of Human Pluripotent Cells to Ureteric Bud Kidney Progenitor-Like Cells," *Nat. Cell Biol.*, vol. 15, no. 12, pp. 1507–1515, 2013.

[20] C. W. Chua *et al.*, "Single luminal epithelial progenitors can generate prostate organoids in culture," *Nat. Cell Biol.*, vol. 16, no. 10, pp. 951–961, Jan. 2014.

[21] M. Eiraku *et al.*, "Self-organizing optic-cup morphogenesis in three-dimensional culture," *Nature*, vol. 472, no. 7341, pp. 51–58, Apr. 2011.

[22] J. R. Spence *et al.*, "Directed differentiation of human pluripotent stem cells into intestinal tissue in vitro," *Nature*, vol. 470, no. 7332, pp. 105–110, Feb. 2011.

[23] M. A. Lancaster and J. A. Knoblich, "Generation of cerebral organoids from human pluripotent stem cells," *Nat. Protoc.*, vol. 9, no. 10, pp. 2329–2340, Oct. 2014.

[24] J. G. Camp *et al.*, "Human cerebral organoids recapitulate gene expression programs of fetal neocortex development," *Proc. Natl. Acad. Sci. U. S. A.*, vol. 112, no. 51, pp. 15672–15677, Dec. 2015.

[25] J. Jo *et al.*, "Midbrain-like Organoids from Human Pluripotent Stem Cells Contain Functional Dopaminergic and Neuromelanin-Producing Neurons," *Cell Stem Cell*, vol. 19, no. 2, pp. 248–257, Aug. 2016.

[26] M. A. Lancaster *et al.*, "Guided self-organization and cortical plate formation in human brain organoids," *Nat. Biotechnol.*, vol. 35, no. 7, pp. 659–666, Jul. 2017.

[27] Y. Sasai, "Cytosystems dynamics in self-organization of tissue architecture," *Nature*, vol. 493, no. 7432. pp. 318–326, 17-Jan-2013.

[28] S. Guven, P. Chen, F. Inci, S. Tasoglu, B. Erkmen, and U. Demirci, "Multiscale assembly for tissue engineering and regenerative medicine," *Trends in Biotechnology*, vol. 33, no. 5. Elsevier Ltd, pp. 269–279, 01-May-2015.

[29] X. Yin, B. E. Mead, H. Safaee, R. Langer, J. M. Karp, and O. Levy, "Engineering Stem Cell Organoids," *Cell Stem Cell*, vol. 18, no. 1. Cell Press, pp. 25–38, 07-Jan-2016.

[30] R. S. Ashton, A. J. Keung, J. Peltier, and D. V. Schaffer, “Progress and Prospects for Stem Cell Engineering,” *Annu. Rev. Chem. Biomol. Eng.*, vol. 2, no. 1, pp. 479–502, Jul. 2011.

[31] N. A. Peppas, P. Bures, W. Leobandung, and H. Ichikawa, “Hydrogels in pharmaceutical formulations,” *European Journal of Pharmaceutics and Biopharmaceutics*, vol. 50, no. 1. pp. 27–46, 03-Jul-2000.

[32] S. Van Vlierberghe, P. Dubruel, and E. Schacht, “Biopolymer-based hydrogels as scaffolds for tissue engineering applications: A review,” *Biomacromolecules*, vol. 12, no. 5. pp. 1387–1408, 09-May-2011.

[33] M. P. Lutolf and J. A. Hubbell, “Synthetic biomaterials as instructive extracellular microenvironments for morphogenesis in tissue engineering,” *Nature Biotechnology*, vol. 23, no. 1. pp. 47–55, 2005.

[34] C. S. Hughes, L. M. Postovit, and G. A. Lajoie, “Matrigel: a complex protein mixture required for optimal growth of cell culture.,” *Proteomics*, vol. 10, no. 9, pp. 1886–1890, 2010.

[35] B. A. Lindborg *et al.*, “Rapid Induction of Cerebral Organoids From Human Induced Pluripotent Stem Cells Using a Chemically Defined Hydrogel and Defined Cell Culture Medium,” *Stem Cells Transl. Med.*, vol. 5, no. 7, pp. 970–979, Jul. 2016.

[36] A. Meinhardt *et al.*, “3D reconstitution of the patterned neural tube from embryonic stem cells,” *Stem Cell Reports*, vol. 3, no. 6, pp. 987–999, Dec. 2014.

[37] S. F. Gilbert, “Developmental Biology - NCBI Bookshelf,” *Sinauer Associates, Inc. Sunderland*, 2000. [Online]. Available: https://www.ncbi.nlm.nih.gov/books/NBK9983/. [Accessed: 05-Nov-2019].

[38] E. Ruoslahti, “RGD AND OTHER RECOGNITION SEQUENCES FOR INTEGRINS,” *Annu. Rev. Cell Dev. Biol.*, vol. 12, no. 1, pp. 697–715, Nov. 1996.

[39] S. T. Wall, K. Saha, R. S. Ashton, K. R. Kam, D. V. Schaffer, and K. E. Healy, “Multivalency of sonic hedgehog conjugated to linear polymer chains modulates protein potency,” *Bioconjug. Chem.*, vol. 19, no. 4, pp. 806–812, Apr. 2008.

[40] T. Vazin *et al.*, “The effect of multivalent Sonic hedgehog on differentiation of human embryonic stem cells into dopaminergic and GABAergic neurons,” *Biomaterials*, vol. 35, no. 3, pp. 941–948, Jan. 2014.

[41] R. S. Ashton *et al.*, “Astrocytes regulate adult hippocampal neurogenesis through ephrin-B signaling,” *Nat. Neurosci.*, vol. 15, no. 10, pp. 1399–1406, Oct. 2012.

[42] A. Conway *et al.*, “Multivalent ligands control stem cell behaviour in vitro and in vivo,” *Nat. Nanotechnol.*, vol. 8, no. 11, pp. 831–838, 2013.

[43] A. J. Engler, S. Sen, H. L. Sweeney, and D. E. Discher, “Matrix Elasticity Directs Stem Cell Lineage Specification,” *Cell*, vol. 126, no. 4, pp. 677–689, Aug. 2006.

[44] A. Banerjee *et al.*, “The influence of hydrogel modulus on the proliferation and differentiation of encapsulated neural stem cells,” *Biomaterials*, vol. 30, no. 27, pp. 4695–4699, Sep. 2009.

[45] Y. Shao and J. Fu, “Integrated micro/nanoengineered functional biomaterials for cell mechanics and mechanobiology: A materials perspective,” *Advanced Materials*, vol. 26, no. 10. pp. 1494–1533, 12-Mar-2014.

[46] S. Khetan, M. Guvendiren, W. R. Legant, D. M. Cohen, C. S. Chen, and J. A. Burdick, “Degradation-mediated cellular traction directs stem cell fate in covalently crosslinked three-dimensional hydrogels,” *Nat. Mater.*, vol. 12, no. 5, pp. 458–465, 2013.

[47] S. Rammensee, M. S. Kang, K. Georgiou, S. Kumar, and D. V. Schaffer, “Dynamics of Mechanosensitive Neural Stem Cell Differentiation,” *Stem Cells*, vol. 35, no. 2, pp. 497–506, Feb. 2017.

[48] C. A. Deforest, B. D. Polizzotti, and K. S. Anseth, “Sequential click reactions for synthesizing and patterning three-dimensional cell microenvironments,” *Nat. Mater.*, vol. 8, no. 8, pp. 659–664, 2009.

[49] C. A. DeForest and K. S. Anseth, “Cytocompatible click-based hydrogels with dynamically tunable properties through orthogonal photoconjugation and photocleavage reactions,” *Nat. Chem.*, vol. 3, no. 12, pp. 925–931, Dec. 2011.

[50] C. M. Nelson and J. P. Gleghorn, “Sculpting Organs: Mechanical Regulation of Tissue Development,” *Annu. Rev. Biomed. Eng.*, vol. 14, no. 1, pp. 129–154, Aug. 2012.

[51] D. E. Discher, D. J. Mooney, and P. W. Zandstra, “Growth factors, matrices, and forces combine and control stem cells,” *Science*, vol. 324, no. 5935. pp. 1673–1677, 26-Jun-2009.

[52] T. D. Hansen *et al.*, “Biomaterial arrays with defined adhesion ligand densities and matrix stiffness identify distinct phenotypes for tumorigenic and non-tumorigenic human mesenchymal cell types,” *Biomater. Sci.*, vol. 2, no. 5, pp. 745–756, 2014.

[53] L. Jongpaiboonkit *et al.*, “An adaptable hydrogel array format for 3-dimensional cell culture and analysis,” *Biomaterials*, vol. 29, no. 23, pp. 3346–3356, Aug. 2008.

[54] P. Occhetta, R. Visone, and M. Rasponi, “High-throughput microfluidic platform for 3D cultures of mesenchymal stem cells,” in *Methods in Molecular Biology*, vol. 1612, Humana Press Inc., 2017, pp. 303–323.

[55] A. Ranga, S. Gobaa, Y. Okawa, K. Mosiewicz, A. Negro, and M. P. Lutolf, “3D niche microarrays for systems-level analyses of cell fate,” *Nat. Commun.*, vol. 5, Jul. 2014.

[56] B. D. Cosgrove, L. G. Griffith, and D. A. Lauffenburger, “Fusing Tissue Engineering and Systems Biology Toward Fulfilling Their Promise,” *Cell. Mol. Bioeng.*, vol. 1, no. 1, pp. 33–41, Mar. 2008.

[57] H. Qi *et al.*, “DNA-directed self-assembly of shape-controlled hydrogels,” *Nat. Commun.*,

vol. 4, Sep. 2013.

[58] M. D. Tang-Schomer *et al.*, “Bioengineered functional brain-like cortical tissue,” *Proc. Natl. Acad. Sci. U. S. A.*, vol. 111, no. 38, pp. 13811–13816, Sep. 2014.

[59] P. J. Su, Q. A. Tran, J. J. Fong, K. W. Eliceiri, B. M. Ogle, and P. J. Campagnola, “Mesenchymal stem cell interactions with 3D ECM modules fabricated via multiphoton excited photochemistry,” *Biomacromolecules*, vol. 13, no. 9, pp. 2917–2925, Sep. 2012.

[60] R. O. Hynes, “The extracellular matrix: Not just pretty fibrils,” *Science*, vol. 326, no. 5957. pp. 1216–1219, 27-Nov-2009.

[61] N. A. Sears, D. R. Seshadri, P. S. Dhavalikar, and E. Cosgriff-Hernandez, “A Review of Three-Dimensional Printing in Tissue Engineering,” *Tissue Engineering - Part B: Reviews*, vol. 22, no. 4. Mary Ann Liebert Inc., pp. 298–310, 01-Aug-2016.

[62] Y. Cao, J. P. Vacanti, K. T. Paige, J. Upton, and C. A. Vacanti, “Transplantation of chondrocytes utilizing a polymer-cell construct to produce tissue-engineered cartilage in the shape of a human ear,” *Plast. Reconstr. Surg.*, vol. 100, no. 2, pp. 297–304, Aug. 1997.

[63] H. W. Kang, S. J. Lee, I. K. Ko, C. Kengla, J. J. Yoo, and A. Atala, “A 3D bioprinting system to produce human-scale tissue constructs with structural integrity,” *Nat. Biotechnol.*, vol. 34, no. 3, pp. 312–319, Mar. 2016.

[64] A. Warmflash, B. Sorre, F. Etoc, E. D. Siggia, and A. H. Brivanlou, “A method to recapitulate early embryonic spatial patterning in human embryonic stem cells,” *Nat. Methods*, vol. 11, no. 8, pp. 847–854, 2014.

[65] G. T. Knight, J. Sha, and R. S. Ashton, “Micropatterned, clickable culture substrates enable in situ spatiotemporal control of human PSC-derived neural tissue morphology,” *Chem. Commun.*, vol. 51, no. 25, pp. 5238–5241, Mar. 2015.

[66] Z. Ma *et al.*, “Self-organizing human cardiac microchambers mediated by geometric confinement,” *Nat. Commun.*, vol. 6, Jul. 2015.

[67] K. Taniguchi *et al.*, “Lumen Formation Is an Intrinsic Property of Isolated Human Pluripotent Stem Cells,” *Stem Cell Reports*, vol. 5, no. 6, pp. 954–962, Dec. 2015.

[68] T. J. Hinton *et al.*, “Three-dimensional printing of complex biological structures by freeform reversible embedding of suspended hydrogels,” *Sci. Adv.*, vol. 1, no. 9, Oct. 2015.

[69] J. S. Miller *et al.*, “Rapid casting of patterned vascular networks for perfusable engineered three-dimensional tissues,” *Nat. Mater.*, vol. 11, no. 9, pp. 768–774, 2012.

[70] X. Y. Wang, Z. H. Jin, B. W. Gan, S. W. Lv, M. Xie, and W. H. Huang, “Engineering interconnected 3D vascular networks in hydrogels using molded sodium alginate lattice as the sacrificial template,” *Lab Chip*, vol. 14, no. 15, pp. 2709–2716, Aug. 2014.

[71] A. Tocchio *et al.*, “Versatile fabrication of vascularizable scaffolds for large tissue engineering in bioreactor,” *Biomaterials*, vol. 45, pp. 124–131, Mar. 2015.

[72] H. Van De Velde, G. Cauffman, H. Tournaye, P. Devroey, and I. Liebaers, “The four blastomeres of a 4-cell stage human embryo are able to develop individually into blastocysts with inner cell mass and trophectoderm,” *Hum. Reprod.*, vol. 23, no. 8, pp. 1742–1747, 2008.

[73] G. Guo *et al.*, “Resolution of Cell Fate Decisions Revealed by Single-Cell Gene Expression Analysis from Zygote to Blastocyst,” *Dev. Cell*, vol. 18, no. 4, pp. 675–685, Apr. 2010.

[74] M. J. Workman *et al.*, “Engineered human pluripotent-stem-cell-derived intestinal tissues with a functional enteric nervous system,” *Nat. Med.*, vol. 23, no. 1, pp. 49–59, Jan. 2017.

[75] M. E. Todhunter *et al.*, “Programmed synthesis of three-dimensional tissues,” *Nat. Methods*, vol. 12, no. 10, pp. 975–981, Sep. 2015.

[76] T. M. Patz *et al.*, “Three-dimensional direct writing of B35 neuronal cells,” *J. Biomed. Mater. Res. - Part B Appl. Biomater.*, vol. 78, no. 1, pp. 124–130, Jul. 2006.

[77] J. A. Barron, B. J. Spargo, and B. R. Ringeisen, “Biological laser printing of three dimensional cellular structures,” in *Applied Physics A: Materials Science and Processing*, 2004, vol. 79, no. 4–6, pp. 1027–1030.

[78] N. R. Schiele, D. T. Corr, Y. Huang, N. A. Raof, Y. Xie, and D. B. Chrisey, “Laser-based direct-write techniques for cell printing,” *Biofabrication*, vol. 2, no. 3. Sep-2010.

[79] N. R. Schiele *et al.*, “Laser direct writing of combinatorial libraries of idealized cellular constructs: Biomedical applications,” *Appl. Surf. Sci.*, vol. 255, no. 10, pp. 5444–5447, Mar. 2009.

[80] J. A. Barron, D. B. Krizman, and B. R. Ringeisen, “Laser printing of single cells: Statistical analysis, cell viability, and stress,” *Ann. Biomed. Eng.*, vol. 33, no. 2, pp. 121–130, Feb. 2005.

[81] A. Schepers, C. Li, A. Chhabra, B. T. Seney, and S. Bhatia, “Engineering a perfusable 3D human liver platform from iPS cells,” *Lab Chip*, vol. 16, no. 14, pp. 2644–2653, 2016.

[82] A. Odawara, M. Gotoh, and I. Suzuki, “A three-dimensional neuronal culture technique that controls the direction of neurite elongation and the position of soma to mimic the layered structure of the brain,” *RSC Adv.*, vol. 3, no. 45, pp. 23620–23630, Dec. 2013.

[83] J. Sha, E. S. Lippmann, J. McNulty, Y. Ma, and R. S. Ashton, “Sequential nucleophilic substitutions permit orthogonal click functionalization of multicomponent PEG brushes,” *Biomacromolecules*, vol. 14, no. 9, pp. 3294–3303, Sep. 2013.

[84] H. Onoe *et al.*, “Metre-long cell-laden microfibres exhibit tissue morphologies and functions,” *Nat. Mater.*, vol. 12, no. 6, pp. 584–590, Jun. 2013.

[85] K. G. Storey, J. M. Crossley, E. M. De Robertis, W. E. Norris, and C. D. Stern, “Neural

induction and regionalisation in the chick embryo," *Development*, vol. 114, no. 3, 1992.

[86] R. D. Del Corral and K. G. Storey, "Opposing FGF and retinoid pathways: A signalling switch that controls differentiation and patterning onset in the extending vertebrate body axis," *BioEssays*, vol. 26, no. 8. pp. 857–869, Aug-2004.

[87] H. F. Farin *et al.*, "Visualization of a short-range Wnt gradient in the intestinal stem-cell niche," *Nature*, vol. 530, no. 7590, pp. 340–343, Feb. 2016.

[88] E. K. Sackmann, A. L. Fulton, and D. J. Beebe, "The present and future role of microfluidics in biomedical research," *Nature*, vol. 507, no. 7491. Nature Publishing Group, pp. 181–189, 2014.

[89] K. Lee, E. A. Silva, and D. J. Mooney, "Growth factor delivery-based tissue engineering: General approaches and a review of recent developments," *Journal of the Royal Society Interface*, vol. 8, no. 55. Royal Society, pp. 153–170, 06-Feb-2011.

[90] S. G. M. Uzel, O. C. Amadi, T. M. Pearl, R. T. Lee, P. T. C. So, and R. D. Kamm, "Simultaneous or Sequential Orthogonal Gradient Formation in a 3D Cell Culture Microfluidic Platform," *Small*, vol. 12, no. 5, pp. 612–622, Feb. 2016.

[91] J. Briscoe and J. Ericson, "The specification of neuronal identity by graded sonic hedgehog signalling," *Semin. Cell Dev. Biol.*, vol. 10, no. 3, pp. 353–362, Jun. 1999.

[92] C. J. Demers *et al.*, "Development-on-chip: In vitro neural tube patterning with a microfluidic device," *Dev.*, vol. 143, no. 11, pp. 1884–1892, Jun. 2016.

[93] M. J. Mahoney and W. M. Saltzman, "Transplantation of brain cells assembled around a programmable synthetic microenvironment," *Nat. Biotechnol.*, vol. 19, no. 10, pp. 934–939, 2001.

[94] R. L. Carpenedo *et al.*, "Homogeneous and organized differentiation within embryoid bodies induced by microsphere-mediated delivery of small molecules," *Biomaterials*, vol. 30, no. 13, pp. 2507–2515, May 2009.

[95] P. N. Dang *et al.*, "Controlled Dual Growth Factor Delivery From Microparticles Incorporated Within Human Bone Marrow-Derived Mesenchymal Stem Cell Aggregates for Enhanced Bone Tissue Engineering via Endochondral Ossification," *Stem Cells Transl. Med.*, vol. 5, no. 2, pp. 206–217, Feb. 2016.

[96] N. A. Impellitteri, M. W. Toepke, S. K. Lan Levengood, and W. L. Murphy, "Specific VEGF sequestering and release using peptide-functionalized hydrogel microspheres," *Biomaterials*, vol. 33, no. 12, pp. 3475–3484, Apr. 2012.

[97] C. L. Watson *et al.*, "An in vivo model of human small intestine using pluripotent stem cells," *Nat. Med.*, vol. 20, no. 11, pp. 1310–1314, Nov. 2014.

[98] G. La Manno *et al.*, "Molecular Diversity of Midbrain Development in Mouse, Human, and Stem Cells," *Cell*, vol. 167, no. 2, pp. 566-580.e19, Oct. 2016.

[99] M. B. Johnson and C. A. Walsh, “Cerebral cortical neuron diversity and development at single-cell resolution,” *Current Opinion in Neurobiology*, vol. 42. Elsevier Ltd, pp. 9–16, 01-Feb-2017.

[100] W. A. Alaynick, T. M. Jessell, and S. L. Pfaff, “SnapShot: Spinal cord development,” *Cell*, vol. 146, no. 1. Cell Press, pp. 178.e1-178.e1, 08-Jul-2011.

[101] D. M. DeLaughter *et al.*, “Single-Cell Resolution of Temporal Gene Expression during Heart Development,” *Dev. Cell*, vol. 39, no. 4, pp. 480–490, Nov. 2016.

[102] D. Grün *et al.*, “Single-cell messenger RNA sequencing reveals rare intestinal cell types,” *Nature*, vol. 525, no. 7568, pp. 251–255, Sep. 2015.

[103] B. Treutlein *et al.*, “Reconstructing lineage hierarchies of the distal lung epithelium using single-cell RNA-seq,” *Nature*, vol. 509, no. 7500, pp. 371–375, 2014.

[104] M. J. Muraro *et al.*, “A Single-Cell Transcriptome Atlas of the Human Pancreas,” *Cell Syst.*, vol. 3, no. 4, pp. 385-394.e3, Oct. 2016.

[105] P. Kerscher *et al.*, “Direct hydrogel encapsulation of pluripotent stem cells enables ontomimetic differentiation and growth of engineered human heart tissues,” *Biomaterials*, vol. 83, pp. 383–395, Mar. 2016.

[106] J. P. Vacanti and R. Langer, “Tissue engineering: The design and fabrication of living replacement devices for surgical reconstruction and transplantation,” *Lancet*, vol. 354, no. SUPPL.1, pp. 32–34, 1999.

[107] R. S. Ashton, A. Banerjee, S. Punyani, D. V. Schaffer, and R. S. Kane, “Scaffolds based on degradable alginate hydrogels and poly(lactide-co-glycolide) microspheres for stem cell culture,” *Biomaterials*, vol. 28, no. 36, pp. 5518–5525, Dec. 2007.

[108] J. G. Fernandez and A. Khademhosseini, “Micro-masonry: Construction of 3D structures by microscale self-assembly,” *Adv. Mater.*, vol. 22, no. 23, pp. 2538–2541, Jun. 2010.

[109] T. S. Karande, J. L. Ong, and C. M. Agrawal, “Diffusion in musculoskeletal tissue engineering scaffolds: Design issues related to porosity, permeability, architecture, and nutrient mixing,” *Ann. Biomed. Eng.*, vol. 32, no. 12, pp. 1728–1743, 2004.

[110] D. B. Kolesky, R. L. Truby, A. S. Gladman, T. A. Busbee, K. A. Homan, and J. A. Lewis, “3D bioprinting of vascularized, heterogeneous cell-laden tissue constructs,” *Adv. Mater.*, vol. 26, no. 19, pp. 3124–3130, May 2014.

[111] L. M. Bellan, S. P. Singh, P. W. Henderson, T. J. Porri, H. G. Craighead, and J. A. Spector, “Fabrication of an artificial 3-dimensional vascular network using sacrificial sugar structures,” *Soft Matter*, vol. 5, no. 7, pp. 1354–1357, 2009.

[112] W. Wu, C. J. Hansen, A. M. Aragón, P. H. Geubelle, S. R. White, and J. A. Lewis, “Direct-write assembly of biomimetic microvascular networks for efficient fluid transport,” *Soft Matter*, vol. 6, no. 4, pp. 739–742, 2010.

[113] A. P. Golden and J. Tien, “Fabrication of microfluidic hydrogels using molded gelatin as a sacrificial element,” *Lab Chip*, vol. 7, no. 6, pp. 720–725, 2007.

[114] M. P. Cuchiara, A. C. B. Allen, T. M. Chen, J. S. Miller, and J. L. West, “Multilayer microfluidic PEGDA hydrogels,” *Biomaterials*, vol. 31, no. 21, pp. 5491–5497, Jul. 2010.

[115] J. A. Rowley, G. Madlambayan, and D. J. Mooney, “Alginate hydrogels as synthetic extracellular matrix materials,” *Biomaterials*, vol. 20, no. 1, pp. 45–53, Jan. 1999.

[116] Z. Chen and L. S. Turng, “A review of current developments in process and quality control for injection molding,” *Advances in Polymer Technology*, vol. 24, no. 3. pp. 165–182, Sep-2005.

[117] S. Liu and Y. Chen, “Water-assisted injection molding of thermoplastic materials: Effects of processing parameters,” *Polym. Eng. Sci.*, vol. 43, no. 11, pp. 1806–1817, Nov. 2003.

[118] T. A. Osswald, L.-S. Turng, and P. J. Gramann, *Injection molding handbook*. Hanser Publishers, 2002.

[119] Astm, “ASTM D638: Standard Test Method for Tensile Properties of Plastics,” 2004.

[120] M. W. Toepke, N. A. Impellitteri, J. M. Theisen, and W. L. Murphy, “Characterization of Thiol-Ene Crosslinked PEG Hydrogels,” *Macromol. Mater. Eng.*, vol. 298, no. 6, pp. 699–703, Jun. 2013.

[121] S. R. Peyton, C. B. Raub, V. P. Keschrumrus, and A. J. Putnam, “The use of poly(ethylene glycol) hydrogels to investigate the impact of ECM chemistry and mechanics on smooth muscle cells,” *Biomaterials*, vol. 27, no. 28, pp. 4881–4893, Oct. 2006.

[122] A. A. Bonapasta, F. Buda, P. Colombet, and G. Guerrini, “Cross-Linking of Poly(Vinyl Alcohol) Chains by Ca Ions in Macro-Defect-Free Cements,” *Chem. Mater.*, vol. 14, no. 3, pp. 1016–1022, Mar. 2002.

[123] E. S. Lippmann, M. C. Estevez-Silva, and R. S. Ashton, “Defined human pluripotent stem cell culture enables highly efficient neuroepithelium derivation without small molecule inhibitors,” *Stem Cells*, vol. 32, no. 4, pp. 1032–1042, 2014.

[124] S. A. Bayer and J. Altman, “Atlas of Human Central Nervous System Development,” *CRC Press Online*, 2002. [Online]. Available: https://www.crcpress.com/Atlas-of-Human-Central-Nervous-System-Development/book-series/CRCAHCNSD. [Accessed: 13-Nov-2019].

[125] M. Huch, J. A. Knoblich, M. P. Lutolf, and A. Martinez-Arias, “The hope and the hype of organoid research,” 2017.

[126] G. T. Knight *et al.*, “Engineering induction of singular neural rosette emergence within hPSC-derived tissues,” *Elife*, vol. 7, Oct. 2018.

[127] M. C. Estevez-Silva, A. Sreeram, S. Cuskey, N. Fedorchak, N. Iyer, and R. S. Ashton, “Single-injection ex ovo transplantation method for broad spinal cord engraftment of

human pluripotent stem cell-derived motor neurons," *J. Neurosci. Methods*, vol. 298, pp. 16–23, Mar. 2018.

[128] S. Vega-Alvarez, A. Herrera, C. Rinaldi, and F. A. Carrero-Martínez, "Tissue-specific direct microtransfer of nanomaterials into Drosophila embryos as a versatile in vivo test bed for nanomaterial toxicity assessment," *Int. J. Nanomedicine*, vol. 9, no. 1, pp. 2031–2041, Apr. 2014.

[129] "ASTM D638 - Instron." [Online]. Available: https://www.instron.us/testing-solutions/by-standard/astm/multiple-testing-solutions/astm-d638. [Accessed: 02-Jan-2020].

[130] K. Y. Kwan, N. Šestan, and E. S. Anton, "Transcriptional co-regulation of neuronal migration and laminar identity in the neocortex," *Development*, vol. 139, no. 9. Oxford University Press for The Company of Biologists Limited, pp. 1535–1546, 01-May-2012.

[131] Z. Molnár *et al.*, "New insights into the development of the human cerebral cortex," *J. Anat.*, vol. 235, no. 3, pp. 432–451, Sep. 2019.

[132] A. A. Sivitilli *et al.*, "Robust production of uniform human cerebral organoids from pluripotent stem cells," *Life Sci. alliance*, vol. 3, no. 5, May 2020.

[133] L. Broutier *et al.*, "Culture and establishment of self-renewing human and mouse adult liver and pancreas 3D organoids and their genetic manipulation," *Nat. Protoc.*, vol. 11, no. 9, pp. 1724–1743, Sep. 2016.

[134] M. A. Lancaster and J. A. Knoblich, "Generation of cerebral organoids from human pluripotent stem cells," *Nat. Protoc.*, vol. 9, no. 10, pp. 2329–2340, Jan. 2014.

[135] C. R. Marti-Figueroa and R. S. Ashton, "The case for applying tissue engineering methodologies to instruct human organoid morphogenesis," *Acta Biomaterialia*, vol. 54. Elsevier Ltd, pp. 35–44, 01-May-2017.

[136] H. Hříbková, M. Grabiec, D. Klemová, I. Slaninová, and Y. M. Sun, "Calcium signaling mediates five types of cell morphological changes to form neural rosettes," *J. Cell Sci.*, vol. 131, no. 3, Feb. 2018.

[137] E. H. Nguyen *et al.*, "Versatile synthetic alternatives to Matrigel for vascular toxicity screening and stem cell expansion," *Nat. Biomed. Eng.*, vol. 1, no. 7, Jun. 2017.

[138] C. Barry *et al.*, "Uniform neural tissue models produced on synthetic hydrogels using standard culture techniques," *Exp. Biol. Med.*, vol. 242, no. 17, pp. 1679–1689, Nov. 2017.

[139] R. Cruz-Acuña *et al.*, "Synthetic hydrogels for human intestinal organoid generation and colonic wound repair," *Nat. Cell Biol.*, vol. 19, no. 11, pp. 1326–1335, Nov. 2017.

[140] B. Artegiani *et al.*, "Fast and efficient generation of knock-in human organoids using homology-independent CRISPR–Cas9 precision genome editing," *Nat. Cell Biol.*, vol. 22, no. 3, pp. 321–331, Mar. 2020.

[141] B. Koo, B. Choi, H. Park, and K. J. Yoon, “Past, Present, and Future of Brain Organoid Technology,” *Molecules and cells*, vol. 42, no. 9. NLM (Medline), pp. 617–627, 30-Sep-2019.

[142] J. Fischer, M. Heide, and W. B. Huttner, “Genetic Modification of Brain Organoids,” *Frontiers in Cellular Neuroscience*, vol. 13. Frontiers Media S.A., p. 558, 17-Dec-2019.

[143] S. Bian *et al.*, “Genetically engineered cerebral organoids model brain tumor formation,” *Nat. Methods*, vol. 15, no. 8, pp. 631–639, Aug. 2018.